COPY

(4)

AD-A202 237

TURBULENCE STRUCTURE AND MASS TRANSPORT IN A CHANNEL FLOW WITH POLYMER INJECTION

David T. Walker and William G. Tiederman
School of Mechanical Engineering
Purdue University
West Lafayette, Indiana 47907

December, 1988

Technical Report for Period 01 December 1987 - 30 November 1988

Approved for public release; distribution unlimited

DTIC ELECTE DEC 2 9 1988 S D E

Prepared for

OFFICE OF NAVAL RESEARCH
800 North Quincy Street
Arlington, VA 22217-5000

88 12 29 040

SECURITY CLASSIFICATION OF THIS PAGE (When Data Entered)

AD-A202237

REPORT DOCUMENTATION PAGE

READ INSTRUCTIONS BEFORE COMPLETING FORM

1. REPORT NUMBER: PME-FM-88-2	2. GOVT ACCESSION NO.
3. RECIPIENT'S CATALOG NUMBER	
4. TITLE (and Subtitle): Turbulent Structure and Mass Transport in a Channel Flow with Polymer Injection	5. TYPE OF REPORT & PERIOD COVERED: Technical Report for Dec. 1, 1987 through Nov. 30, 1988
6. PERFORMING ORG. REPORT NUMBER	
7. AUTHOR(s): David T. Walker, William G. Tiederman	8. CONTRACT OR GRANT NUMBER(s): N00014-83K-0183
9. PERFORMING ORGANIZATION NAME AND ADDRESS: School of Mechanical Engineering, Purdue University, West Lafayette, Indiana 47907	10. PROGRAM ELEMENT, PROJECT, TASK AREA & WORK UNIT NUMBERS: 4322-754
11. CONTROLLING OFFICE NAME AND ADDRESS: Office of Naval Research, 800 North Quincy Street, Arlington, VA 22217-5000	12. REPORT DATE: December, 1988
	13. NUMBER OF PAGES: 142
14. MONITORING AGENCY NAME & ADDRESS (if different from Controlling Office)	15. SECURITY CLASS. (of this report)
	15a. DECLASSIFICATION/DOWNGRADING SCHEDULE

16. DISTRIBUTION STATEMENT (of this Report)

APPROVED FOR PUBLIC RELEASE: DISTRIBUTION UNLIMITED

17. DISTRIBUTION STATEMENT (of the abstract entered in Block 20, if different from Report)

18. SUPPLEMENTARY NOTES

19. KEY WORDS (Continue on reverse side if necessary and identify by block number)

Drag reduction; turbulent wall flows; concentration measurements

20. ABSTRACT (Continue on reverse side if necessary and identify by block number)

This study which examined a fully developed turbulent channel flow with polymer injection at the wall had two complimentary objectives. The first objective was to gain more understanding of the way in which long-chain, high-molecular-weight, water soluble polymers effect viscous drag reduction in turbulent wall flows. The second was to acquire information useful in the modeling of the transport processes in flows with polymer injection at the wall, particularly the high Schmidt number mixing process. A

DD FORM 1 JAN 73 1473 EDITION OF 1 NOV 65 IS OBSOLETE
S/N 0102-014-6601

SECURITY CLASSIFICATION OF THIS PAGE (When Data Entered)

fluorescence technique was developed for time-resolved measurements of species concentration profiles. This technique was combined with laser velocimetry to obtain measurements of turbulent mass transport in a flow with polymer injection and, for comparison purposes, a flow with water injection. Two-component laser velocimeter measurements were made in both flows to examine the effect of both the injection process and the evolving polymer concentration field on the structure of turbulence.

In the flows with injection, the major transport mechanism was identified as long (in the streamwise direction) filaments of high concentration fluid periodically lifting away from the near-wall region. When polymer was injected, mixing of the injected fluid with the outer flow required longer streamwise distance than for water injection. The high extensional viscosity of the polymer solution resulted in a strong correlation between large instantaneous polymer concentrations and small wall-normal velocity fluctuations causing lower levels of turbulent mass transport. After the polymer solution began to mix with the flow, the turbulent mass transport was smaller than in the flow with water injection but the degree of correlation between velocity and concentration fluctuations was comparable. This indicates that the mass transport processes were similar for these two cases. In both cases, the high Schmidt number resulted in high concentration fluid mixing from the near-wall region to the outer flow and then back near the wall yielding low levels of net turbulent mass transport.

Measurements of turbulence structure show that while the root-mean-square (RMS) fluctuation level of the streamwise velocity was increased by the presence of the polymer solution, the RMS of the wall-normal velocity and the Reynolds shear stress were reduced as the polymer solution mixed with the flow. Production of the streamwise Reynolds normal stress was decreased but the production of the Reynolds shear stress was unchanged. This shows that the pressure-strain correlation terms in the Reynolds stress transport equations may be directly affected by the polymers.

TABLE OF CONTENTS

	Page
LIST OF TABLES	iii
LIST OF FIGURES	iv
LIST OF SYMBOLS	ix
CHAPTER 1 - INTRODUCTION	1
1.1 Objectives	2
1.2 Drag-reducing polymer solutions	3
1.3 Turbulence structure and drag reduction	4
1.4 Scalar transport and the dispersion of injected polymer solutions	7
1.5 Closure	10
CHAPTER 2 - APPARATUS AND PROCEDURES	12
2.1 Experimental facilities	12
2.2 Polymer solution preparation	14
2.3 Velocity measurements	16
2.4 Concentration measurements	23
2.5 Simultaneous velocity and concentration measurements	33
2.6 Data analysis	37
CHAPTER 3 - WATER FLOW RESULTS	43
3.1 Experimental conditions	43
3.2 Mean velocities	46
3.3 Second moments	46
3.4 Reynolds stress production	57
CHAPTER 4 - THE CONCENTRATION FIELD IN INJECTED FLOWS	63
4.1 Time-resolved concentration profiles	64
4.2 Probability density functions for concentration	67
4.3 Time-averaged statistics	76
CHAPTER 5 - THE STRUCTURE OF TURBULENCE IN INJECTED FLOWS	85
5.1 Mean velocities	85
5.2 Second moments	88

Page

5.3 Reynolds stress production 96

CHAPTER 6 - TURBULENT MASS TRANSPORT 100
6.1 Time-averaged turbulent mass transport 100
6.2 The detailed structure of turbulent mass transport 106
6.3 Implications for modeling 117

CHAPTER 7 - SUMMARY AND CONCLUSIONS 123

REFERENCES 128

APPENDICES
Appendix A: Calculation of Rotated Statistics 132
Appendix B: Uncertainty Analysis 135

VITA 143

LIST OF TABLES

Table		Page
2.1	Estimated error in wall-normal root-mean-square velocities from results of Kim et al. (1987).	18
3.1	Experimental conditions for water flow with no injection.	44

Accession For
NTIS GRA&I
DTIC TAB
Unannounced
Justification
By
Distribution/
Availability Codes
Dist | Avail and/or Special
A-1

QUALITY INSPECTED 2

LIST OF FIGURES

Figure		Page
2.1	Schematic of flow loop.	13
2.2	Injection slot and optical arrangement.	15
2.3	Space-averaged dye concentration determined by: ———— , attenuation; – – – – , integration of measured dye concentration profile.	32
2.4	Schematic of optics for simultaneous velocity and concentration measurement.	34
2.5	Block diagram of electronics for simultaneous velocity and concentration measurement.	38
3.1	Estimated shear velocity for water flow with no injection: * , u_τ; + , viscous contribution; O , turbulent contribution; ═══ , 95% confidence interval.	45
3.2	Mean velocity profile for water flow with no injection.	47
3.3	Root-mean-square velocity fluctuation profiles for water flow with no injection: * , u'/u_τ; + , v'/u_τ.	48
3.4	Near-wall behavior of root-mean-square velocity fluctuations: * , u'/u_τ; + , v'/u_τ; – – – – , $v'/u_\tau = 0.005y^{+2}$ (Finnicum and Hanratty, 1985); ———— , $v'/u_\tau = 0.009y^{+2}$ (Kim et al.,1987).	50
3.5	Turbulence intensity profiles for water flow with no injection: * , $u'/\overline{U}$; + , $v'/\overline{U}$.	51
3.6	Near-wall behavior of turbulence intensity: * , $u'/\overline{U}$; + , $v'/\overline{U}$.	52
3.7	Turbulent shear stress for water flow with no injection; ———— , total shear stress for fully developed flow (Equation 3.3).	54
3.8	Turbulent shear stress for water flow with no injection; ———— , Equation 3.4; I , 95 % confidence interval.	55
3.9	Correlation coefficient for water flow with no injection.	56

Figure		Page
3.10	Reynolds stress production ($\overline{u^2}$ component) for water flow with no injection; ———— , production calculated using $\overline{uv}$ from Equation 3.4.	61
3.11	Reynolds stress production ($\overline{uv}$ component) for water flow with no injection.	62
4.1	Time-resolved concentration profiles at x = 25 mm for water injection.	65
4.2	Time-resolved concentration profiles at x = 10 mm for polymer injection.	66
4.3	Time-resolved concentration profiles at x = 25 mm for polymer injection.	68
4.4	Time-resolved concentration profiles at x = 50 mm for polymer injection.	69
4.5	Time-resolved concentration profiles at x = 100 mm for polymer injection.	70
4.6	Time-resolved concentration profiles at x = 200 mm for polymer injection.	71
4.7	Probability density function for polymer concentration versus distance from the wall and concentration for x = 10 mm.	73
4.8	Probability density function for polymer concentration versus distance from the wall and concentration for x = 25 mm.	74
4.9	Probability density function for polymer concentration versus distance from the wall and concentration for x = 50 mm.	75
4.10	Probability density function for polymer concentration versus distance from the wall and concentration for x = 100 mm.	77
4.11	Probability density function for polymer concentration versus distance from the wall and concentration for x = 200 mm.	78
4.12	Mean concentration profiles for water injection: a) x = 10 mm, b) x = 25 mm, c) x = 50 mm, d) x = 100 mm.	79
4.13	Mean concentration profiles for polymer injection: a) x = 10 mm, b) x = 25 mm, c) x = 50 mm, d) x = 100 mm, e) x = 200 mm; ———— , water injection results.	80

Figure		Page
4.14	Root-mean-square concentration profiles for water injection: a) x = 10 mm, b) x = 25 mm, c) x = 50 mm, d) x = 100 mm.	82
4.15	Root-mean-square concentration profiles for polymer injection: a) x = 10 mm, b) x = 25 mm, c) x = 50 mm, d) x = 100 mm, e) x = 200 mm; ———— , water injection results.	83
5.1	Mean velocity profile for flow with water injection; ———— , no-injection results.	86
5.2	Mean velocity profiles for flow with polymer injection: a) x = 25 mm, b) x = 50 mm, c) x = 100 mm, d) x = 200 mm; ———— , no-injection results.	87
5.3	Root-mean-square velocity fluctuation profiles for flow with water injection: * , u'/u_τ; + , v'/u_τ; ———— , no-injection results.	89
5.4	Turbulent shear stress profile for flow with water injection; ————, no-injection results; I , 95 % confidence interval.	90
5.5	Root-mean-square velocity fluctuation (u'/u_τ) profiles for flow with polymer injection: a) x = 25 mm, b) x = 50 mm, c) x = 100 mm, d) x = 200 mm; ————, no-injection results.	91
5.6	Root-mean-square velocity fluctuation (v'/u_τ) profiles for flow with polymer injection: a) x = 25 mm, b) x = 50 mm, c) x = 100 mm, d) x = 200 mm; ————, no-injection results.	93
5.7	Turbulent shear stress profiles for flow with polymer injection: a) x = 25 mm, b) x = 50 mm, c) x = 100 mm, d) x = 200 mm; ———— , no-injection results; I , 95 % confidence interval.	94
5.8	Correlation coefficient for flow with polymer injection: a) x = 25 mm, b) x = 50 mm, c) x = 100 mm, d) x = 200 mm; ———— , no-injection results.	95
5.9	Reynolds stress production ($\overline{u^2}$ component) for flow with polymer injection: a) x = 25 mm, b) x = 50 mm, c) x = 100 mm, d) x = 200 mm; ———— , no-injection results.	97
5.10	Reynolds stress production ($\overline{uv}$ component) for flow with polymer injection: a) x = 25 mm, b) x = 50 mm, c) x = 100 mm, d) x = 200 mm; ———— , no-injection results.	98
6.1	Turbulent mass transport profile at x = 25 mm for water injection; I , 95 % confidence interval.	101

Figure Page

6.2 Turbulent mass transport profiles for polymer injection: a) x = 25 mm, b) x = 50 mm, c) x = 100 mm, d) x = 200 mm; ———— , x = 25 mm for water injection; I , 95 % confidence interval. 103

6.3 Mass-transport correlation coefficient profile at x = 25 mm for water injection. 104

6.4 Mass-transport correlation coefficient profiles for polymer injection: a) x = 25 mm, b) x = 50 mm, c) x = 100 mm, d) x = 200 mm; ———— , x = 25 mm for water injection. 105

6.5 Velocity and concentration scatter diagrams for flow with water injection: x = 25 mm, a) y^+ = 88.3, b) y^+ = 32.4, c) y^+ = 18.4. 107

6.6 F(v) for flow with water injection: x = 25 mm, a) y^+ = 88.3, b) y^+ = 32.4, c) y^+ = 18.4. 110

6.7 Velocity and concentration scatter diagrams for flow with polymer injection: x = 200 mm, a) y^+ = 109.2, b) y^+ = 27.1, c) y^+ = 13.1. 111

6.8 F(v) for flow with polymer injection: x = 200 mm, a) y^+ = 109.2, b) y^+ = 27.1, c) y^+ = 13.1. 113

6.9 Velocity and concentration scatter diagrams for flow with polymer injection: x = 25 mm, a) y^+ = 70.8, b) y^+ = 32.4, c) y^+ = 27.2. 114

6.10 F(v) for flow with polymer injection: x = 25 mm, a) y^+ = 70.8, b) y^+ = 32.4, c) y^+ = 27.2. 115

6.11 Ratio of turbulent mass transport to momentum transport: + , x = 25 mm with water injection; * , x = 200 mm with polymer injection. 118

6.12 Turbulent diffusivities for a) mass transport, b) momentum transport: + , x = 25 mm with water injection; * , x = 200 mm with polymer injection. 120

6.13 Turbulent Schmidt number profiles: + , x = 25 mm with water injection; * , x = 200 mm with polymer injection. 121

Appendix Figure | Page

A.1 Coordinate system for rotation of velocity statistics. 133

B.1 Uncertainty in estimated statistics due to finite ensemble size.
——— : $\overline{U}$, $\overline{V}$, $\overline{C}$; – – – – : u', v', c'; - - - - - : $\overline{uv}$, $\overline{vc}$. 140

LIST OF SYMBOLS

Symbol	Description
A_n	calibration constant for photodiode array element n
B	additive constant in the law of the wall
C	instantaneous concentration
C_i	injected concentration
D_{ab}	molecular mass diffusivity
F(v)	relative contribution of normal velocity fluctuations to mass transport, $F(v) = \frac{1}{\overline{vc}} \int_{-\infty}^{\infty} vc\, f(v,c)\, dc$
I	intensity of fluorescent emission
I_e	intensity of excitation laser beam
I_o	initial intensity of excitation laser beam
M	molar concentration, moles per liter
N	ensemble size
R	correlation coefficient
R_{uv}	correlation coefficient for momentum transport, $R_{uv} = \overline{uv}/u'v'$
R_{vc}	correlation coefficient for mass transport, $R_{vc} = \overline{vc}/v'c'$
RMS	root mean square
Sc	molecular Schmidt number, $Sc = \nu/D_{ab}$
Sc_t	turbulent Schmidt number, the ratio of the turbulent momentum diffusivity to the turbulent mass diffusivity
U, V, W	instantaneous velocities in the x, y and z directions respectively
U_m	mass-averaged velocity
U_o	center-line velocity
U_1, U_2	measured velocity components

Symbol	Description
V_{dn}	dark-level voltage from photodiode array element n
V_n	output voltage from photodiode array element n
a	channel half-height
a_n	fraction of the fluorescent emission from a point in the field of view which is incident on photodiode array element n
b_n	sensitivity of photodiode array element n
c	instantaneous concentration fluctuation, $c = C - \overline{C}$
d	y-direction length of concentration measurement volume
f(v,c)	joint probabiltiy density function for normal-velocity and concentration fluctuations
h	channel height
k	extinction coefficient for dye
l_x, l_y, l_z	dimensions of the laser velocimeter measurement volume in the x, y and z directions respectively
s	spacing of concentration measurement volumes
t	time
u,v,w	instantaneous velocity fluctuations in the x, y and z directions respectively: $u=U-\overline{U}$, $v=V-\overline{V}$, $w=W-\overline{W}$
u_1, u_2	instantaneous fluctuations in the measured velocity components: $u_1=U_1-\overline{U}_1$, $u_2=U_2-\overline{U}_2$
u_τ	shear velocity, $u_\tau = \sqrt{\tau_w/\rho}$
x,y,z	respectively, the streamwise, wall-normal and transverse directions
x_1, x_2	coordinate system for measured velocity components
ℓ	liters
α	proportionality constant relating the fluorescent emission of the dye to the amount of light absorbed
β	proportionality constant relating the dye extinction coefficient to the dye concentration
δ	uncertainty in an estimated statistic due to the finite ensemble size
δ^*	displacement thickness

Symbol	Description
ε	experimental uncertainty
κ	von Karman constant in the law of the wall
μ	dynamic viscosity
ν	kinematic viscosity
ρ	density
$\rho(c,y)$	probability density for concentration
σ	standard deviation
τ	shear stress
τ_w, τ_{wall}	wall shear stress
υ	total uncertainty, $\upsilon = \sqrt{\delta^2 + \varepsilon^2}$

Superscripts

$^+$	normalized with inner variables u_τ and ν
$\bar{}$	time average
$'$	root mean square (RMS)

This page intentionally left blank.

CHAPTER 1 - INTRODUCTION

The phenomenon of drag reduction resulting from the presence of long chain, high molecular weight polymers in turbulent flow of liquids has received much attention in the past several decades. Although understanding of the way in which polymers reduce drag has proved elusive, this lack of understanding has not impeded the use of polymer drag reduction for engineering purposes in pipe flows (see the review by Hoyt, 1984). One area receiving little attention is external flows where the practical implementation of polymer drag reduction is complicated by the presence of an unbounded fluid medium. In these flows, the use of polymers requires that the polymer solution be delivered to the flow and the performance of the solution as a drag reducer will depend, to large extent, on the mixing of the polymer with the ambient fluid.

The work of Wells and Spangler (1967) established that the polymer solution had to be in the near-wall region to cause drag reduction. Investigations by Tiederman et al. (1985) and McComb and Rabie (1982) have shown that drag reduction results from the presence of the polymer in the buffer region ($10 < y^+ < 100$). Knowledge of the near-wall structure of drag-reduced turbulent flows is confined primarily to homogeneous flows where polymer concentration is constant and the turbulent structure has been modified throughout the flow. In flows where a polymer solution is injected at the wall, one can examine the evolution of the turbulent structure from the Newtonian

state which exists upstream of the injector, to a drag-reduced state downstream. In this way, the effect of the polymer solution on the near-wall region can be examined in detail and the initial changes to the near-wall turbulent structure caused by the polymer solution can be detected.

Although the evolution of the mean polymer concentration profile downstream of wall injectors has been investigated by various authors, the mass transport processes that govern this evolution have not been examined directly. The Schmidt number for diffusion of polymer solutions in water is high ($Sc > 100$) hence, mass transfer is dominated by turbulent transport mechanisms. Since turbulent transport is convective in nature and the polymer is not a passive scalar, i.e. the turbulence is modified locally by the polymer, mass and momentum transport in injected flows are coupled. In order to model this type of flow, direct measurements of turbulent mass transport and momentum transport are necessary unless one is willing to proceed with adhoc assumptions.

1.1 Objectives

In this study, a turbulent channel flow with polymer injection at the wall was examined. The specific objectives were to determine in detail the modifications to the structure of turbulence caused by the injection of the polymer solution and to quantify the high Schmidt number mixing process which occurs. Realization of these objectives required two-component velocity measurements, detailed information about the polymer concentration field and direct measurements of turbulent mass transport. The velocity field was examined using two-component laser velocimetry. To determine the

concentration field, a laser-induced fluorescence technique was developed to measure instantaneous polymer concentration profiles. For measurement of turbulent mass transport, the concentration measurements were combined simultaneously with laser velocimetry to obtain direct measurements of turbulent mass transport.

In what follows, the behavior of the polymer solutions is discussed, the structure of turbulence in drag-reduced flows is outlined and the relevant work in mixing and dispersion for flows with polymer injection is examined.

1.2 Drag-reducing polymer solutions

Polymer solutions capable of causing drag reduction in turbulent flows are typically non-Newtonian, viscoelastic fluids. The polymer used in this study was an aqueous solution of SEPARAN AP-273, a polyacrylamide manufactured by Dow Chemical. Argumedo et al. (1978), Tsai and Darby (1978) and Cho et al. (1983), among others, have demonstrated that when subjected to steady-shear viscometric flows, this type of polymer solution exhibits shear-thinning behavior: the shear viscosity decreases with increasing shearing strain-rate (dU/dy). Ryskin (1987) showed that, when placed in a purely elongational strain (dU/dx), e.g. flow through an axisymmetric nozzle, the viscosity increased with increasing elongational strain-rate. This "extensional" viscosity can be up to two orders of magnitude larger than the shear viscosity. These results are evidence of the complex constitutive nature of polymer solutions. Constitutive relations which model the steady shear response of the polymer solution have been proposed by Argumedo et al. and Tsai and Darby. Tsai and Darby also modeled the response of the fluid to certain transient inputs. At present these

rheological modeling efforts are at best tentative and have not been implemented in numerical simulations of turbulent flow.

In flows where a polymer solution is injected, the rheology of the resulting water-polymer mixture is also complicated by the presence of concentration variations. In the investigations of Frings (1984) and Bewersdorff (1984) it was shown that when very-high-concentration polymer solutions (i.e. several thousand parts per million) are injected, threads of high-concentration fluid can form which persist for long distances downstream. This nearly "two-phase" behavior is more complex rheologically than flows where the injected concentration is below 1000 ppm and the polymer solution diffuses more readily. To date, there has been no investigation of the effect of non-homogeneous concentration on the rheological properties of polymer solutions.

1.3 Turbulence structure and drag reduction

For Newtonain flows, the turbulence structure is defined relative to the Reynolds averaged Navier-Stokes and continuity equations. For a stationary turbulent flow these are:

$$\overline{U}_j \frac{\partial \overline{U}_i}{\partial x_j} = -\frac{1}{\rho}\frac{\partial \overline{P}}{\partial x_i} + \frac{\partial}{\partial x_j}\left[\nu \frac{\partial \overline{U}_i}{\partial x_j} - \overline{u_i u_j}\right] \tag{1.1}$$

$$\frac{\partial \overline{U}_i}{\partial x_i} = 0 \tag{1.2}$$

The terms $\overline{u_i u_j}$ are unknowns introduced by the averaging process. These unknowns comprise the Reynolds stress tensor and represent transport of "i" component momentum in the "j" direction due to fluctuations in the velocity field. "Turbulence

structure" refers to the spatial variation in the elements of the Reynolds stress tensor and other statistical quantities appearing in Equation 1.1.

In flows where there is an evolving polymer concentration field, the right-hand side of Equation 1.1 could contain additional terms resulting from the non-Newtonian nature of the polymer solution and the unsteady concentration field. Since the exact constitutive equation for the polymer solution has not been determined, the form of these terms is unknown. The mathematical form of the Reynolds stresses (which arise from the advective, left-hand side terms of the momentum equation) is unaffected by the non-Newtonian behavior of the polymer solutions. Although additional terms may be introduced when polymer is present, the importance of the Reynolds stresses is undiminished.

Due to the viscoelastic nature of drag-reducing polymers, measurements of velocity using hot-wire anemometers, hot-film devices or pitot tubes can be grossly in error. This leaves the laser velocimeter as the only viable method for measuring velocity and turbulence statistics. To date most investigations have been restricted to one-component velocity measurements although recent measurements by Luchik and Tiederman (1988), and Willmarth et al. (1987) have quantified drag-reduced flows using two-component measurements. These measurements have been confined to flows with constant polymer concentration.

The turbulence statistics most often measured are profiles of the mean streamwise velocity component. These have been reported Berner and Scrivener (1980), McComb and Rabie (1982), and Bewersdorff (1984) for circular tubes, Rudd (1972) and Logan

(1972) for square tubes and Reischman and Tiederman (1975), Luchik and Tiederman (1988) and Willmarth et al. (1987) for rectangular channels. The effects of drag-reducing additives on the mean velocity profile (normalized with inner variables: $U^+ = \overline{U}/u_\tau$, $y^+ = yu_\tau/\nu$ where $u_\tau = \sqrt{\tau_w/\rho}$ and ν is the kinematic viscosity evaluated at the long time average wall shear rate) are clearly established. The linear sublayer ($y^+ < 8$) remains unaffected and the logarithmic overlap region is displaced toward higher velocities but its slope is unchanged relative to Newtonian flows.

The root mean square (RMS) of the streamwise velocity (u') also exhibits specific trends in drag-reduced flows. In Newtonian flows the peak in u'/u_τ occurs at about $y^+ = 15$; for drag reducing flows this peak is shifted outward in both physical distance and y^+. These changes can be directly related to the changes which occur in the mean velocity profile; an increase in the mean velocity gradient results in an increase in u' and the opposite also holds.

The results presented by Luchik and Tiederman (1988) and Willmarth et al. (1987) show that the RMS of the normal velocity decreases both physically and nondimensionally throughout the viscous sublayer. Similar results were obtained by Logan (1972) but the interpretation of those results was complicated by the presence of secondary flows in the square duct used in that study.

Luchik and Tiederman (1988) also measured the turbulent shear stress, $\overline{uv}$, and found that the location of the peak in $\overline{uv}$ moved outward and the peak value was decreased. Willmarth et al. (1987) found $\overline{uv}$ greatly decreased across the entire flow and proposed the existence of a non-Newtonian retarding force to account for the

discrepancy between the total stress and the sum of the turbulent and mean viscous shear stresses. This behavior was not seen in the experiments of Luchik and Tiederman, where the polymer was mixed uniformly with the flow, but is similar to that presented by Bewersdorff (1984) for pipe flows where a very high concentration polymer solution was injected at the centerline. In Bewersdorff's flow, the solution did not completely mix with the ambient fluid resulting in the presence of high-concentration polymer threads in the flow. This raises the question of whether polymer threads were present in the flow of Willmarth et al.

These studies indicate that the presence of polymers in a turbulent flow results in significant changes in the structure of turbulence which, in turn, cause reduced viscous drag. The mechanism(s) by which the polymer solutions cause these structural changes have not been identified.

1.4 Scalar transport and the dispersion of injected polymer solutions

The conservation of a scalar quantity C in stationary turbulent flow is governed by the Reynolds averaged species conservation equation:

$$\overline{U}_i \frac{\partial \overline{C}}{\partial x_i} = \frac{\partial}{\partial x_i} \left[D_{ab} \frac{\partial \overline{C}}{\partial x_i} - \overline{u_i c} \right] . \tag{1.6}$$

The time-averaging process introduces the unknowns $\overline{u_i c}$. For a developing scalar field in a two-dimensional (on average) boundary layer or channel flow one would usually reduce this equation to its "thin shear layer" (or boundary layer) form:

$$\bar{U}\frac{\partial \bar{C}}{\partial x} + \bar{V}\frac{\partial \bar{C}}{\partial y} = \frac{\partial}{\partial y}\left[D_{ab}\frac{\partial \bar{C}}{\partial y} - \overline{vc}\right] \tag{1.7}$$

The unknown $\overline{vc}$ represents scalar transport in the direction normal to the wall resulting from velocity and concentration fluctuations. Solution of this model equation requires the specification of $\overline{vc}$ as a function of position.

Flows with injection at the wall occur most frequently in film-cooling applications in gas turbines and other harsh environments. The review by Hartnett (1985) shows that the injection flowrates which are typical for film cooling are significantly larger than those which are necessary for polymer drag reduction. This results in the injected fluid extending far into the fully-turbulent portion of the flow. Since this radically alters the near-wall turbulent structure, the physics of the injection process for film cooling are significantly different from those of polymer injection where there is minimal disturbance to the flow.

Other studies of scalar transport in Newtonian flows have been generally restricted to investigations of heat transfer. Hishida et al. (1986) examined a fully developed pipe flow with constant heat flux at the wall. That study showed that mean velocity and temperature profiles were similar and turbulent scalar transport ($\overline{v\theta}$) profiles were similar to those for turbulent momentum transport ($\overline{uv}$). Antonia et al. (1977) examined $\overline{v\theta}$ in a boundary layer at several locations downstream of a step change in wall heat flux. Their results showed that the maximum value of $\overline{v\theta}$ at all locations downstream of the discontinuity was approximately equal to the heat flux at the wall. When distance from the wall was scaled with the thermal boundary layer thickness, there was good agreement between the $\overline{v\theta}$ profiles for all streamwise

locations. No direct comparisons were drawn between $\overline{uv}$ and $\overline{v\theta}$; however, as the thickness of the thermal boundary layer approached that of the momentum boundary layer, the $\overline{v\theta}$ profile was similar to typical behavior of $\overline{uv}$ in boundary layer flows. These results were shown to also be consistent with behavior in flows with a step change in wall temperature.

The invesigations of Hishida et al. and Antonia et al. show that for fully developed flows and boundary layer flows where the thermal boundary layer thickness equals the momentum boundary layer thickness, turbulent scalar transport profiles are similar to turbulent momentum transport profiles. This occurred because, in both studies, the working fluid was air (where the Prandtl number is near unity) and the boundary conditions were similar for the momentum and energy equations. In flows with injection at the wall, this similarity does not exist: The boundary condition at the wall for the species conservation equation specifies zero scalar flux and for mass transport in liquids, the Schmidt number is at least several hundred. These differences together with the fact that the flow is not fully developed make similarity between turbulent mass transport and momentum transport unlikely.

Investigations into the mixing of injected polymer solutions have been limited to the measurement of mean concentration profiles. Latto and El Reidy (1976,1984) measured mean concentration profiles downstream of slot injectors in a flat plate boundary layer and showed that polymer solutions diffuse more slowly than water solutions. An investigation by Collins and Gorton (1976) showed that downstream of the region where large concentration gradients exist, diffusion rates are comparable to

those resulting from plain water injection. Fabula and Burns (1970) measured the mean polymer concentration profile far downstream of a slot injector in a zero pressure gradient boundary layer. They showed that in this region, where the polymer was present across the entire boundary layer, the concentration profile was self-similar.

All these measurements were made using pitot probes and isokinetic sampling techniques. Latto et al. (1981) have shown that measured mean concentrations are always less than actual concentrations in inhomogeneous flows when this measurement technique is used. This is due to the strong dependence of solution viscosity upon concentration.

None of these polymer studies examined turbulent mass transport directly, nor did any attempt to relate the evolution of the concentration field to the changes in the structure of turbulence which result in drag reduction.

1.5 Closure

In the next chapter, the experimental facilities and the apparatus and procedures used for this investigation are discussed. This includes a discussion of the two-component laser velocimeter system used for making high spatial resolution velocity measurements and procedures to eliminate bias errors which can occur with this technique. A laser-induced fluorescence technique for making accurate, high-speed, non-intrusive measurements of scalar concentration profiles is described in detail. And the combination of laser velocimetry and concentration measurements to obtain direct measurements of turbulent mass transport is discussed.

The results from this study are contained in the next four chapters. In Chapter 3, measurements of turbulence structure for the water flow with no injection are presented. These data establish the "standard" character of the basic water flow and serve as a yardstick by which modification to the flow can be measured. Also, a highly accurate method for determining the wall shear stress in fully developed flows is shown. The concentration field in injected flows is discussed in Chapter 4. Time-averaged statistics are presented and the underlying behavior of the concentration field is investigated by examining the time-history of instantaneous concentration profiles. A comparison between the concentration field resulting from polymer injection and that resulting from the injection of dyed water is made. In Chapter 5, the effect of the evolving concentration field on the structure of turbulence is examined. Changes in the mean quantities and Reynolds stresses resulting from the developing concentration field are discussed, and the causes of these changes are inferred from examination of the Reynolds stress transport equations. In these results, the effect of the injection process on turbulence structure is isolated from the modification of the flow by the polymers by examining a flow with water injection. Chapter 6 presents direct measurements of turbulent mass transport for both water injection and polymer injection. These results are compared and the relationship between the velocity and concentration fluctuations is examined in detail. A discussion of issues relevant to modeling these flows is then presented.

The final chapter summarizes the major results and presents conclusions.

CHAPTER 2 - APPARATUS AND PROCEDURES

2.1 Experimental facilities

The water flow loop used in these experiments, shown in Figure 2.1, was driven by four ninety gallon per minute centrifugal pumps operating in parallel yielding a maximum Reynolds number, based on channel height, of about 40 000. At each end of the test section there was a large stilling tank to isolate the test section from any hydrodynamic disturbances in the flow loop. The upstream stilling tank contained a perforated plate followed by a screen and open-cell sponge section and a smooth two-dimensional contraction at the outlet. The inlet of the channel was preceded by a flow straightener consisting of closely packed plastic drinking straws which insured that no large-scale vorticity existed in the channel entry flow. The downstream tank contained a perforated plate to damp out disturbances and a copper coil through which cooling water was passed to maintain the channel water at a constant temperature.

The flow loop had a rectangular-cross-section channel (6.0 cm high by 57.5 cm wide) as the test section. The test section was constructed from one-half inch acrylic and polycarbonate sheet and was more than one hundred channel heights long. Polymer solutions were injected through flush-mounted, angled slots located in both of the 57.5 cm walls of the channel. The injection slots had a width, measured in the streamwise direction, of 2.5 mm and were inclined 25 degrees to the flow direction as

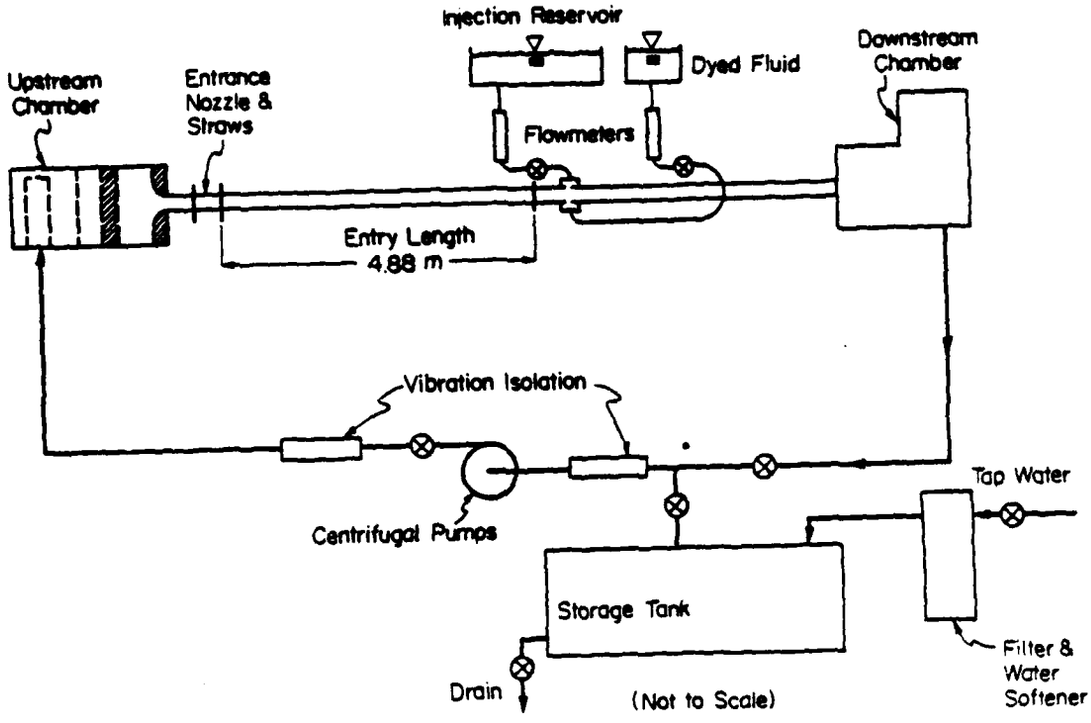

Figure 2.1 Schematic of flow loop.

shown in Figure 2.2. The injectors were located about eighty channel heights downstream of the inlet.

The coordinate system used in the description of the apparatus and presentation of the results is also shown in Figure 2.2. The x-axis is parallel to the flow direction and the y-axis is normal to the flow direction and the long (57.5 cm) dimension of the channel cross section. The origin of this coordinate system is located at the center (mid-span) of the injection slot located in the lower 57.5 cm wall of the channel.

2.2 Polymer solution preparation

These experiments conducted over a period of several months using several different batches of polymer solution. To ensure that the results are comparable, the polymer solutions were prepared using a standard procedure and the batches were checked for repeatability.

The additive was an aqueous solution of SEPARAN AP-273, a polyacrylamide manufactured by Dow Chemical, at a concentration of 700 ppm based on weight. The dry powder was suspended in 300 mℓ of isopropyl alcohol and mixed into filtered, deaerated tap water at about 38 °C using a magnetic stirrer. The concentration of this initial mixture was about 5000 ppm and it was allowed to hydrate for 12 to 24 hours. This solution was then diluted to the desired concentration using filtered tap water and allowed to hydrate for 12 to 24 hours before using.

The repeatability of the polymer solutions was checked in two ways. The steady shear viscosity was checked over a range of shear rates using a Brookfield LVT-SCP3

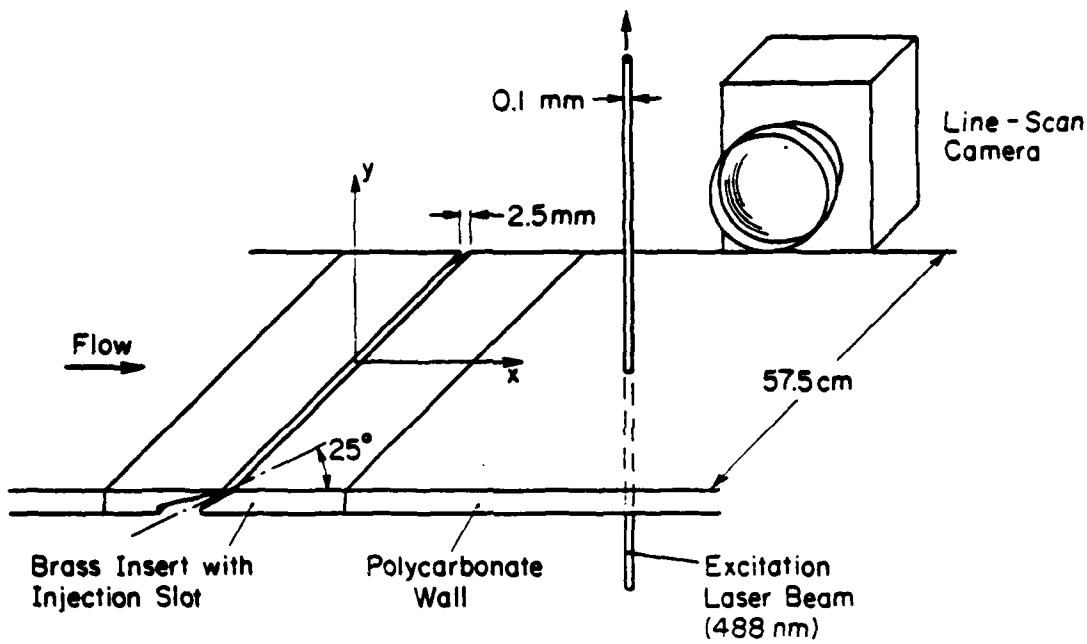

Figure 2.2 Injection slot and optical arrangement.

cone and plate viscometer. Also, samples of each batch were diluted to 100 ppm and drag reduction was measured in a 1.405 cm diameter tube for a range of flowrates. Only polymer solutions which exhibited reasonable consistency in these two measures were used.

2.3 Velocity measurements

2.3.1 Two-component laser velocimeter system

The transmitting optics consisted of a Thermo-Systems Incorporated (TSI) model 9100-8 laser velocimeter system incorporating a Lexel model 85.5 500 mW argon-ion laser. This is a two-component, three-beam system where velocities are measured using one blue (488 nm) beam, one green (514.5 nm) beam, and a blue-green beam containing both wavelengths. Both channels were frequency shifted 40 MHz using a single Bragg cell ahead of the color separator. The beam spacing was 25 mm and the beams were expanded to 2.5 mm and focused with a 250 mm transmitting lens.

Modifications to the standard TSI 9100-8 system consisted of the following: The beam displacer in the output end of the model 9112-1 dichroic color separator was rotated 90 degrees to place the green beam at 90 degrees from the blue beam. After the color separator, the blue-green beam was displaced to the optical axis using a TSI 9174 50 mm beam displacer. These changes placed the blue-green beam on the optical axis and the blue beam and green beam at nominally ± 45 degrees from vertical. In this way, velocity components at about ± 45 degrees to the flow direction were measured. With this system the included angle between the beams can deviate from 90 degrees by

as much as 4 degrees. This is accounted for in the data analysis procedure discussed below.

For this system the measured velocity components are in a plane which is parallel to the flow direction but inclined at an angle of about 3 degrees relative to the wall-normal direction. This introduces some error into the measurement of quantities related to the normal velocity. For the second moment of the normal velocity $\overline{v^2}$,

$$\overline{v_m^2} = \overline{v^2}\cos^2\alpha + \overline{w^2}\sin^2\alpha \tag{2.1}$$

where $\overline{v_m^2}$ is the second moment of the measured velocity component and α is the angle of inclination from the wall-normal direction. For the turbulent shear stress $\overline{uv}$

$$\overline{uv}_m = \overline{uv}\cos\alpha\,. \tag{2.2}$$

Thus the error introduced in $\overline{uv}$ for $\alpha = 3$ degrees is about 0.1 percent which is considerably smaller than the uncertainty in $\overline{uv}_m$. The effect on the second moment of the normal velocity can be evaluated using the near-wall values of $\overline{v^2}$ and $\overline{w^2}$ from Kim et al. (1987). Table 2.1 shows the resulting error in the measured value of $v' = \sqrt{\overline{v^2}}$ for $\alpha = 3$ degrees. The resulting error in v' is only significant very near the wall ($y^+ \leq 5$).

The optics table was equipped to translate the measurement volume in three orthogonal directions. The beams were translated in the vertical (y) direction using a pair of enhanced aluminum mirrors. The upper mirror and the transmitting lens were mounted on a vertical translation stage which was positioned using two two-inch micrometers (see Luchik, 1985). The entire vertical traverse assembly was mounted

Table 2.1 Estimated error in wall-normal root-mean-square velocities from results of Kim et al. (1987).

y^+	$\frac{v'_m}{v'}$	%error
1.344	3.8158	281.6
1.934	1.5876	58.8
2.630	1.2829	28.3
3.433	1.1517	15.2
4.341	1.0432	4.2
5.354	1.0287	2.9
6.472	1.0209	2.1
7.639	1.0152	1.5
9.018	1.0113	1.1
10.440	1.0116	1.1

on a translation stage which moved the measurement volume parallel to the optical axis (z-direction). The optics table was located on translation stages which allowed several inches of travel in the streamwise (x) direction.

The location of the measurement volume relative to the wall was determined using a TSI model 9140 receiving optics assembly and eyepiece installed in the transmitting optics train. By moving the probe volume toward the wall, the y-location where the image of the probe volume intersected the wall could be determined to within about one-half the probe volume diameter. This position was then used as a reference for all subsequent vertical location measurements.

The beam geometry is defined by the transmitting optics and determines exactly which components of velocity are measured and the relationship between measured Doppler frequency and velocity. With the beams in air, a screen was placed a known distance several feet from the beam crossing point and oriented normal to the optical

axis. The points where the three beams intersected the screen were marked and the lengths of the sides of the triangle formed by these points was measured. From these measurements and the known distance from the beam crossing point, the half-angle of each beam pair was calculated and used to determine the fringe spacing for each channel. The lengths of the three sides of this triangle are used to calculate the included angle between the measured velocity components which in turn is used to calculate true orthogonal velocity components from the measured velocities.

The receiving optics were standard TSI two-component items. Scattered light was collected using a 250 mm focal length lens. A 2.27X telescope was inserted behind the collection lens to increase the spatial resolution of the receiving optics. A 50 μm aperture was used in a TSI 9143 field-stop assembly to ensure spatial coincidence of the two measured velocities. The light passing through the aperture was re-collimated and passed through a dichroic color separator. The separate colors were bandpass filtered and focused on two photomultiplier tubes.

The spatial resolution of the measurement system is defined by both the transmitting optics and the receiving optics and their relative orientation. The axis of the receiving optics was located in the y-z plane at an angle of 9.5 degrees from the axis of the transmitting optics. For this orientation, the extent of the probe volume in the y-direction is defined by the diameter of the beam intersection ($l_y = 63$ μm). The x dimension of the measurement volume is determined by the diameter of the field of view of the receiving optics ($l_x = 55$ μm). The length of the probe volume along the z-axis, defined by the field of view of the receiving optics and the collection angle, was

$l_z = 330\ \mu m$. Non-dimensionalizing with the shear velocity and kinematic viscosity of the basic water flow yields: $l_x^+ = 1.6$, $l_y^+ = 1.8$, and $l_z^+ = 9.6$.

The photomultiplier output for each channel was high-pass filtered at 25 MHz to remove the pedestal frequencies and was electronically down-mixed to yield an effective shift frequency of 0.5 MHz using a TSI model 9186 down-mixer. The frequency of the down-mixed signals was determined using two TSI model 1980 counter processors. Signals were high-limit and low-limit filtered at 1 MHz and 30 kHz respectively resulting in a pass-band equivalent to ± 2.5 m/s. (The center-line velocity for the water flow was 0.65 m/s.) The Schmitt-trigger threshold in these counters is 50 mV so amplifier gain was adjusted to maintain noise levels below 10–15 mV. Maximum-signal amplitudes of about 1 V resulted in signal-to-noise ratios up to 60:1. The elapsed time for 8 zero crossings was measured. Validation required less than three percent difference in the period determined from the total time and the period determined from the time for 5 zero crossings.

Velocity data were acquired using a Masscomp 5520 microcomputer communicating with the TSI model 1998 interface through a Masscomp PI16F fast parallel interface. Data were not transferred to the computer unless measurements were made on both channels within a predetermined coincidence window. The length of the coincidence window was set equal to the estimated minimum transit time through the probe volume (about 100 μs).

2.3.2 Seeding, sampling and velocity bias

The major drawback to measuring fluid velocities using laser velocimetry is that the fluid velocity is not measured directly; the measured velocity is that of particles suspended in the fluid. To obtain accurate measurements one must ensure that there is no more than one particle in the measurement volume at any given time. One must also take care to ensure that the estimated velocity statistics are not affected by fringe bias, filter bias, or velocity bias (see Edwards, 1987).

For this study the flow was seeded with homogenized whole milk which contains fat particles about 0.3 μm in diameter. To insure that the flow was uniformly seeded, the injected fluids were seeded at the same concentration as the water in the flow loop. In the case of the polymer solutions, this was accomplished by adding the seed to the water used to dilute the solution to its final concentration.

The maximum particle arrival rate achieveable with a given laser velocimeter in a given flow (with only one particle in the measurement volume on average) can be estimated by dividing the velocity of the flow by the diameter of the probe volume. For the flow in question this results in a particle arrival rate of about 4 kHz to 8 kHz, depending on position in the flow. For the results presented here, the water in the flow loop was prepared by filtering with a diatomaceous earth filter to remove the natural hydrosol present in the water. The water was then seeded with whole milk at a concentration of 15 mℓ/1000 ℓ which resulted in maximum validation rates of about 2 kHz. This insured that no more than one particle was in the probe volume at any given time.

Fringe bias was overcome by frequency shifting. The effective fringe velocity (after down-mixing) was more than three times the maximum velocity in the flow. This provided almost uniform angular response for the velocity measurements. The possibility of filter bias was eliminated by setting the filters in the signal processors to yield a pass-band equivalent to $\pm$ 2.5 m/s ($\pm$ 3 U_o).

Velocity bias occurs because there is a higher probability of measuring a high velocity particle than a low velocity particle (see McLaughlin and Tiederman, 1973). For the flow in question, which exhibits thirty to forty percent turbulence intensity near the wall, the error in the estimate of the mean velocity would be up to fifteen percent if this effect was ignored. For the two-component measurements, velocity bias was eliminated using the fixed-waiting-time sampling method. In this method the data acquisition system is inhibited for a fixed amount of time between one realization and the next. The Kolmogorov time scale is representative of the smallest or dissipation scales in the flow. (For isotropic turbulence, this time scale is generally smaller than the Eulerian microscale.) For the flow in question, the Kolmogorov time scale was estimated by assuming that dissipation of turbulence kinetic energy was equal to production at the production peak. The validation rate was maintained at about five times the Kolmogorov frequency and the inhibit time was ten times the inverse of the validation rate. Based on the results of Gould et al. (1988), this approach should be adequate to eliminate velocity bias effects from the mean quantities and it is assumed that the effects on higher statistical moments are also eliminated.

For the water flow results presented in Chapter 3, all statistics were based on ensembles of 25 000 data realizations. Statistics for the flows with water and polymer injection (Chapter 5) were calculated using ensembles of 10 000 realizations.

2.4 Concentration measurements

Time-resolved concentration measurements were obtained in a manner similar to that used by Koochesfahani and Dimotakis (1986). The injected fluid was marked with a fluorescent dye and the spatial distribution of the intensity of fluoresced light emitted from a laser beam directed normal to the channel wall was measured. The dye concentration at a point was determined from the fluorescent light intensity and the injectant concentration was inferred from the measured dye concentration. For turbulent flows, where dispersion occurs due to convective mixing, the "turbulent" mass diffusivity is typically two or more orders of magnitude larger than the molecular mass diffusivity. This indicates that the time scale for molecular diffusion is more than one hundred times the timescale for "turbulent diffusion", hence the effect of molecular diffusion will be small and the dye concentration will yield a good estimate of the polymer concentration.

2.4.1 Analysis

For light propagating in an absorbing medium, the change in intensity, dI_e, over the differential distance dy is

$$dI_e = -kI_e\, dy \tag{2.3}$$

where k is the extinction coefficient for the medium. In this case, I_e represents the intensity of the of the laser beam used to excite the dye. Integration of Equation 2.3 from the point where the beam enters the medium (y = 0) to the point in question (y) yields

$$I_e(y) = I_o \; e^{-\int_0^y k(r)\,dr} \tag{2.4}$$

where $I_o = I_e(0)$. The intensity of the fluoresced light, I, emitted from a differential length, ds, along the excitation beam is some fraction of the light absorbed over that distance,

$$I = \alpha \, dI_e = \alpha \, k I_e \, ds \tag{2.5}$$

where α is a constant. Hence, for a small segment of the excitation laser beam of length d at location y,

$$I(y) = \alpha k(y) I_e(y) d \, . \tag{2.6}$$

For fluorescent dyes in the range of concentrations of interest here, the extinction coefficient is proportional to the dye concentration

$$k = \beta \, C \, . \tag{2.7}$$

Combining the above equations yields

$$I(y) = \alpha \, \beta C(y) \, I_o \, e^{-\int_0^y \beta C(r)\,dr} \, d \, . \tag{2.8}$$

This equation relates the fluorescence intensity from a discreet segment of the laser beam to the initial laser beam intensity and the dye concentration along the beam path.

Solving for the local concentration C(y) yields

$$C(y) = \frac{I(y)}{I_o \alpha \beta d} \, e^{\int_0^y \beta C(r)\, dr} . \tag{2.9}$$

If the dye concentration is considered constant over a distance s measured from the midpoint between segments i-1 and i to the midpoint between segments i and i+1, then the integration in the above equation can be written as a summation. The average dye concentration over the segment located at y_n, (the n^{th} segment of the laser beam), is given by

$$C_n = C(y_n) = \frac{I_n}{I_o \alpha \beta d} \, e^{\sum_{i=1}^{n-1} \beta C_i s} \tag{2.10}$$

where $I_n = I(y_n)$. This result can be rewritten as

$$C_n = \frac{1}{I_o \alpha \beta d} \left[\prod_{i=1}^{n-1} e^{\beta C_i s} \right] \, I_n . \tag{2.11}$$

This last equation expresses the dye concentration at the n^{th} location along the beam path in terms of the properties of the dye, the dye concentration at the previous n-1 locations, and the intensity of the fluorescent emission from a small segment of the excitation beam. Also required are the values of d and s which are determined by the detector used for the fluorescence intensity measurements.

For these experiments the fluorescence intensity distribution along the path of the excitation laser beam was measured using a Reticon camera incorporating a line array of photodiodes. In developing working equations, the characteristics of the photodiode array and the imaging optics must be considered. The voltage for a given element of

the array increases linearly with incident light intensity from a dark-level voltage. Both the dark-level voltage and the sensitivity vary slightly from element to element. In addition, since measurements were made near a wall, the fraction of the total fluorescent emission collected by the camera lens varied with position in the field of view.

The voltage for an element of the photodiode array is related to the fluorescent intensity at the corresponding point in the field of view by

$$V_n = a_n b_n I_n + V_{dn} \tag{2.12}$$

where a_n is the fraction of the emitted light which is incident on the element, b_n is the sensitivity of the element and V_{dn} is the dark voltage for the element. Combining this result with Equation 2.11 yields

$$C_n = \left[\frac{1}{I_o \alpha \beta d a_n b_n} \right] \left[\prod_{i=1}^{n-1} e^{\beta C_i s} \right] (V_n - V_{dn}) \tag{2.13}$$

which relates concentration to measured voltage. Examination of this equation reveals that the term in brackets depends entirely on known constants and element number. Hence, this term can be replaced by a single variable A_n, resulting in

$$C_n = \frac{1}{A_n} \left[\prod_{i=1}^{n-1} e^{\beta C_i s} \right] (V_n - V_{dn}) . \tag{2.14}$$

The single element-dependent constant is then determined by placing a known dye concentration in the flow field and measuring the array element voltages.

2.4.2 Optical arrangement

For these experiments the fluorescence intensity distribution along the path of the excitation laser beam was measured using a Reticon line-scan camera incorporating a 256 element linear photodiode array. The elements of the photodiode array are 25 μm by 425 μm and are located on 50 μm centers. For all streamwise measurement stations in the flow with water injection and the first measurement station in the flow with polymer injection, the magnification was set to yield effective measurement volumes which were spaced 60.5 μm apart and measured 30.3 μm in the direction normal to the wall. The magnification at the other streamwise locations for the polymer flow resulted in 35.0 μm measurement volumes spaced 70.0 μm apart.

The blue (488 nm) line from a Lexel model 85.5 argon-ion laser was used to excite the dye. The diameter of the excitation beam determined the spatial resolution of the measurement in the streamwise and spanwise directions. Focusing the excitation beam with a 200 mm focal length lens yielded a beam diameter of 115 ± 5 μm across the field of view.

2.4.3 Data acquisition

All timing and data acquisition tasks were accomplished using a Masscomp 5520 micro-computer. This computer has 8 Mbytes of random access memory available for data acquisition and sufficient hardware floating point calculation capability and graphics capability to analyze data on-line during the course of an experiment. Data were acquired using a 12 bit A/D converter capable of one million conversions per

signals were generated using the clock module of the computer.

The Reticon line-scan camera requires a start signal to begin each scan of the array and a clock signal to drive the multiplexer which samples the individual elements. The output from each element is in the form of a dark-level voltage plus a voltage proportional to the integrated intensity of the light incident on the element during the time between successive scans of the array. Hence, the exposure time for each intensity profile is equal to the time between start signals. The maximum output voltage is two volts and the dark level voltage is typically about 10 mV.

For all measurements presented here the camera clock signal frequency was set to 857 kHz. During water injection, the array scan rate (the frequency at which start signals were delivered) was 3 kHz yielding an exposure time of 333 microseconds. Every sixth scan of the array was digitized resulting in a sampling rate of 500 Hz. For the flow with polymer injection, the array scan rate was 2 kHz yielding an exposure time of 500 microseconds. Two sampling rates were used in the polymer injection flow. To calculate long-time averaged statistics, every tenth scan of the array was digitized yielding a sampling rate of 200 Hz. For time-resolved measurements, every second scan of the array was digitized for a sampling rate of 1000 Hz.

2.4.4 Concentration measurement procedure

Prior to the concentration measurements the injected fluid was dyed with fluorescein disodium salt at a molar concentration of about 10^{-6}. The water in the flow loop was given a dye concentration of about 3×10^{-7} M for purposes of calibration.

The fluorescence of the fluorescein dye is very sensitive to pH variations (see Walker, 1986). For the water injection measurements, this posed no problem since the injected fluid was the same as the fluid in the channel. However, the polymer solutions had a pH of 8.1 whereas the channel water had a pH of 7.4. To obtain accurate polymer concentration measurements the pH of the channel water was adjusted to match the polymer solution by adding sodium hydroxide to the water.

The fluorescent emission from the dye in the polymer solution was observed to decrease steadily with time. Since this behavior was not seen when water was the solvent, it is believed that the polymers promoted the formation of non-fluorescing aggregates of dye molecules. Gentle stirring of the dyed polymer solution slowed this process enough that there was negligible change in fluorescence during the course of an experiment.

The camera was positioned and aligned visually with the excitation beam using the through-the-lens viewfinder. Final alignment was accomplished by observing the camera output on an oscilloscope and adjusting the vertical camera position to place the maximum measured light level, which occurs where the beam first enters the flowfield, at the first photodiode.

All dye concentrations were determined using an attenuation cell. This cell allowed the passage of a laser beam through a cavity in which a fluid, either the injectant or water from the flow loop, was flowing. By measuring the attenuation of a laser beam passing through the cell, the dye concentration of the fluid could be accurately determined. The attenuation measurement was performed using a Lexel

model 504 laser power meter. In this way, the dye concentration of the injectant was measured prior to an experiment and the dye concentration of the channel water was monitored during the experiment.

To avoid buildup of dye in the flow loop, dyed fluid was injected through only the center 60% of the lower injection slot and undyed fluid was injected through the outer 20% on each end. Undyed fluid was injected through the slot in the top channel wall. This combination resulted in the average dye concentration of the injected fluid being nearly equal to the background concentration in the channel and thus kept the background concentration relatively constant.

Since there was a small amount of fluctuation in the laser light intensity level (about one percent at a frequency of about 50 Hz), the beam was sampled before entering the test section and a photodiode was used to monitor the laser intensity during the fluorescence measurements. The signal from this photodiode was sampled and stored with each scan of the photodiode array in the camera. This information was used to correct all fluorescence measurements for fluctuations in the excitation source intensity.

Three separate measurements with the photodiode array were required for each data set. The first was a dark-level measurement in which 1000 scans of the array were digitized with the lens aperture covered and then the average dark-level voltage for each element was calculated and stored. Simultaneously, the dark level for the beam-sampler photodiode was measured and the information was stored. Next, the fluorescence intensity resulting from the presence of dye in the channel water was

measured with the camera and the dye concentration of the water in the flow loop was determined using the attenuation cell. These measurement allowed calculation of the constants relating the voltage from each element of the photodiode array to the dye concentration in the field of view. Finally, the fluorescence intensity was measured during injection with the photodiode array. These steps were repeated at each streamwise location and for the different fluids injected.

All concentration statistics were calculated using ensembles of 10 000 realizations.

2.4.5 Verification

To verify the accuracy of the concentration measurement technique, dyed water was injected at a flow rate large enough to establish a concentration boundary layer about 5 mm thick along one wall of the channel. The intensity of the attenuated laser beam leaving the test section was measured along with the fluorescence intensity profiles along the beam. The average concentration along the beam path could then be deduced from the measured attenuation of the excitation laser beam and from integration of the measured concentration profile. The correlation coefficient for these two independent measurements of space-averaged concentration was 0.97 verifying the accuracy of the concentration profile measurements. A portion of the time history of these two measurements is shown in Figure 2.3.

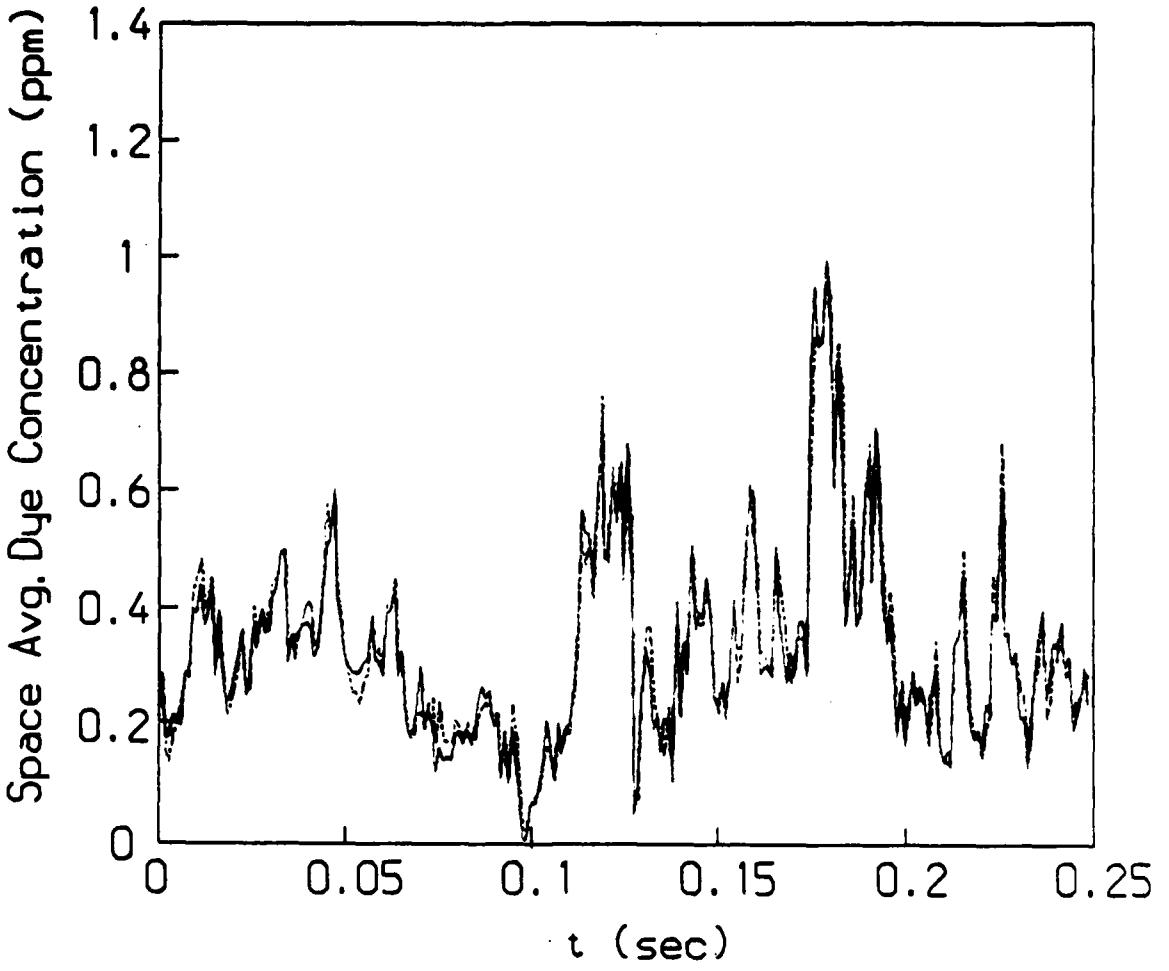

Figure 2.3 Space-averaged dye concentration determined by: ———— , attenuation; – – – – , integration of measured dye concentration profile.

2.5 Simultaneous velocity and concentration measurements

Simultaneous measurements of normal velocity and concentration at a point were accomplished by combining the laser induced fluorescence (LIF) concentration measurement technique described above with a single-component laser velocimeter. When combining these two techniques, two considerations are paramount: the beams for the laser velocimeter must not affect the concentration measurements; and the scattered light for the velocity measurements must not be overwhelmed by the fluorescent emission from the dye. In practice, these goals were accomplished by using a helium-neon laser for the velocity measurements. The dye used for the LIF measurements does not absorb light in the red portion of the spectrum, hence the helium-neon laser did not excite the dye and contaminate the concentration measurements. The fluorescent emission from the dye is primarily in the green-yellow portion of the spectrum, away from the helium-neon wavelength and the two signals were separated effectively using an optical filter.

2.5.1 One-component laser velocimeter system

The transmitting optics for the one-component laser velocimeter consisted of optics from the previously described TSI model 9100-8 system used in conjunction with a Spectra-Physics Inc. model 106-1 10 mW helium-neon laser. The optical arrangement used is shown schematically in Figure 2.3. A TSI model 9115-1 beam splitter, set for reference-beam operation, was used to create two equal-intensity, orthogonally polarized beams. The plane of the beams was oriented to measure the vertical (y-component) velocity. The polarization of one beam was rotated using a

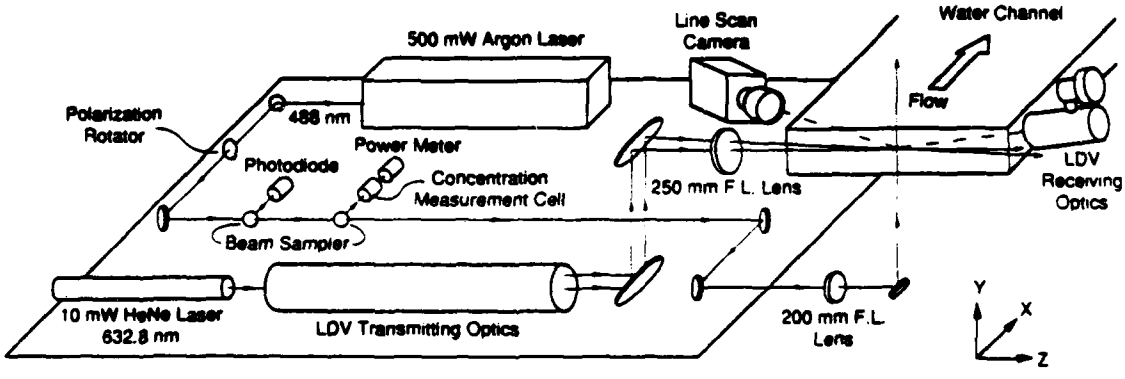

Figure 2.4 Schematic of optics for simultaneous velocity and concentration measurement.

quarter-wave retarder to match that of the other. One beam was frequency shifted 40 MHz using a TSI model 9182-12 Bragg cell. The lower beam of the pair was displaced to the optical axis using a TSI 9174 beam displacer, to enable measurements in close proximity to the lower wall of the channel. The beam spacing was 25 mm and the beams were expanded to 1.54 mm and focused with a 250 mm transmitting lens. As with the two-component system the measured velocity component is inclined at about 3 degrees to the wall-normal direction and the errors introduced are similarly small.

The receiving optics were the same as the two-component system except they incorporated only one photomultiplier tube and a narrow bandpass optical filter centered at 632.8 nm. The spatial resolution of the measurement system was unchanged in the x- and z-directions, but the smaller beam diameter and longer wavelength of the helium-neon system resulted in a vertical probe volume dimension (l_y) of 130 μm ($l_y^+ = 3.7$).

The photomultiplier output was high-pass filtered at 25 MHz to remove the pedestal frequencies and was electronically down-mixed to yield an effective shift frequency of 50 kHz using a TSI model 9186 down-mixer. The frequency of the down-mixed signals was determined using a TSI model 1980 counter-type signal processor. Signals were high-limit and low-limit filtered at 100 kHz and 3 kHz respectively resulting in a pass-band equivalent to ±0.3 m/s. (The maximum RMS normal velocity was about 0.03 m/s.) Signal quality and validation requirements were the same as outlined for the two-component system. An analog velocity trace was generated using a TSI model 1988 digital to analog converter.

Seeding was the same for this system as for the two-component system and the potential sources of bias were either eliminated or minimized. Fringe bias was eliminated by frequency shifting. The resulting fringe velocity was more than ten times the maximum normal-velocity component and it was large enough to obtain measurements on the particles traveling in the streamwise direction at the maximum streamwise velocity. Velocity bias was again eliminated by controlled sampling of the processor output. Instead of fixed-waiting-time sampling, as used for the two-component measurements, the analog velocity signal was sampled at equal time intervals. As before, the validation rate was about five times the Kolmogorov frequency and the sampling rate was set at one-tenth the validation rate. According to Edwards (1987) this is adequate to eliminate velocity bias.

2.5.2 Experimental procedure

In performing this measurement, two conditions had to be satisfied. The measurements of concentration and velocity must be made at the same point in space; they must also occur at essentially the same point in time.

The procedure used to ensure spatial coincidence of the velocity and concentration measurements consisted of the following steps. Using a TSI model 9140 receiving optics assembly and eyepiece installed in the transmitting optics train, an image of the probe volume was focused on the eyepiece reticule and aligned with the reticule cross-hairs. The excitation beam for the concentration measurements was then adjusted so that it remained sharply focused on the reticule and centered on the cross-hairs throughout the vertical travel of the transmitting optics. The line-scan camera was

then aligned and focused on the excitation beam. The wall location was established with the laser velocimeter using the procedure outlined for the two-component system. The exact vertical position of the concentration measurement volumes was determined by increasing the integration time of the video camera until the laser velocimeter beam crossing registered a measurable voltage on the camera output. Determining the camera element numbers which corresponded to two known positions of the beam crossing accurately established the position of the concentration measurement volumes relative to the channel wall.

The velocity signal was an additional analog channel for the A/D converter and the velocity was sampled once for each intensity profile digitized. A block diagram of the electronics is shown in Figure 2.4. The integration time for the concentration measurements was 500 μs which is one-fifth the estimated smallest timescale in the flow. This also corresponds to the average time between validations for the velocity measurements. This indicates that on average there was one velocity realization per concentration profile measurement thus ensuring good temporal coincidence. Data were acquired at a rate of 200 Hz by digitizing every tenth concentration profile measurement and ensembles of 10 000 data points were used to calculate statistics.

2.6 Data analysis

The calculation of statistical quantities was the primary data analysis task for most of the quantities measured in this study. For most of these quantities, this process is straightforward. However, the two-component laser velocimeter data required somewhat more processing and warrants a more detailed discussion. The analysis of

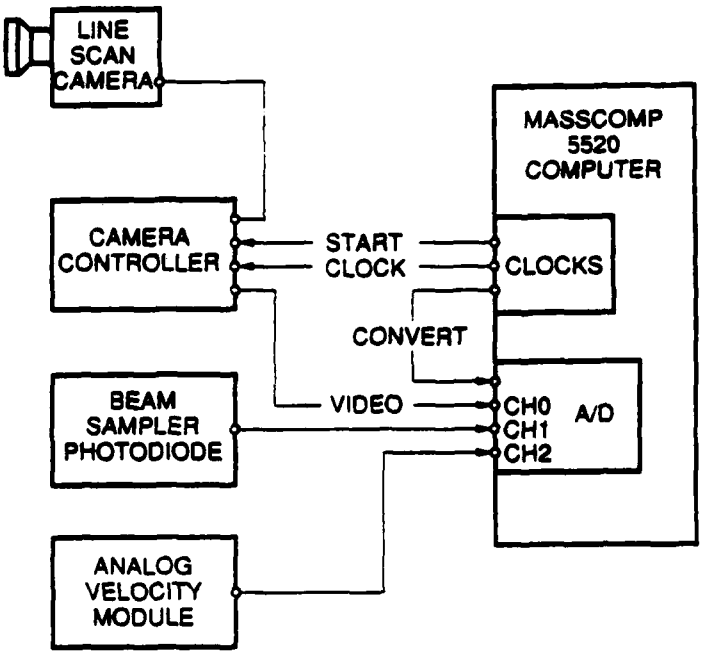

Figure 2.5 Block diagram of electronics for simultaneous velocity and concentration measurement.

these velocity data can be described as several discrete steps, although in practice some of these were done concurrently to reduce computation time.

The individual velocities, U'_1 and U'_2, measured on each channel were calculated. Each U'_1,U'_2 pair was resolved into precisely orthogonal velocity components U_1 and U_2 as follows:

$$U_1 = U'_1 \tag{2.15}$$

$$U_2 = \frac{1}{\sin\theta_i} U'_2 - \frac{1}{\tan\theta_i} U'_1. \tag{2.16}$$

In these equations, θ_i is the angle between the measured velocity components determined from the beam geometry measurements.

All statistics were calculated using the orthogonal U_1, U_2 components. The orientation of these velocity components relative to the flow direction was determined from the velocity measurements themselves. For any given θ measured relative to the flow direction

$$U = U_2\cos\theta + U_1\sin\theta \tag{2.17}$$

$$V = U_2\sin\theta - U_1\cos\theta. \tag{2.18}$$

Time-averaging Equation 2.18 and setting $\overline{V} = 0$ yields

$$\theta = \mathrm{Tan}^{-1}\left[\frac{\overline{U}_1}{\overline{U}_2}\right]. \tag{2.19}$$

The value of θ was determined from measurements in the outer flow (where maximum signal quality was attained) and this value was used at all y-locations. The use of one

value at all y-locations resulted in average normal-velocities which were equal to zero within the uncertainty of the normal-velocity measurement.

Equations 2.17 and 2.18 can be used to calculate values of $\overline{U}$ and $\overline{V}$ in the rotated coordinate system. Calculation of the second moments in the rotated coordinate system is more complicated. The appropriate relationships are:

$$\overline{u^2} = \overline{u_1^2}\sin^2\theta + \overline{u_2^2}\cos^2\theta + 2\overline{u_1 u_2}\cos\theta\sin\theta \tag{2.20}$$

$$\overline{v^2} = \overline{u_1^2}\cos^2\theta + \overline{u_2^2}\sin^2\theta - 2\overline{u_1 u_2}\cos\theta\sin\theta \tag{2.21}$$

$$\overline{uv} = \left(\overline{u_2^2} - \overline{u_1^2}\right)\sin\theta\cos\theta + \overline{u_1 u_2}\left(\sin^2\theta - \cos^2\theta\right) \tag{2.22}$$

The derivation of these relationships are given in Appendix A.

The calculation of some quantities required either integration of the statistical quantities across the channel half-height or differentiation of quantities at a point in the flow. Integrations were done using the trapezoidal rule and assuming zero velocity at the wall. Since the spaces between the locations of the measured velocities varied with distance from the wall, derivatives were defined as the average of the one-sided finite difference approximations on either side of the point in question. At the first and last data point in a profile, the derivatives were set equal to the one-sided finite difference approximations.

The determination of wall shear stress can be done in several different ways. For fully developed duct flows, the average wall shear stress is proportional to the pressure gradient. If the wall shear stress is constant around the perimeter of the duct (as it is in a circular pipe) then this method is uncomplicated. In rectangular channels, the wall

shear stress is not constant around the perimeter and locally the wall shear stress can deviate from the average. The local wall shear stress can be determined from mean velocity measurements in two ways: Estimating the mean velocity gradient at the wall or estimating the slope of the logarithmic portion of the mean velocity profile. Both of these methods use only a limited amount of data in a small portion of the flow.

In these experiments, the shear velocity $u_\tau = \sqrt{\tau_w/\rho}$ for the water flow with no injection was determined using the fact that the total shear stress (the sum of the mean viscous and turbulent shear stress) must be a linear function of distance from the wall for a fully developed flow:

$$\tau_{total} = \mu\frac{d\overline{U}}{dy} - \rho\overline{uv} = \tau_{wall}(1-y/a) \tag{2.23}$$

where a is the channel half-height. Rearranging yields

$$\tau_{wall} = \frac{\mu\frac{d\overline{U}}{dy} - \rho\overline{uv}}{(1-y/a)}. \tag{2.24}$$

Using the definition of shear velocity, $u_\tau = \sqrt{\tau_w/\rho}$ results in

$$u_\tau = u_\tau(y) = \left[\frac{\nu\frac{d\overline{U}}{dy} - \overline{uv}}{(1-y/a)}\right]^{1/2} \tag{2.25}$$

which expresses u_τ as a function of distance from the wall. The shear velocity (which is a constant) at each y-location is determined using the measured values of $\overline{uv}$ and the estimated values of the mean velocity gradient for each measurement point in the flow. These values are then averaged to determine the shear velocity for the flow.

In the following chapters, experimental data will be presented. For mean and and root-mean-square statistics, the uncertainty in the estimated quantity is comparable to the size of the plotting symbol used. For statistics such as $\overline{uv}$ and $\overline{vc}$, the uncertainty estimates are indicated by error bands on a few representative points. These estimates are at the 95 percent confidence level and their determination is discussed in Appendix B.

CHAPTER 3 - WATER FLOW RESULTS

Measurements in the water flow with no injection were made 100 mm downstream of the injector. These results are presented to verify the "standard" nature of the water flow and as a reference for measurements made during injection. This type of flow has been well studied by many investigators. Hussain and Reynolds (1975) performed one-component hot-wire velocity measurements in an air flow in a 32:1 aspect ratio channel which minimized end-wall effects. Kreplin and Eckelmann (1979) examined the near-wall structure of a oil channel flow where, due to the high viscosity, excellent spatial resolution was obtained with hot film probes. The thesis of Wei (1987) shows high spatial resolution, two-component laser velocimeter measurements over a range of Reynolds numbers. Recently, Kim et al. (1987) presented results from a full numerical simulation of turbulent channel flow.

3.1 Experimental conditions

Integral parameters were calculated and are presented in Table 3.1 along with the values of the major flow variables. Integration of the mean velocity profile yielded a mass-averaged velocity of 0.574 m/s. The Reynolds number based on mass-averaged velocity and channel height was 36 000 and the momentum thickness Reynolds number was 1780.

Table 3.1 Experimental conditions for water flow with no injection.

$U_m = 0.574$ m/s	$h = 60.0 \times 10^{-3}$ m
$U_o = 0.651$ m/s	$\nu = 0.957 \times 10^{-6}$ m^2/s
$u_\tau = 27.6 \times 10^{-3}$ m/s	$Re_h = \frac{U_m h}{\nu} = 36\,000$
$\delta^* = 3.45 \times 10^{-3}$ m	$Re_\delta = \frac{U_o h}{2\nu} = 20\,400$
$\theta = 2.61 \times 10^{-3}$ m	$Re_\theta = \frac{U_o h}{\nu} = 1770$

The shear velocity u_τ for the water flow with no injection was determined using the linear variation of total shear stress. Figure 3.1 shows the variation of calculated shear velocity with distance above the wall. The value of the shear velocity, determined by averaging these values, was 0.0276 ± 0.0010 m/s at 95 per cent confidence. This is equivalent to a strain rate of 798 s^{-1} at the wall and a viscous length ν/u_τ of 0.0346 mm. Therefore, $y^+ = 867$ at the channel centerline.

Since the flow is fully developed, static pressure drop should be proportional to the wall shear stress (if one assumes that this high-aspect-ratio channel approximates flow between infinite parallel plates). The value of shear velocity calculated from the static pressure drop is about ten percent higher than the value determined from the total shear stress due to the presence of secondary flows in the channel corners.

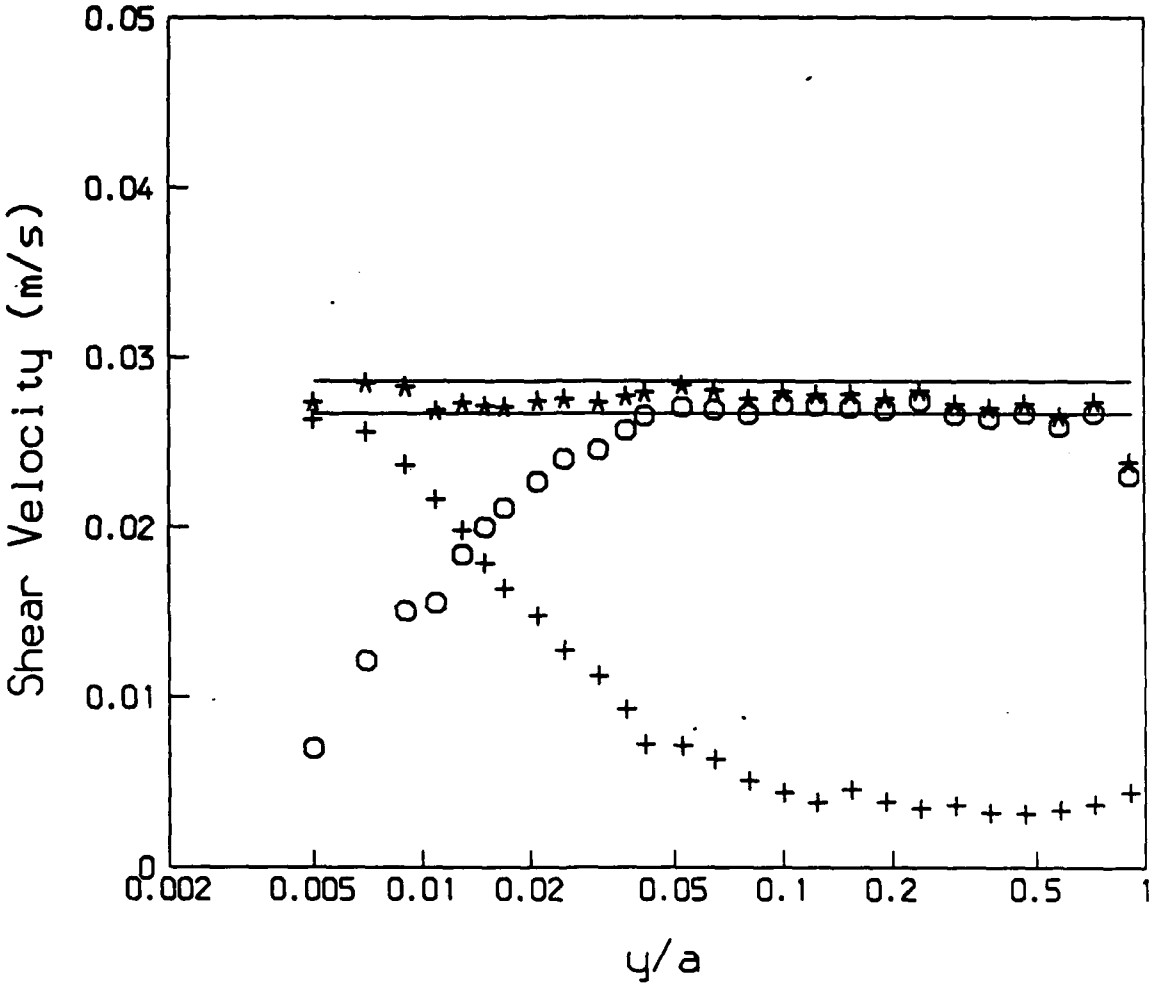

Figure 3.1 Estimated shear velocity for water flow with no injection: * , u_τ; + , viscous contribution; O , turbulent contribution; ═══ , 95% confidence interval.

3.2 Mean velocities

Figure 3.2 shows the mean streamwise velocity profile normalized with shear velocity and kinematic viscosity (this normalization is hereafter indicated by the + superscript). The two solid lines in the figure represent the near-wall variation in U^+,

$$U^+ = y^+. \tag{3.1}$$

and the relationship for the logarithmic overlap region

$$U^+ = \frac{1}{\kappa} \ln y^+ + B. \tag{3.2}$$

There is good agreement between the line and the data in the linear region and there is good correspondence with the logarithmic law using κ=0.41 and B=6.0 (Luchik and Tiederman, 1987).

3.3 Second moments

Figure 3.3 shows the root-mean-square (RMS) velocity fluctuation level for the streamwise and normal velocity components as a function of distance from the wall. These results show a peak in u' of 2.9 at about $y^+ = 15$ and a value of about one at the channel centerline. The RMS of the normal velocity shows a broad peak of about 1.2 centered near $y^+ = 100$ and drops to slightly less than one at the channel centerline. These values for u' and v' agree well with Kreplin and Eckelmann (1979) but are about ten percent higher than those reported by Wei (1987), Hussain and Reynolds (1978) and Kim et al. (1987).

The effect of gradient broadening on the measured u' levels due to the finite size of the measuring volume is estimated to introduce about six percent error at $y^+ = 5$ and

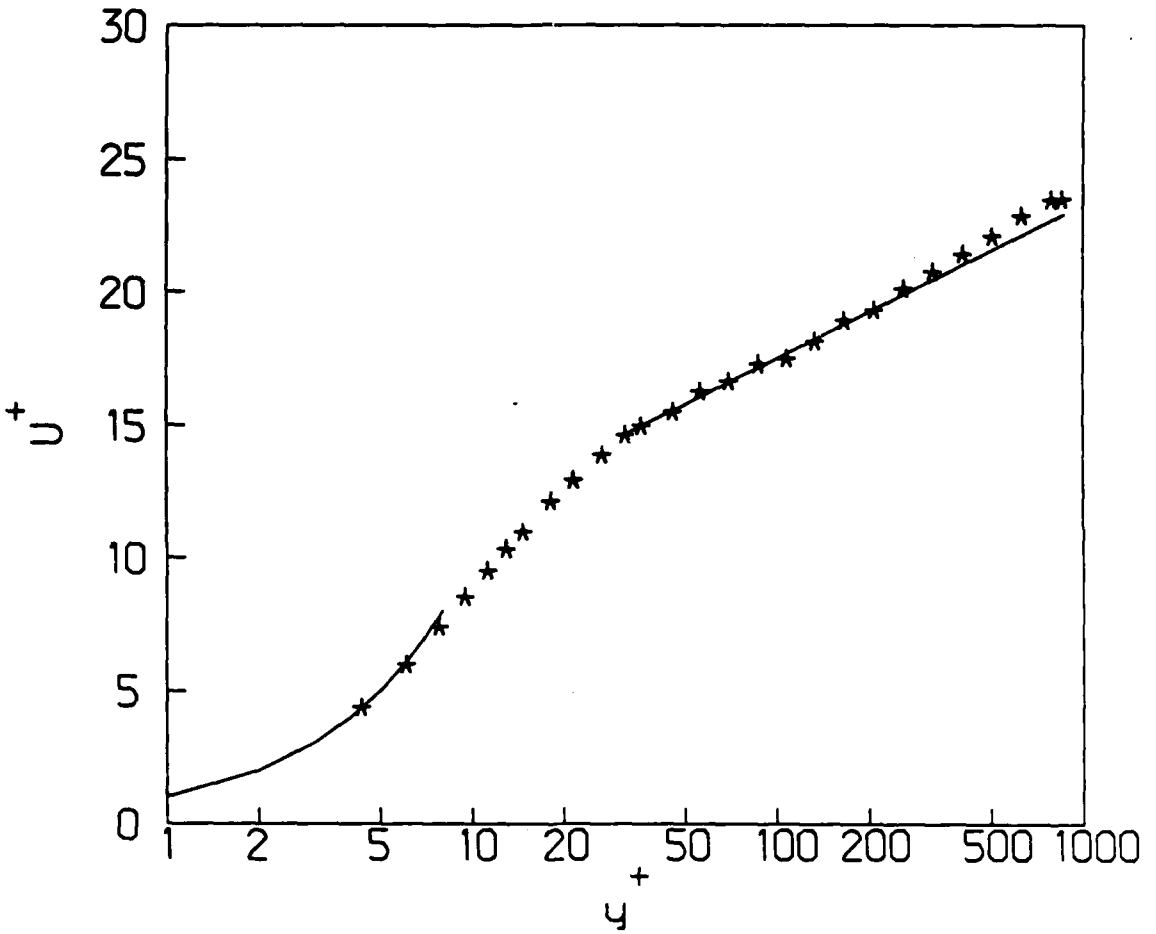

Figure 3.2 Mean velocity profile for water flow with no injection.

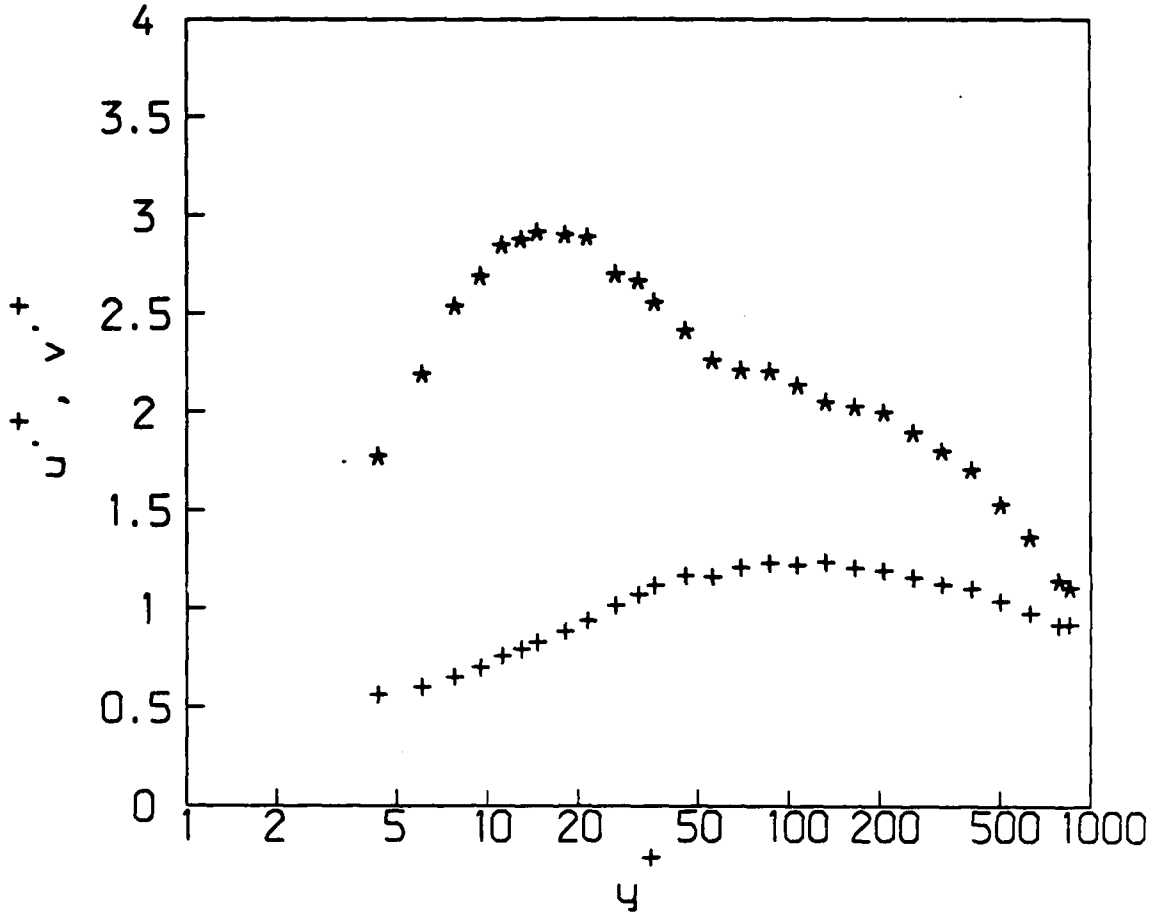

Figure 3.3 Root-mean-square velocity fluctuation profiles for water flow with no injection: * , u'/u_τ; + , v'/u_τ.

less than one percent error for $y^+ > 10$ (see Karpuk and Tiederman, 1976). The results of Luchik and Tiederman (1986) show that for laser velocimeter measurements the RMS levels are not affected by spatial averaging over the spanwise length of the probe as is the case with hot-wire and hot-film devices. Therefore, since the uncertainty in u_τ is small, these results are believed to accurately represent the turbulence structure.

The near-wall behavior of the RMS velocities is shown in Figure 3.4. The behavior of u' is as expected near the wall; the RMS of the normal velocity, however, approaches a constant value as y approches zero. The results of Finnicum and Hanratty (1985) and Kim et al. (1987) indicate that v' varies as y^2 at the wall. The present results do not appear to be consistent with this trend and therefore the accuracy of the v' measurements for $y^+ < 10$ is questionable.

The RMS velocities when normalized by the local mean velocity (turbulence intensity) are shown in Figure 3.5 and the near-wall variation is shown in Figure 3.6. Near the channel centerline, both quantities approach about 4 to 5 percent, as is expected. The streamwise turbulence intensity is approaching a value near 0.4 at the wall which is slightly higher than Kim et al. (1987) (0.36)and considerably higher than Hanratty et al. (1977) (0.3). The normal turbulence intensity behaves as expected, except for $y^+ < 10$.

For a fully developed channel flow, the total shear stress (mean viscous shear stress minus Reynolds shear stress) varies linearly across the channel

$$\tau_{total} = \mu\frac{d\overline{U}}{dy} - \rho\overline{uv} = \tau_{wall}(1 - y/a) \qquad (3.3)$$

The turbulent shear stress $\overline{uv}$ is shown in Figure 3.7 normalized with u_τ; also shown is a

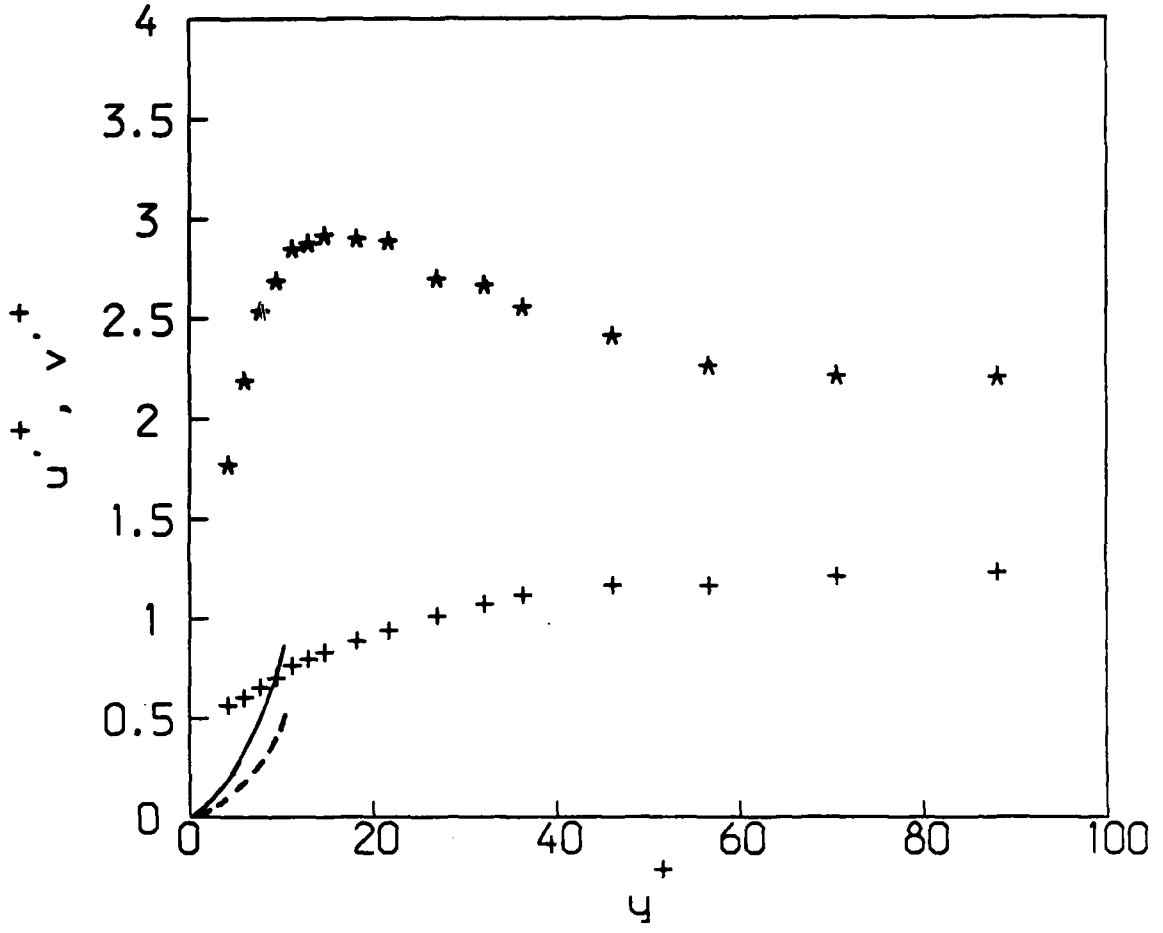

Figure 3.4 Near-wall behavior of root-mean-square velocity fluctuations: * , u'/u_τ; + , v'/u_τ; – – – – , $v'/u_\tau = 0.005y^{+2}$ (Finnicum and Hanratty, 1985); ———— , $v'/u_\tau = 0.009y^{+2}$ (Kim et al.,1987).

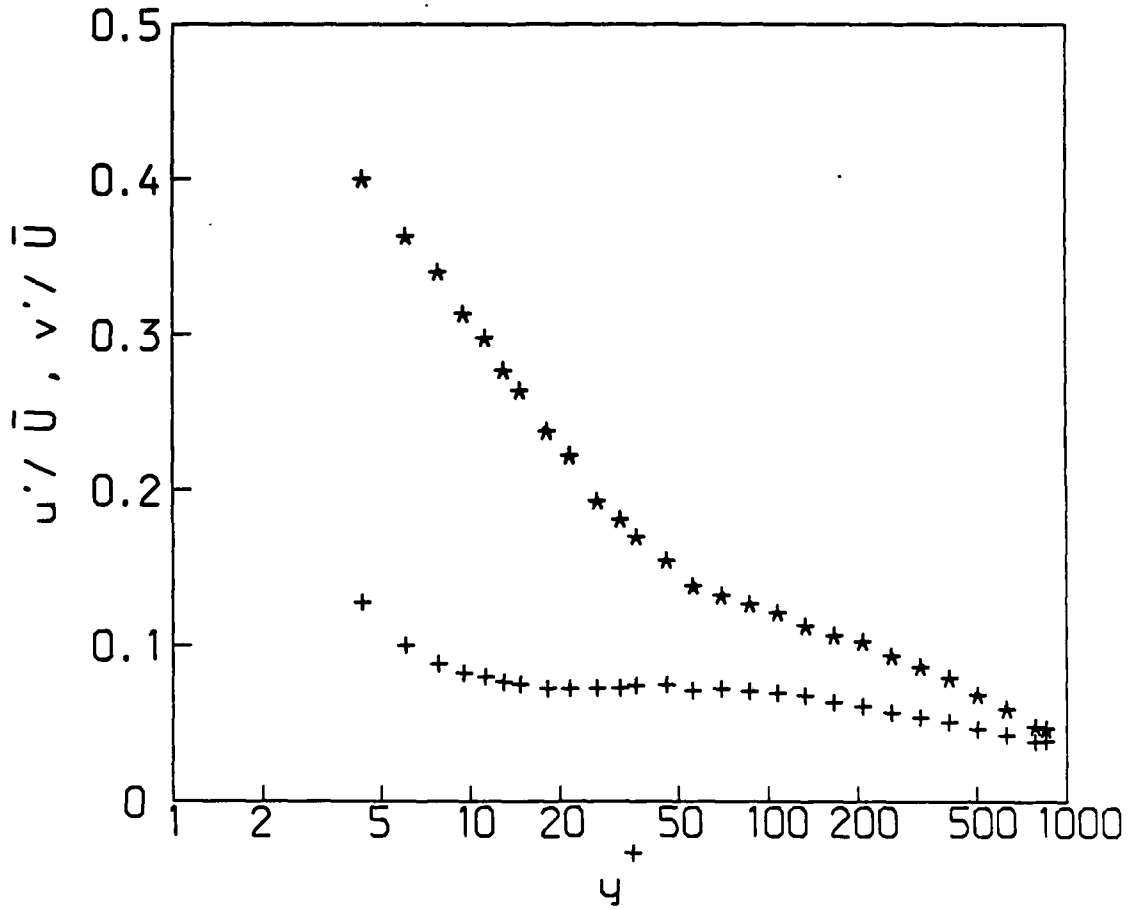

Figure 3.5 Turbulence intensity profiles for water flow with no injection: * , $u'/\bar{U}$; + , $v'/\bar{U}$.

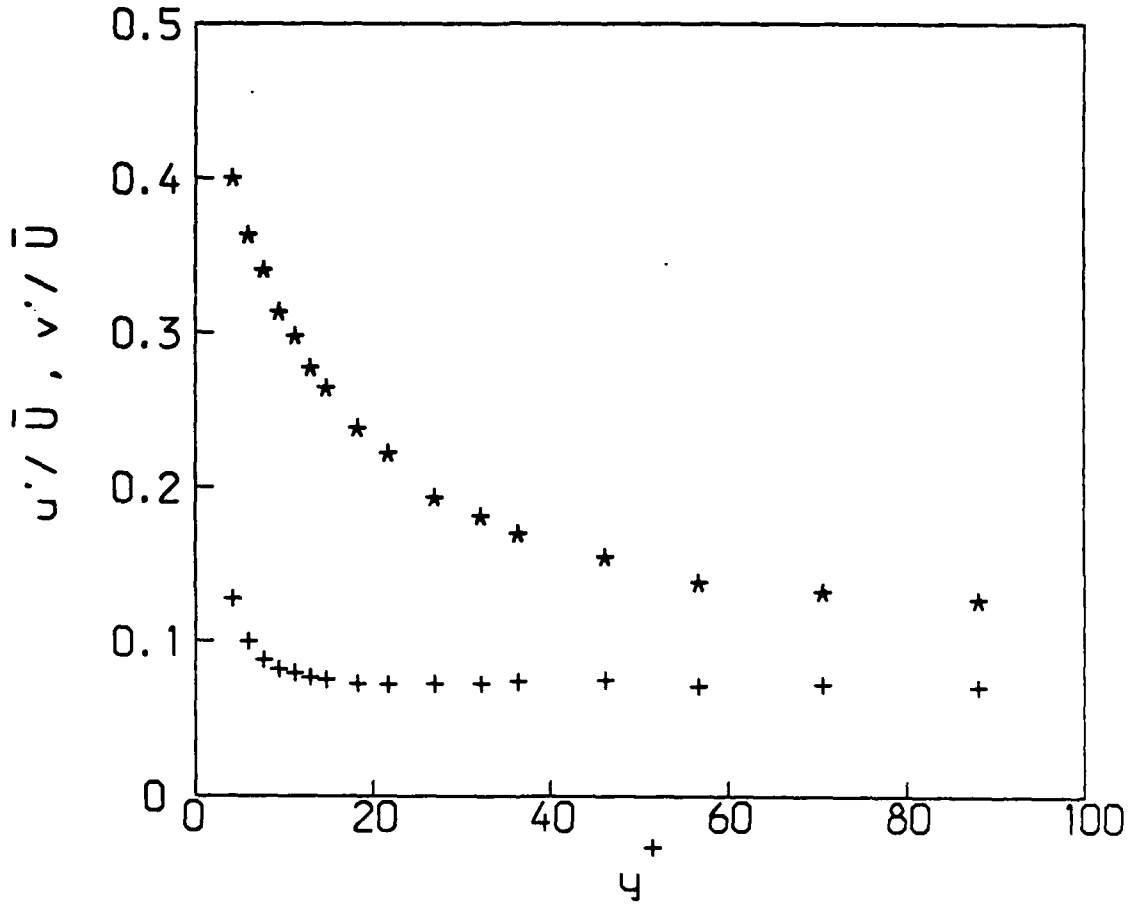

Figure 3.6 Near-wall behavior of turbulence intensity: * , $u'/\bar{U}$; + , $v'/\bar{U}$.

line representing the linear variation in total shear across the channel. Away from the wall, where the mean viscous shear is small, the agreement between the line and the data is excellent. Equation 3.3 can be solved for $-\rho\overline{uv}$

$$-\rho\overline{uv} = \tau_{wall}(1 - y/a) - \mu\frac{d\overline{U}}{dy}. \qquad (3.4)$$

Figure 3.8 shows the same data on a semi-log coordinates, which allows a more detailed examination of the near-wall region, along with a line representing Equation 3.4 (the values determined from subtracting the the mean viscous shear stress from the total shear stress). There is good agreement between these two values, although there is some scatter in the data near the peak in $-\overline{uv}$.

The correlation coefficient R_{uv} is a measure of how strongly the u and v fluctuations are correlated, i.e. the degree to which the velocity fluctuations contribute to momentum transport. If u = kv where k is a constant, the data is perfectly correlated and every velocity fluctuation contributes to the net momentum transport (R_{uv} = 1); if the fluctuations in u and v are independent, R_{uv} is zero. The peak value of R_{uv}, shown in Figure 3.9 as a function of y^+, is about 0.35 which is lower than that seen in the numerical work of Moin and Kim (1982) (~0.4 at Re = 24 300) and Kim et al. (1987) (0.45-0.50 at Re = 5600). The results of Wei (1987) decrease from 0.45 to 0.35 as Reynolds number increases from 30 000 to 80 000. Assuming the trend toward lower peak values with increasing Reynolds number is correct, the present results are compatible with the numerical results although they disagree with those of Wei. The occurrence of a local peak in R_{uv} near y^+ = 12 which has been seen in all the published channel flow computations (Moin and Kim, 1982; Kim et al., 1987; Moser and Moin,

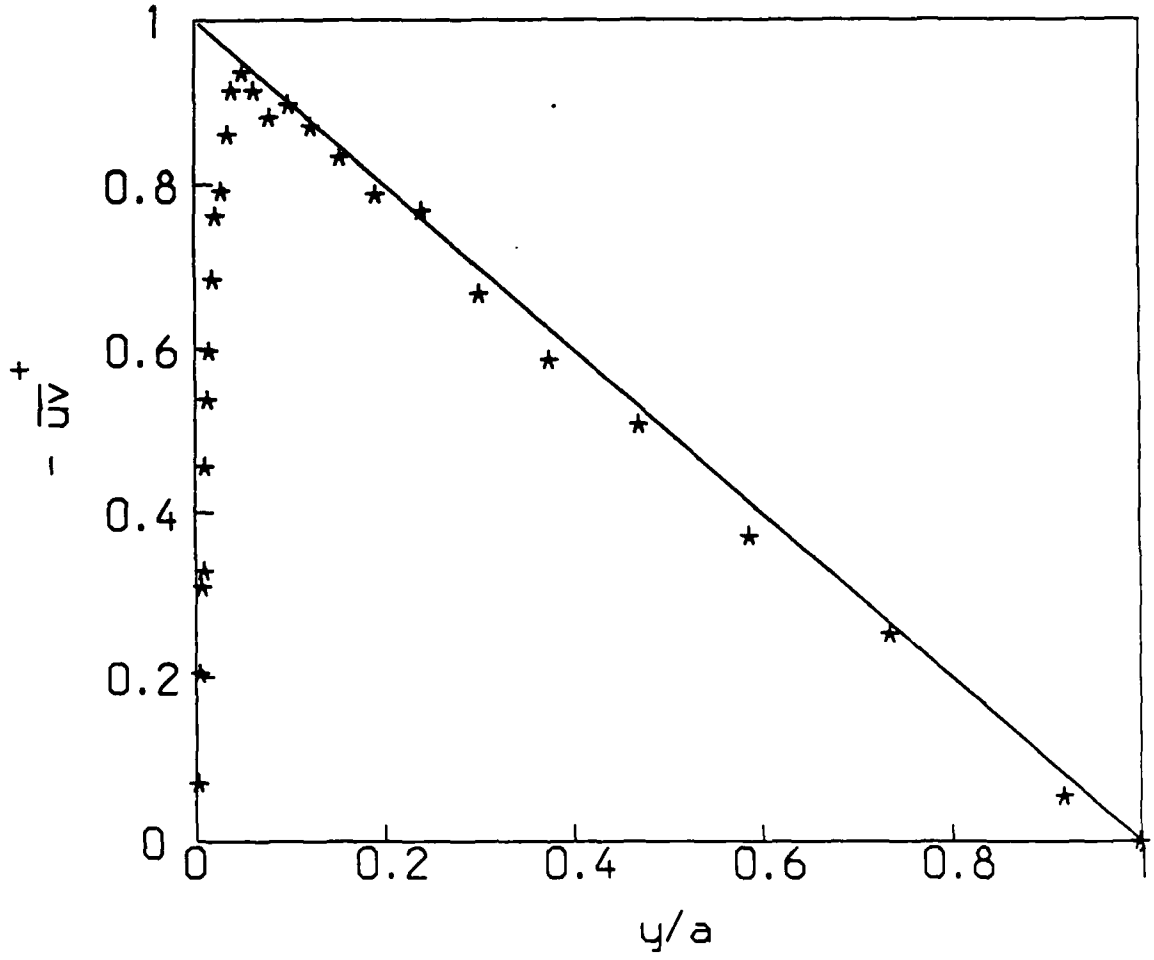

Figure 3.7 Turbulent shear stress for water flow with no injection; ——— , total shear stress for fully developed flow (Equation 3.3).

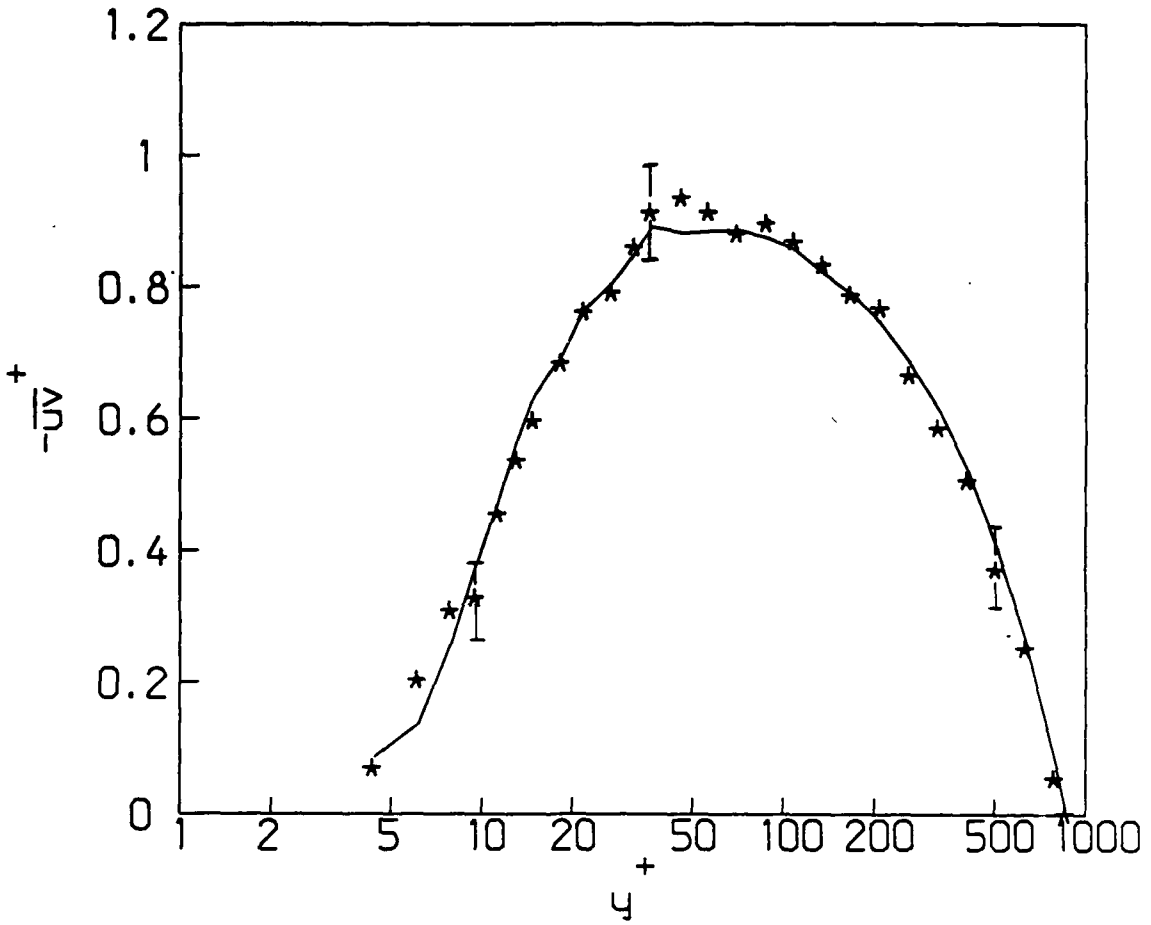

Figure 3.8 Turbulent shear stress for water flow with no injection; ———— , Equation 3.4; I , 95 % confidence interval.

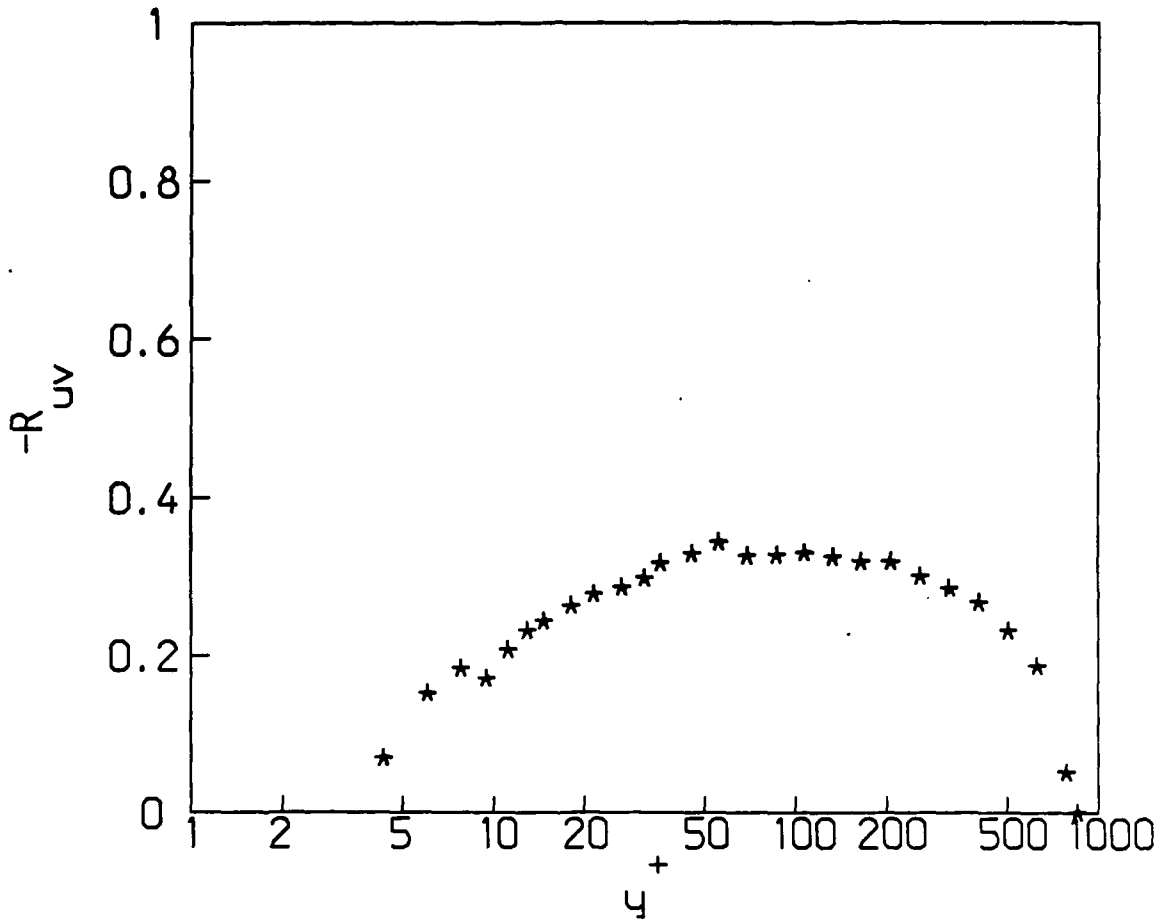

Figure 3.9 Correlation coefficient for water flow with no injection.

1987) does not appear in the present experimental results.

3.4 Reynolds stress production

One can derive transport equations for the elements of the Reynolds stress tensor $\overline{u_i u_j}$. Although these are not "conservation" equations in the strict thermodynamic sense, the terms of the equations represent contributions to the maintenance of a $\overline{u_i u_j}$ in a unit control volume. The general form of these equations (see e.g. Bradshaw, 1978) is shown in Equation 3.5.

$$\begin{aligned}\frac{\partial \overline{u_i u_j}}{\partial t} + \overline{U}_l \frac{\partial \overline{u_i u_j}}{\partial x_l} = &\underbrace{-\left[\overline{u_i u_l}\frac{\partial \overline{U}_j}{\partial x_l} + \overline{u_j u_l}\frac{\partial \overline{U}_i}{\partial x_l}\right]}_{\text{I}} \\ &\underbrace{+\overline{\frac{p'}{\rho}\left[\frac{\partial u_i}{\partial x_j} + \frac{\partial u_j}{\partial x_i}\right]}}_{\text{II}} \\ &\underbrace{-\frac{\partial}{\partial x_l}\overline{(u_i u_j u_l)}}_{\text{III}} \underbrace{-\frac{1}{\rho}\left[\frac{\partial}{\partial x_i}\overline{(p' u_j)} + \frac{\partial}{\partial x_j}\overline{(p' u_i)}\right]}_{\text{IV}} \\ &\underbrace{+\nu\frac{\partial^2 \overline{u_i u_j}}{\partial x_l{}^2}}_{\text{V}} \underbrace{-2\nu\overline{\left[\frac{\partial u_i}{\partial x_l}\frac{\partial u_j}{\partial x_l}\right]}}_{\text{VI}}\end{aligned} \tag{3.5}$$

Choosing different values of i and j yields equations for the six independent Reynolds stresses. The left-hand side of this equation represents the time rate of change and advection of a given Reynolds stress. These are balanced by the terms on the right-hand side: Term I represents production of Reynolds stress by interaction of the turbulent motion with the mean rate-of-strain field. Term II accounts for the generation, destruction or redistribution between components by means of pressure

fluctuations and is generally referred to as the pressure-strain correlation. The pressure-strain correlation causes the normal stresses to become more isotropic; the small magnitude stresses are increased at the expense of the larger stresses. Terms III and IV represent transport through turbulent fluctuations: III accounting for transport by velocity fluctuations and IV for pressure fluctuations. Viscous transport of Reynolds stress is represented by term V and term VI represents generation or destruction due to viscous stress fluctuations.

The behavior of the terms in Equation 3.5 is presented in detail by Mansour et al. (1988) and Spalart (1988) for a fully developed channel flow and a boundary layer, respectively. These results were obtained by direct numerical simulation of turbulent flow.

Equation 3.5 can be specialized to the case of stationary, fully-developed, two-dimensional (on average) flow. For this case, the left-hand side of the equation is zero and the right-hand side is simplified. For the streamwise normal-stress $\overline{u^2}$ the result is Equation 3.6.

$$\begin{aligned} 0 = & \underset{\text{I}}{-2\,\overline{uv}\frac{\partial \overline{U}}{\partial y}} + \underset{\text{II}}{2\,\overline{\frac{p'}{\rho}\left[\frac{\partial u}{\partial x}\right]}} \underset{\text{III}}{- \frac{\partial}{\partial y}\overline{(u^2 v)}} \\ & \underset{\text{V}}{+ \nu\frac{\partial^2 \overline{u^2}}{\partial y^2}} \underset{\text{VI}}{- 2\nu\left[\overline{\left[\frac{\partial u}{\partial x}\right]^2} + \overline{\left[\frac{\partial u}{\partial y}\right]^2} + \overline{\left[\frac{\partial u}{\partial z}\right]^2}\right]} \end{aligned} \tag{3.6}$$

The dominant source term is the production term (I) and it is balanced primarily by destruction due to viscous stress fluctuations (VI) and redistribution to the other normal

stresses through the pressure-strain correlation (II). Equation 3.7 shows the resulting equation for the wall-normal normal-stress $\overline{v^2}$.

$$\begin{aligned} 0 = \; & \underset{II}{2\overline{\frac{p'}{\rho}\left[\frac{\partial v}{\partial y}\right]}} - \underset{III}{\frac{\partial(\overline{v^3})}{\partial y}} - \underset{IV}{\frac{2}{\rho}\frac{\partial}{\partial y}(\overline{p'v})} \\ & + \underset{V}{\nu\frac{\partial^2\overline{v^2}}{\partial y^2}} - \underset{VI}{2\nu\left[\overline{\left[\frac{\partial v}{\partial x}\right]^2} + \overline{\left[\frac{\partial v}{\partial y}\right]^2} + \overline{\left[\frac{\partial v}{\partial z}\right]^2}\right]} \end{aligned} \tag{3.7}$$

For this component of the Reynolds stress tensor, there is no type I production term. The major source term is the pressure-strain correlation (II) which increases $\overline{v^2}$ and decreases $\overline{u^2}$. This source is balanced by the viscous destruction term (VI). Equation 3.8 is for the Reynolds shear stress $\overline{uv}$.

$$\begin{aligned} 0 = \; & \underset{I}{-\overline{v^2}\frac{\partial \overline{U}}{\partial y}} + \underset{II}{\overline{\frac{p'}{\rho}\left[\frac{\partial u}{\partial y} + \frac{\partial v}{\partial x}\right]}} - \underset{III}{\frac{\partial}{\partial y}(\overline{uv^2})} \\ & \underset{IV}{-\frac{1}{\rho}\left[\frac{\partial}{\partial x}(\overline{p'v}) + \frac{\partial}{\partial y}(\overline{p'u})\right]} + \underset{V}{\nu\frac{\partial^2\overline{uv}}{\partial y^2}} \\ & \underset{VI}{-2\nu\left[\overline{\left[\frac{\partial u}{\partial x}\frac{\partial v}{\partial x}\right]} + \overline{\left[\frac{\partial u}{\partial y}\frac{\partial v}{\partial y}\right]} + \overline{\left[\frac{\partial u}{\partial z}\frac{\partial v}{\partial z}\right]}\right]} \end{aligned} \tag{3.8}$$

As in Equation 3.6, the dominant production term is term I. The results of Spalart (1988) and Mansour et al. (1988) show that in the shear stress equation, the pressure-strain correlation (II) is primarily responsible for the destruction of shear stress and that destruction through viscous stress fluctuations (term VI) is very small. For all

components of the Reynolds stress tensor, the contributions from turbulent diffusion (terms III and IV) and viscous diffusion (term V) are generally small. The equation for $\overline{w^2}$ is similar to Equation 3.7 and the other two shear stresses, $\overline{uw}$ and $\overline{vw}$ are identically zero.

Examination of Equations 3.6 and 3.8 shows that there are two quantities responsible for the production of Reynolds stress in this flow. In the transport equation for the streamwise normal stress $\overline{u^2}$ (Equation 3.6), the production term has the form

$$\overline{uv}\frac{d\overline{U}}{dy}. \tag{3.9}$$

For the Reynolds shear stress $\overline{uv}$, the production term (from Equation 3.8) is

$$\overline{v^2}\frac{d\overline{U}}{dy}. \tag{3.10}$$

Figure 3.10 shows the $\overline{u^2}$ production profile for this flow normalized with shear velocity and kinematic viscosity. Also shown is a line representing this quantity calculated using the value of $\overline{uv}$ from Equation 3.4. The agreement between the two results is excellent and they compare favorably with results presented in the literature. Reynolds shear stress ($\overline{uv}$) production is shown in Figure 3.11. This quantity exhibits a peak near $y^+ = 10$ which is significantly higher than that reported by Spalart (1988), Mansour et al. (1988) and Nagano and Hishida (1985). Those studies both showed a peak of about 0.1-0.15 at $y^+ = 15$–20. For $y^+ > 10$ the behavior is reasonable and the difference nearer the wall is attributable to the error in the measured v'.

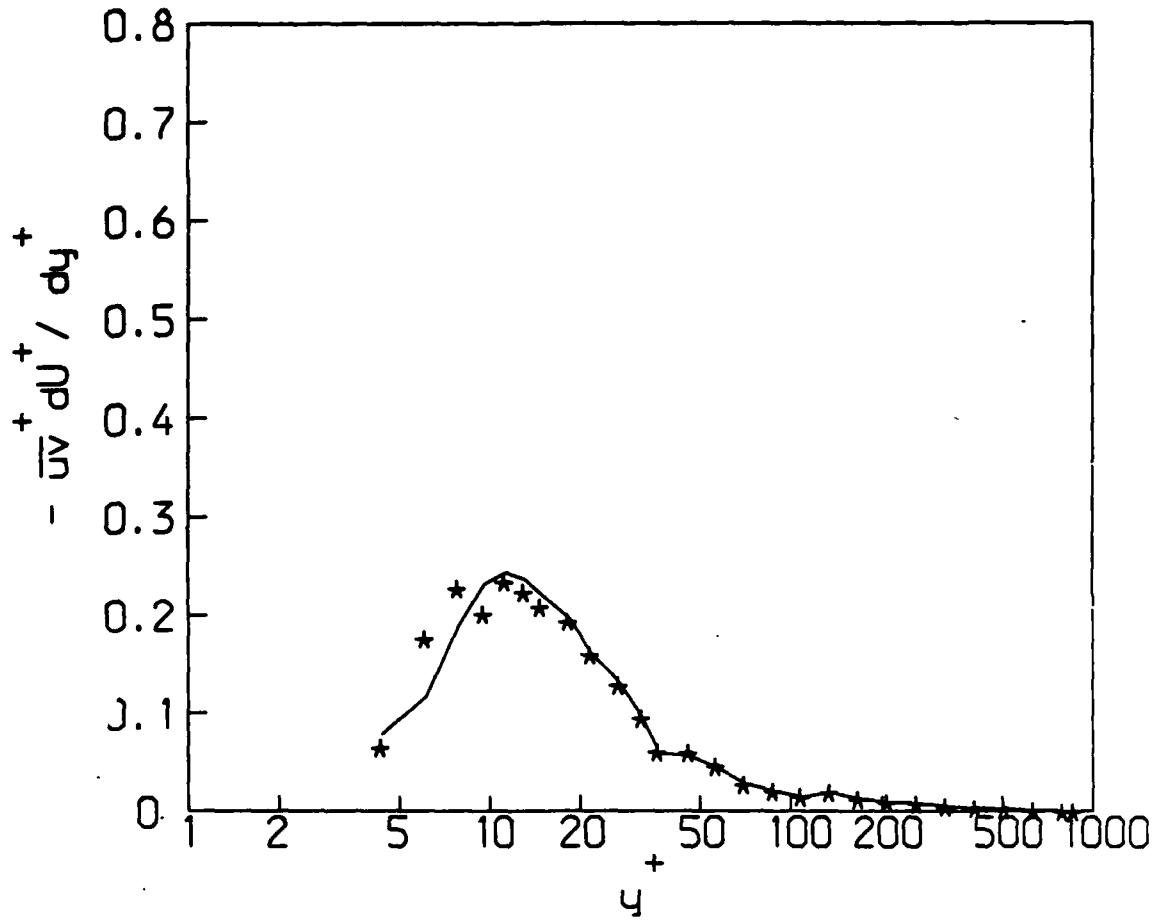

Figure 3.10 Reynolds stress production ($\overline{u^2}$ component) for water flow with no injection; ———— , production calculated using $\overline{uv}$ from Equation 3.4.

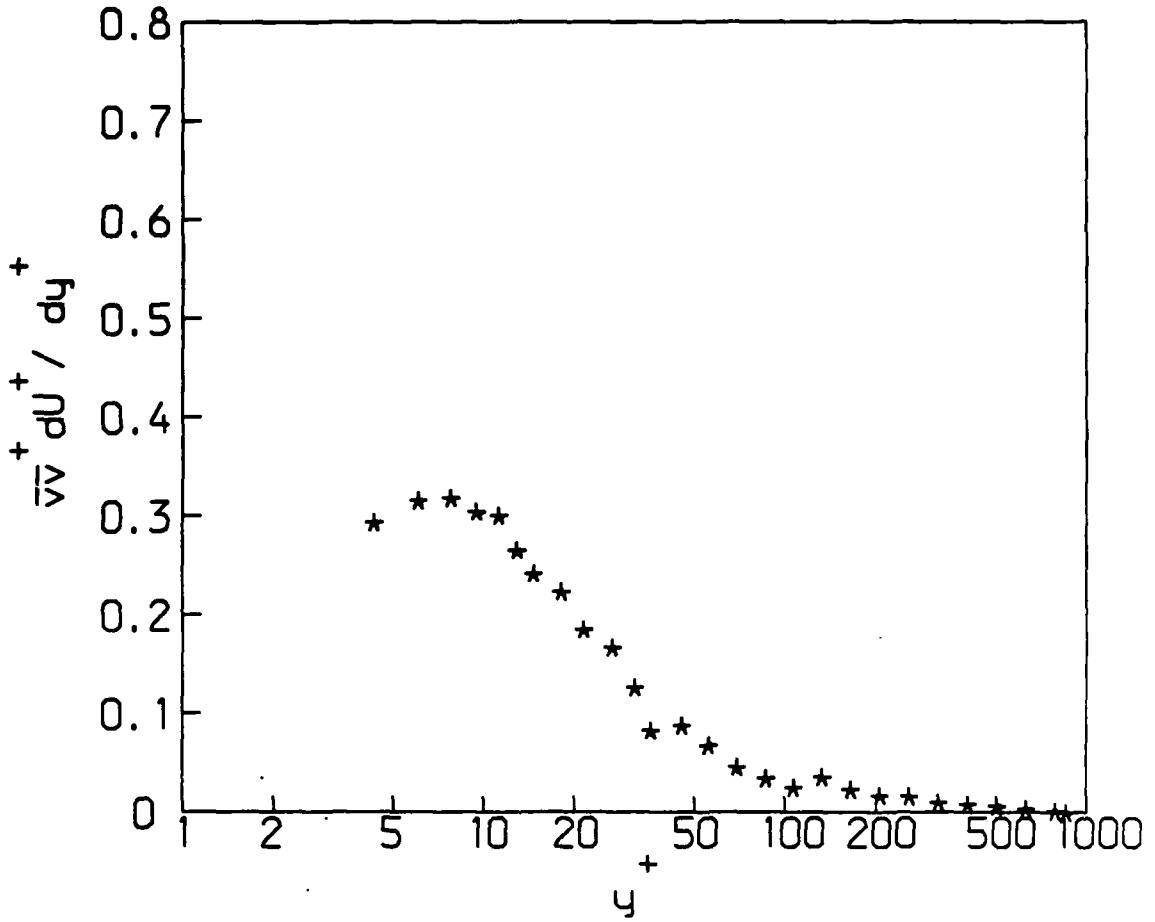

Figure 3.11 Reynolds stress production ($\overline{uv}$ component) for water flow with no injection.

CHAPTER 4 - THE CONCENTRATION FIELD IN INJECTED FLOWS

Concentration measurements were made while injecting either pure water or a 700 ppm aqueous solution of SEPARAN AP-273. The flow in the channel was maintained at the conditions described in the previous section for the flow with no injection. The fluids were injected at both the top and bottom channel walls at a flow rate equal to the mass flow rate through the linear portion of the viscous sublayer of the undisturbed channel flow (1.0 ℓ/min through each injection slot). For the polymer solution, this resulted in 25 percent drag reduction in the region from 50 to 150 mm downstream of the injector and a peak drag reduction level of 44 percent in the region from 150 to 250 mm based on the measured change in the static pressure drop.

For the flow with water injection, concentration measurements were made at locations 10, 25, 50, and 100 mm downstream of the injector. The first one hundred elements of the photodiode array were sampled resulting in concentration profiles which covered 6 mm of the flow starting at the lower channel wall. For polymer injection, concentration measurements were made at locations 10, 25, 50, 100 and 200 mm downstream of the injector ($x^+ = 290$, 730, 1450, 2910 and 5810 respectively). The first one hundred elements of the photodiode array were sampled and the measurements were made over 7 mm adjacent to the channel wall.

4.1 Time-resolved concentration profiles

In order to examine the type of instantaneous behavior in the concentration field which gives rise to the time averaged statistics, time-resolved measurements of injectant concentration profiles are presented in Figures 4.1 through 4.6. Concentrations are normalized with the injected concentration and the distance from the wall is normalized with the shear velocity and kinematic viscosity of the water flow with no injection. These data were taken at x = 25 mm for the flow with dyed water injection and for all five measurement stations in the flow with polymer injection. Figures 4.1 through 4.4 are representative of the entire time records from which they were taken. At the two downstream measurement stations there were short periods of activity interspersed with considerably longer intervals which were relatively quiescent. (Here, activity is defined as movement of high concentration fluid away from the wall.) Figures 4.5 and 4.6 were taken from active periods and are not representative of the entire time sequence from which they were taken.

For the flow with water injection, Figure 4.1, there are periods of activity and quiescent periods interspersed in time and relatively high concentrations extending instantaneously to $y^+ = 150$ and beyond. In Figure 4.2 time-resolved concentration profiles at x = 10 mm for polymer injection are shown. The concentration at the wall is consistently high, but in the region from y^+ of 25 to 100 the concentration varies between one and zero. This indicates that the initial mixing of the polymer solution occurs through stretching and distortion of the injected polymer layer, rather than through diffusive transport. The regions of high concentration fluid extending from the

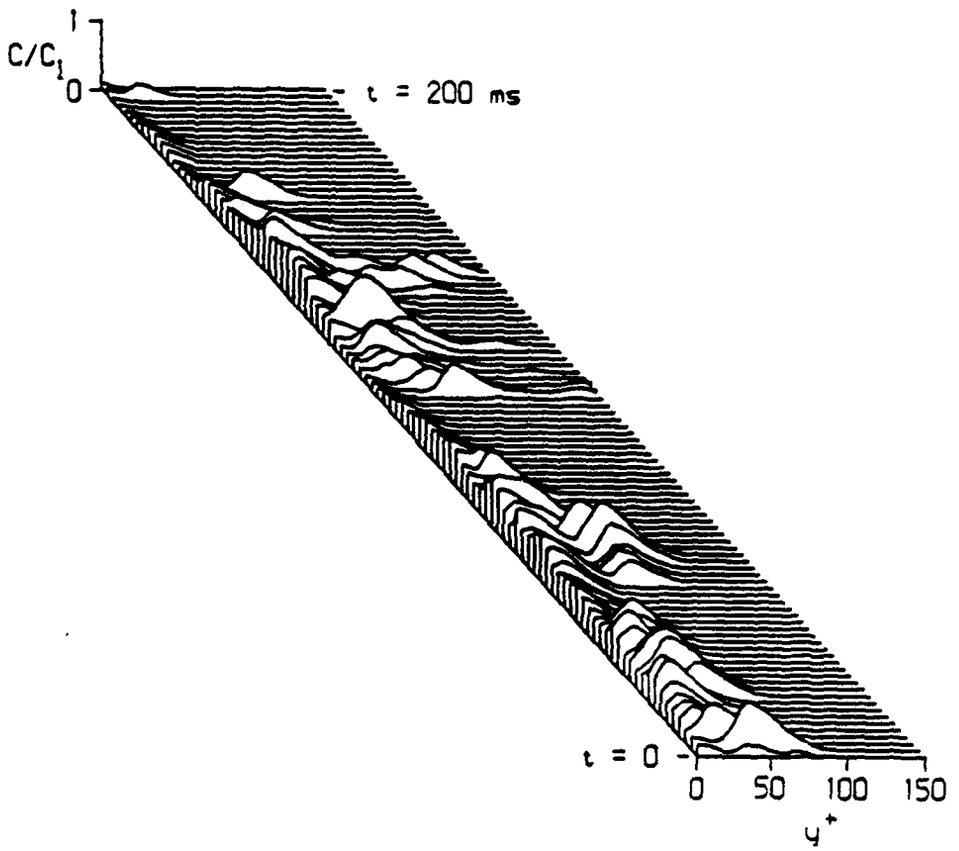

Figure 4.1 Time-resolved concentration profiles at x=25 mm for water injection.

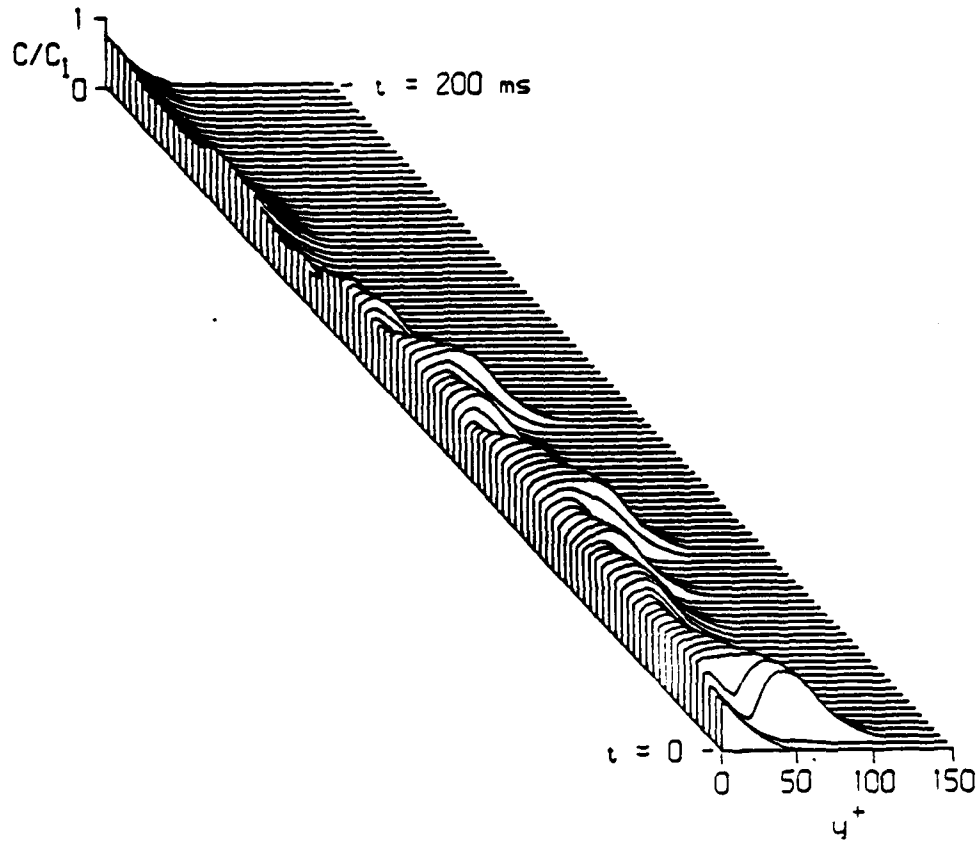

Figure 4.2 Time-resolved concentration profiles at x=10 mm for polymer injection.

wall appear to persist for the same duration as the periods of activity in the water flow. This may mean that the timescales associated with the initial mixing of the polymer solution with the flow are similar to those of the event responsible for transport in the flow without polymer injection.

At x = 25 mm and 50 mm (Figures 4.3 and 4.4) the concentrations are reduced and the flow is relatively quiescent with very little movement of the high concentration fluid outward from the wall. One would expect very little change in the long time average statistics in this region and also very small values of $\overline{vc}$.

The last two stations exhibit considerably more high concentration fluid moving away from the wall. The spatial behavior of the concentration field can be inferred from its temporal behavior by assuming the concentration field is "frozen" and moves past the probe at a fixed convection velocity (i.e. the Taylor hypothesis). The trajectory, in time, of the high concentration regions indicates that high concentration fluid lifts away from the wall in filaments which rise near their downstream end and remain near the wall at their upstream end. At the last location (Figure 4.5) the concentration levels are generally lower than at x = 100 mm (Figure 4.6) and there is slightly more activity.

4.2 Probability density functions for concentration

Plots of the probability density of measured polymer concentration as a function of normalized concentration and distance from the wall for the various streamwise locations are shown in Figures 4.7 through 4.11. The plots span the region from the

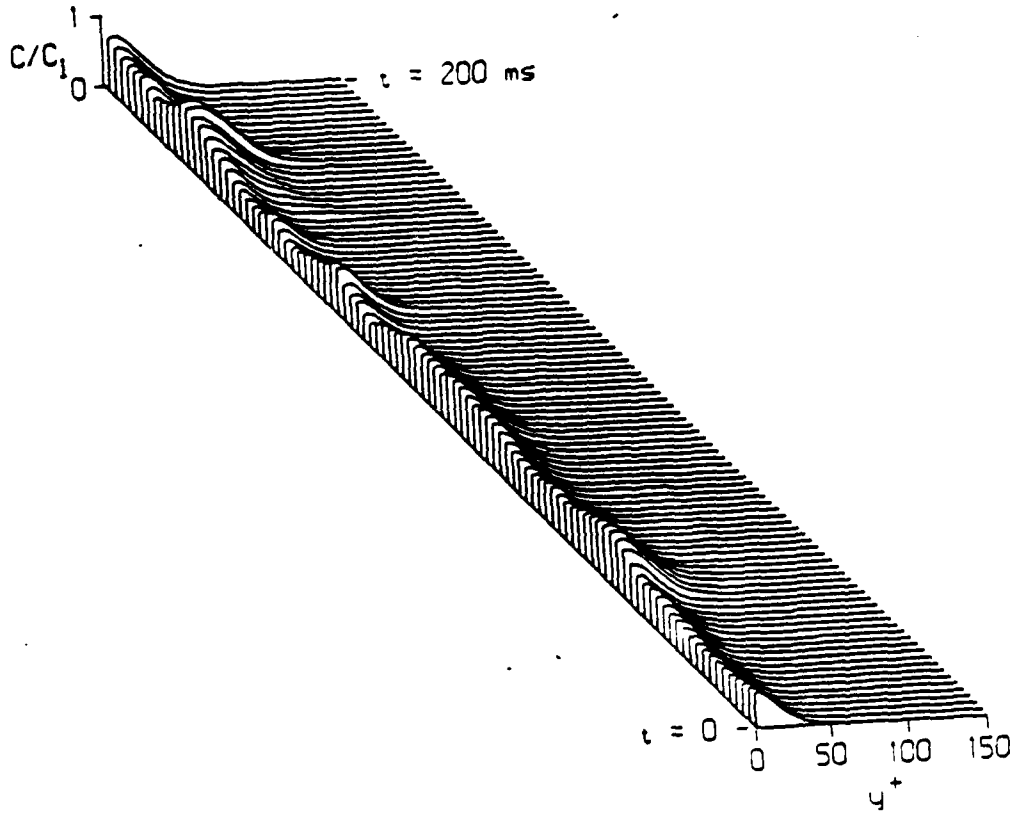

Figure 4.3 Time-resolved concentration profiles at x=25 mm for polymer injection.

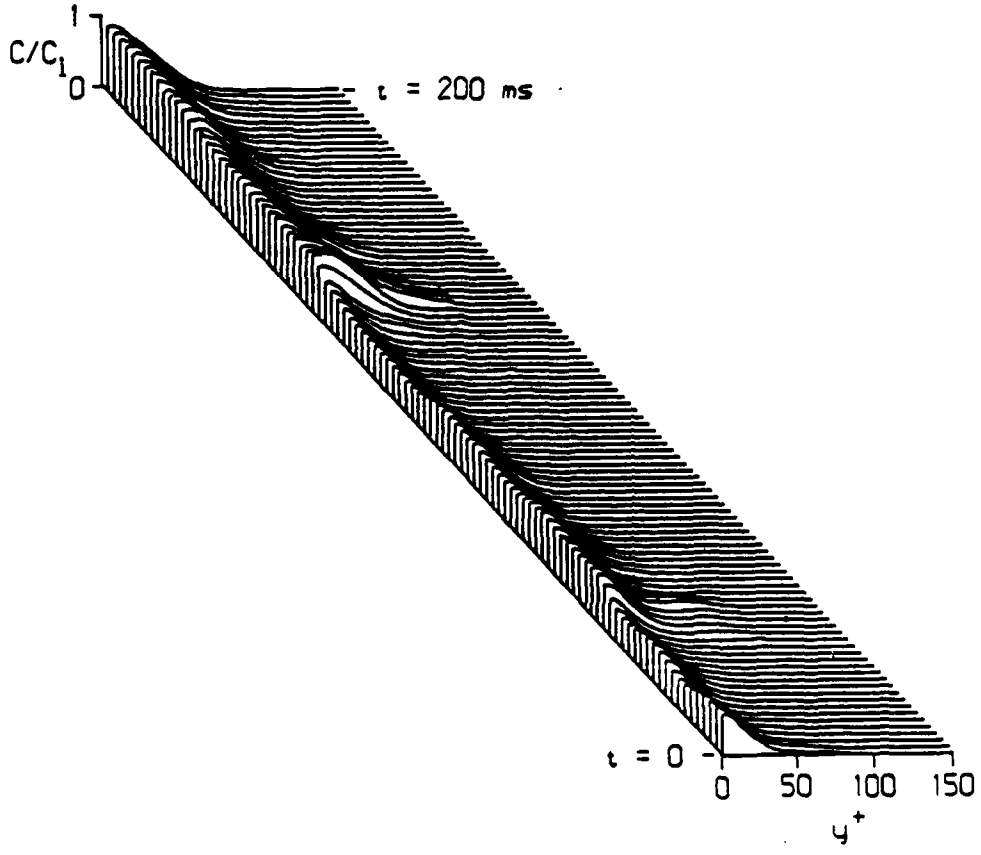

Figure 4.4 Time-resolved concentration profiles at x=50 mm for polymer injection.

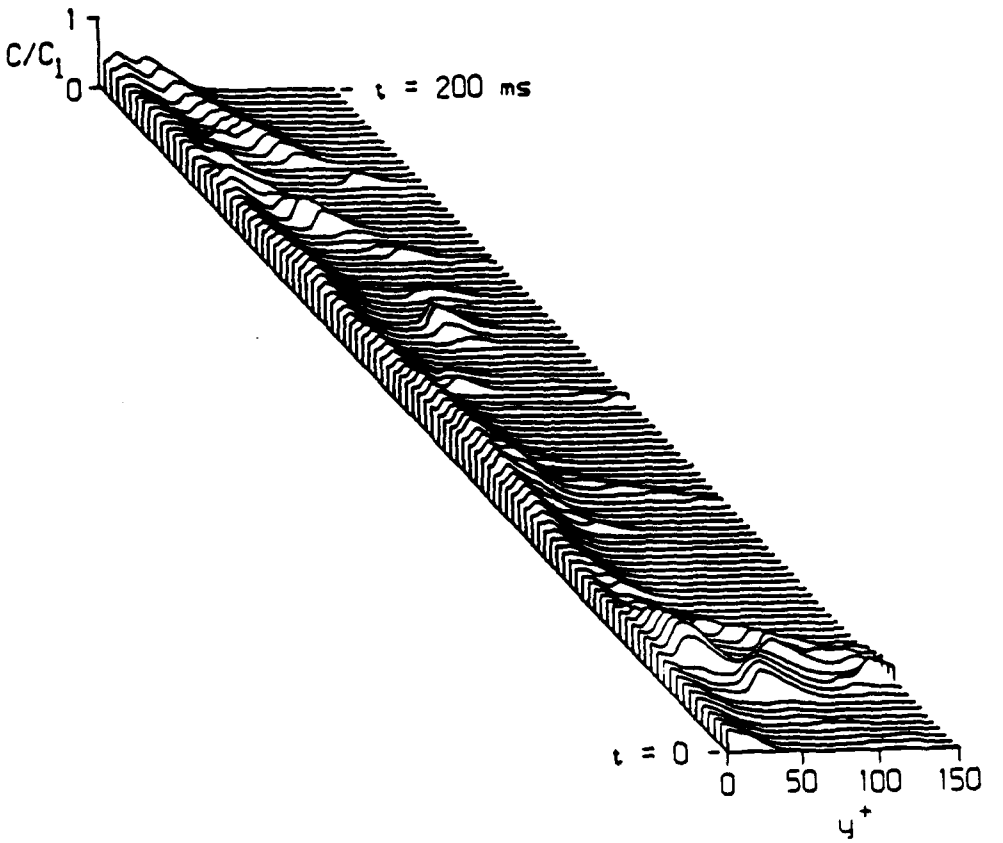

Figure 4.5 Time-resolved concentration profiles at x=100 mm for polymer injection.

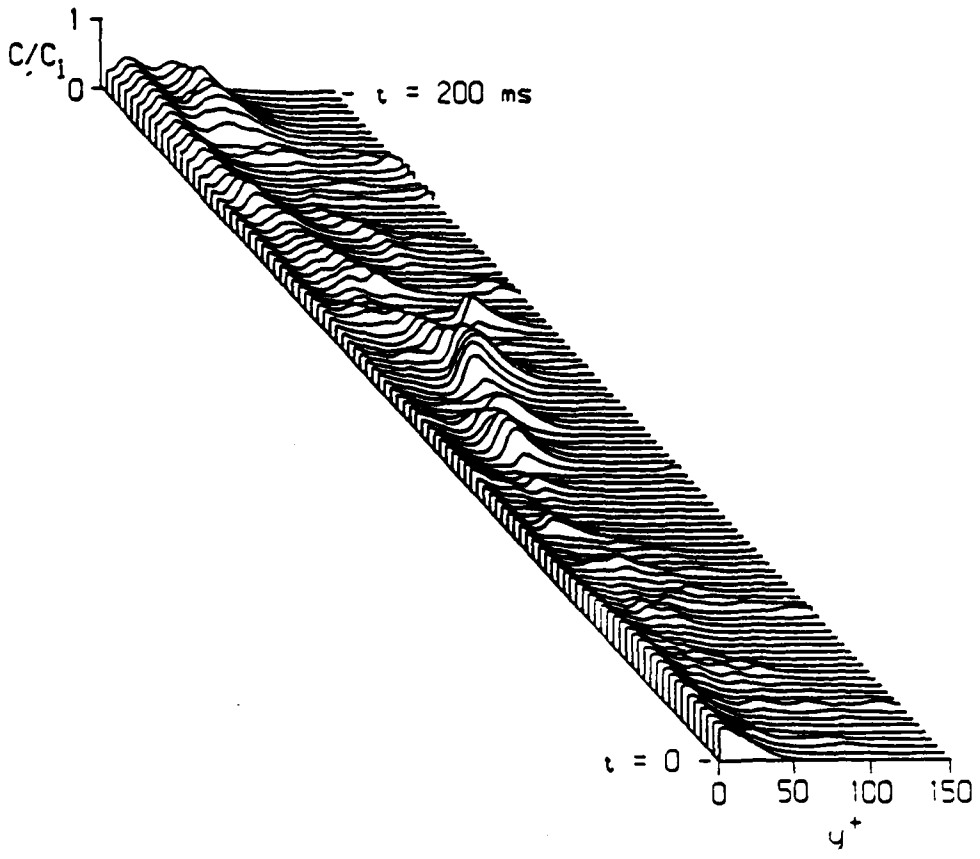

Figure 4.6 Time-resolved concentration profiles at x=200 mm for polymer injection.

wall to where there is minimal probability of non-zero concentration. One apparent anomaly is present in Figure 4.7, the plot for x = 10 mm: immediately adjacent to the wall ($y \leq 0.25$ mm, $y^+ \leq 7.3$) the probability of occurrence of concentrations near the injected concentration ($C/C_i=1$) is reduced compared to larger y-locations. It is believed that this is due to the slight difference in index of refraction between the water and polymer solution and the high polymer concentration present at the wall. This apparent inaccuracy in the measured concentration near the wall would introduce less than two percent error in the concentration values determined for locations farther from the wall. This effect was not apparent at any of the other streamwise locations.

At x = 10 mm (Figure 4.7), the concentration at the wall varies from about 0.35 up to 1.0. At about $y^+=25$, the presence of pure water is detected and at this location all concentrations between zero and 1.0 were measured. This behavior will result in large RMS concentration levels at this location. The measured concentrations steadily decrease with distance from the wall until virtually no polymer is present at about $y^+ = 80$. At x = 25 mm, shown in Figure 4.8, the distribution of concentrations near the wall has broadened to include concentrations less than 0.2. Pure water is still not detected for $y^+ < 25$ and the distributions at all y-locations except those immediately adjacent to the wall are becoming narrower and shifting toward lower concentrations. The probability density function at x = 50 mm, shown in Figure 4.9, is virtually unchanged from that at x = 25 mm and is further evidence that little transport away from the wall has occurred over this distance.

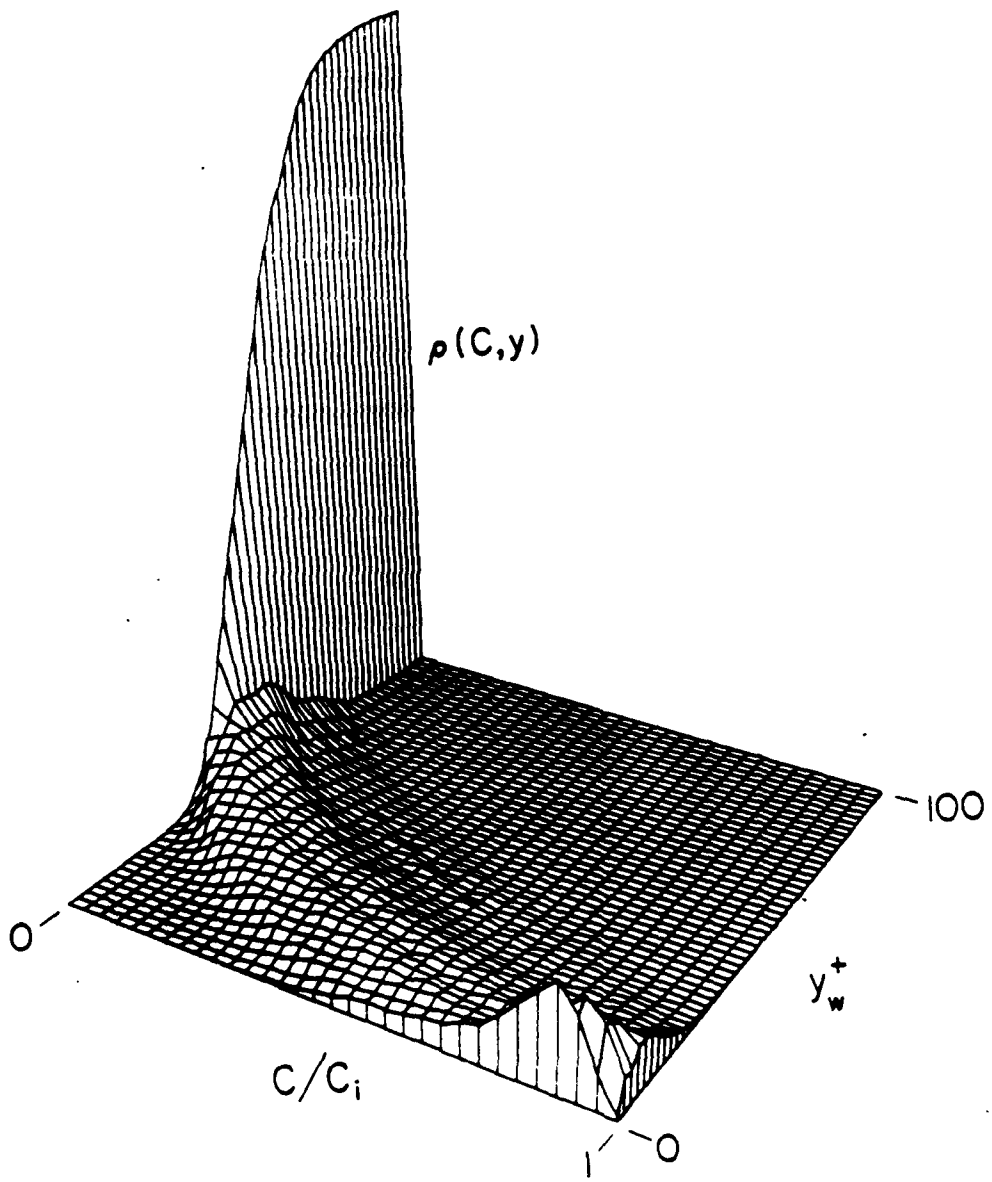

Figure 4.7 Probability density function for polymer concentration versus distance from the wall and concentration for x=10 mm

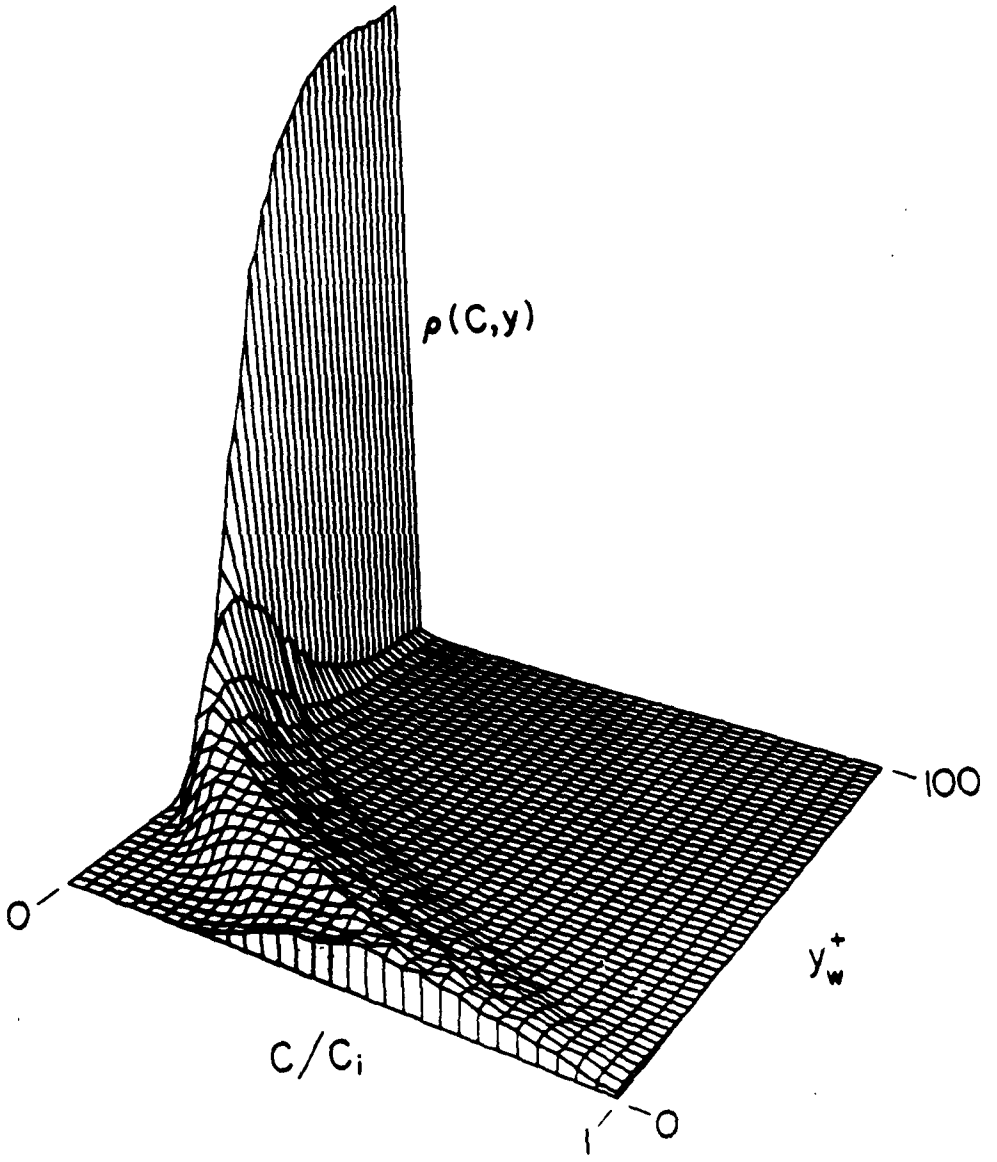

Figure 4.8 Probability density function for polymer concentration versus distance from the wall and concentration for x=25 mm

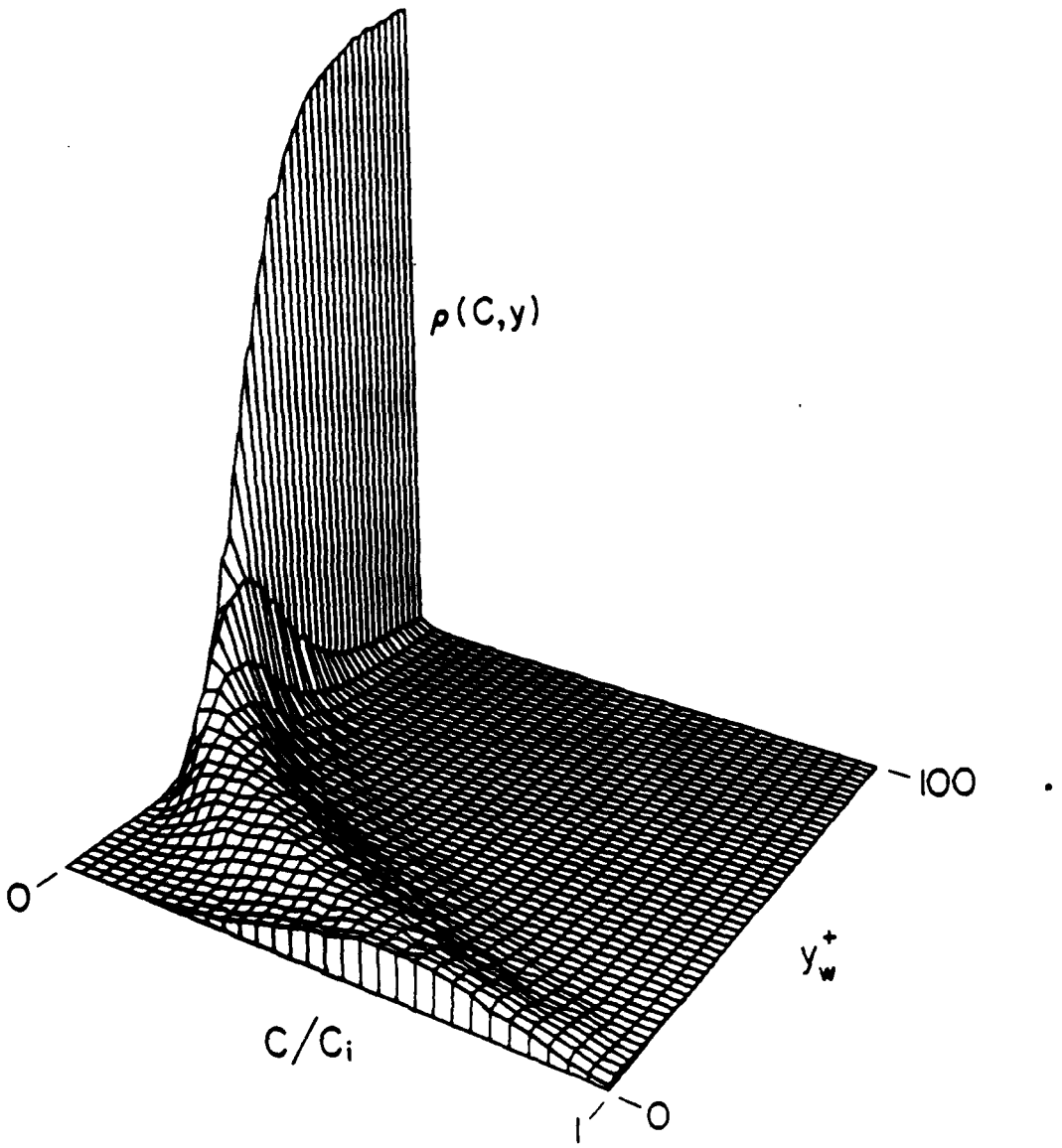

Figure 4.9 Probability density function for polymer concentration versus distance from the wall and concentration for x=50 mm

Figures 4.10 and 4.11 show the last two streamwise stations. At these locations, the distributions near the wall become less broad and move toward zero concentration while presence of the polymer solution is detected at increasing distances from the wall.

It is interesting to note that at no time is the presence of pure water detected at the wall. This indicates that transport in this region is dominated by molecular diffusion and small scale turbulent mixing and that fluid from the outer flow rarely if ever penetrates all the way to the wall.

4.3 Time-averaged statistics

Figure 4.12 shows mean concentration profiles as a function of distance downstream of the injector for injection of dyed water. Again, the profiles are normalized with the injected concentration, C_i, and are plotted versus distance from the wall normalized with the kinematic viscosity and shear velocity of the water flow without injection. At x = 10 mm, the mean concentration at the wall is reduced to 0.65. The near-wall concentration is reduced by about one half at each succeeding streamwise location until it reaches less than 0.06 at x = 100 mm (when the polymer is mixed uniformly with the flow, the concentration is 0.0018). The thickness of the high-concentration wall layer increases steadily with streamwise distance from $y^+ = 70$ at x = 10 mm to $y^+ > 150$ at x = 100 mm. Figure 4.13 shows mean concentration profiles as a function of distance downstream of the injector for SEPARAN AP-273 injection. The near-wall mean concentration is 0.75 at x = 10 mm although this is probably slightly low due to the apparent concentration measurement error near the

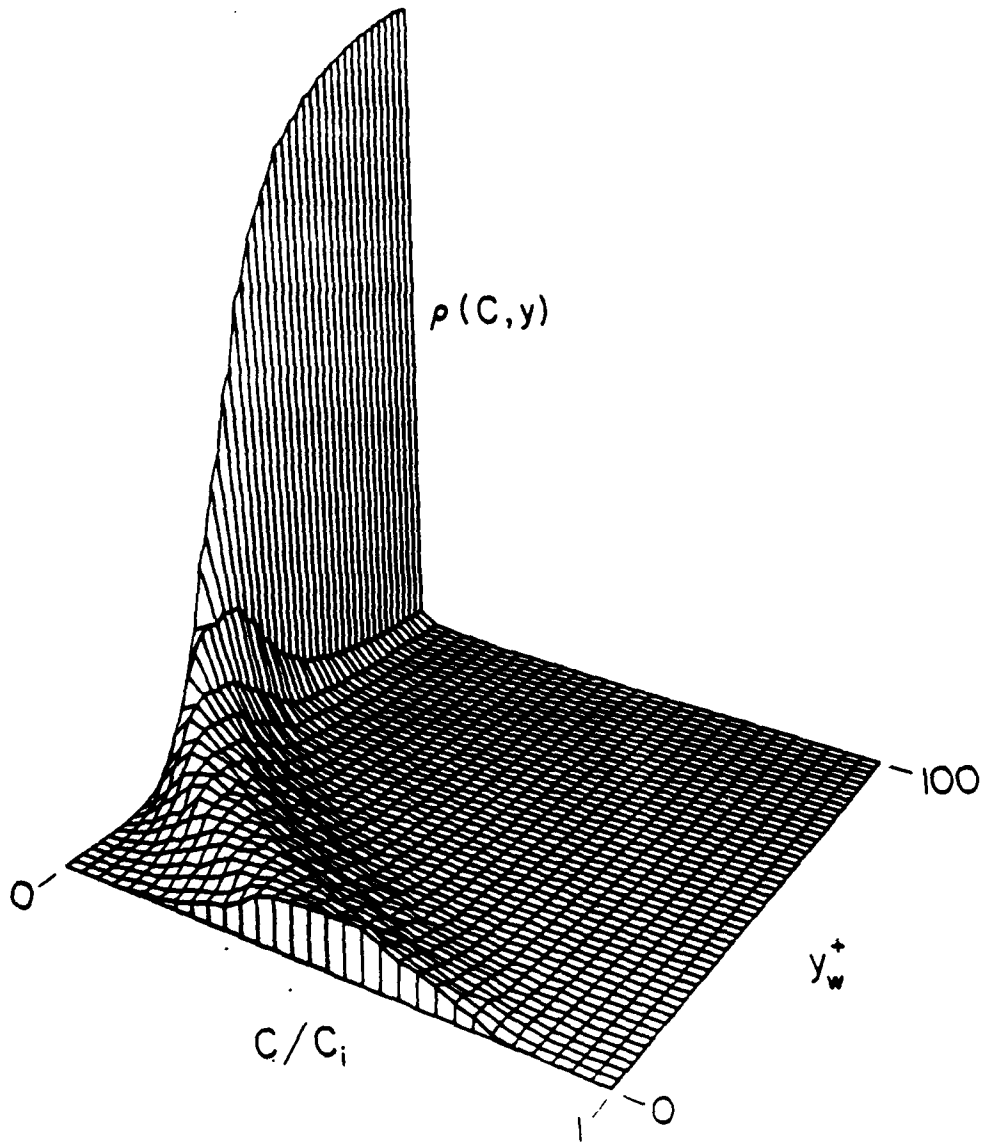

Figure 4.10 Probability density function for polymer concentration versus distance from the wall and concentration for x=100 mm

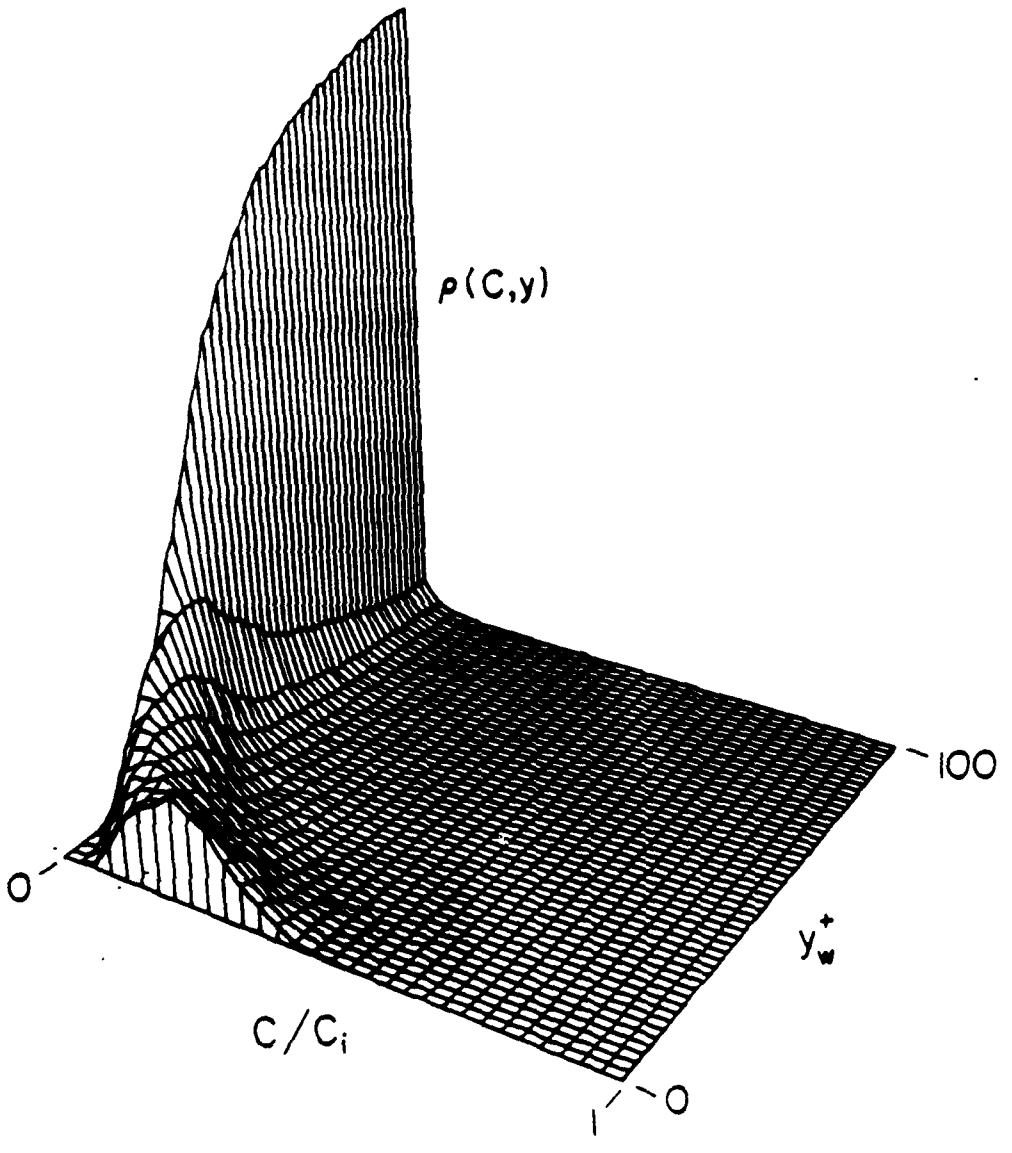

Figure 4.11 Probability density function for polymer concentration versus distance from the wall and concentration for x=200 mm

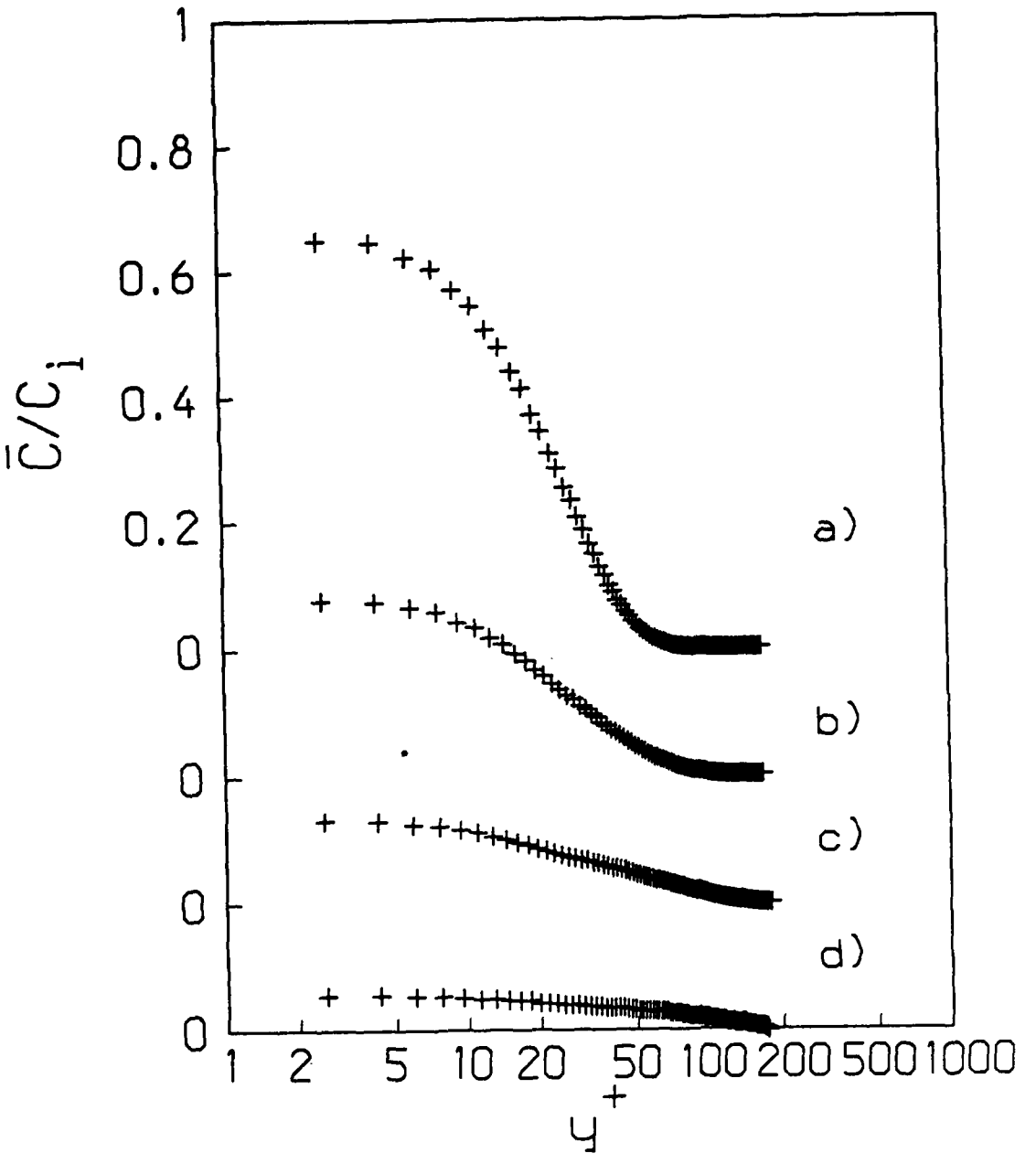

Figure 4.12 Mean concentration profiles for water injection: a) x = 10 mm, b) x = 25 mm, c) x = 50 mm, d) x = 100 mm.

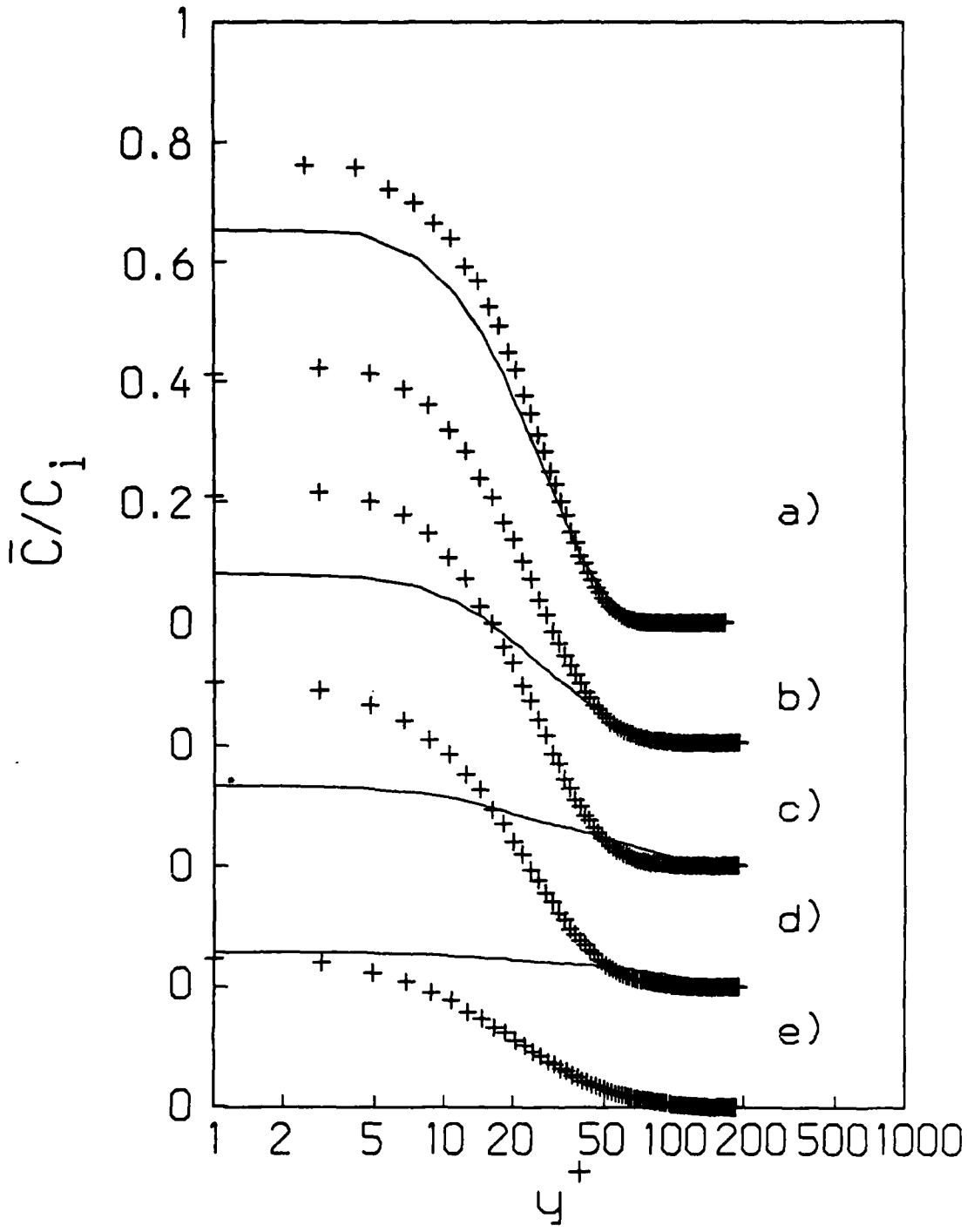

Figure 4.13 Mean concentration profiles for polymer injection: a) x = 10 mm, b) x = 25 mm, c) x = 50 mm, d) x = 100 mm, e) x = 200 mm; ———— , water injection results.

wall at this streamwise location. Near-wall concentration then levels off at about 0.62 from 25 to 50 mm downstream of the injector. At $x = 100$ mm the near-wall concentration is reduced to 0.5 and at 200 mm it is down to 0.25. For $x \leq 100$ mm the thickness of the high-concentration layer at the wall is about 75 wall units and only at $x = 200$ mm does it extend beyond $y^+=100$.

Although the water mixes more readily with the flow than the polymer solution, the mean concentration profiles at $x = 10$ mm are similar enough to indicate that the initial mixing is not strikingly different for the two cases. At $x = 50$ mm the mean concentration profile for polymer injection is virtually unchanged from that of $x = 25$ mm. This is evidence of a polymer-induced supression of turbulent mass transport in this streamwise region. At $x = 100$ mm, the suppression of the mass transport has decreased as indicated by the reduction in wall concentration from that of the previous location and at the last measurement station the mean concentrations are reduced considerably and the thickness of the high-concentration wall layer is growing.

Figure 4.14 shows the root-mean-square (RMS) concentration, c', as a function of y^+ for the injection of dyed water. At $x = 10$ mm the c' profile peaks at about $0.3C_i$ at $y^+\approx12$ and fluctuations exist out to $y^+=100$, significantly beyond the edge of the high-concentration wall layer (based on the mean concentration profile). With increasing streamwise distance, the peak in the RMS concentration profile broadens and moves further from the wall and non-zero RMS levels occur well beyond the y-location where the mean concentration profile approaches zero. RMS concentration profiles for polymer injection are presented in Figure 4.15. At $x = 10$ mm, the RMS concentration level is

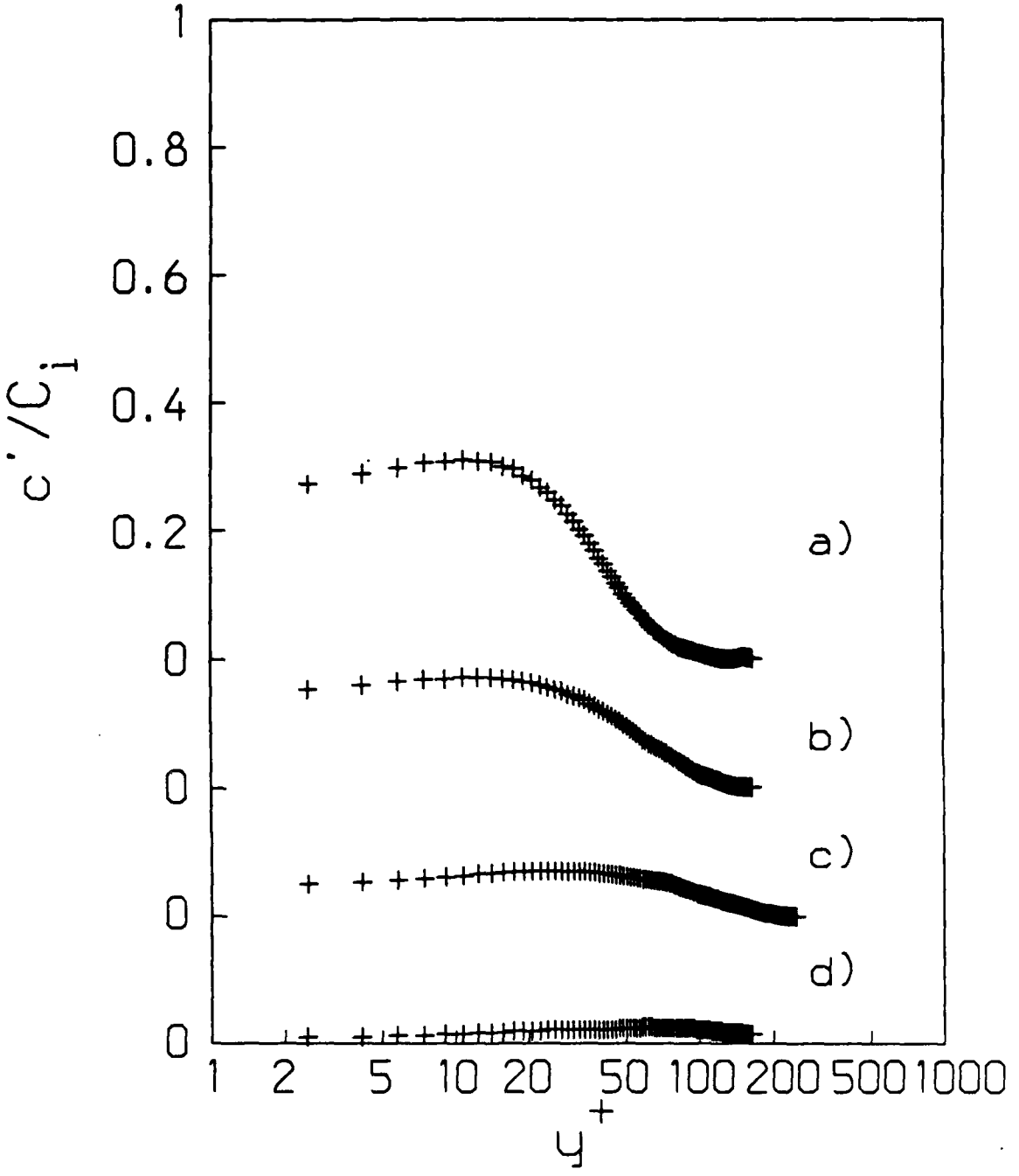

Figure 4.14 Root-mean-square concentration profiles for water injection: a) x = 10 mm, b) x = 25 mm, c) x = 50 mm, d) x = 100 mm.

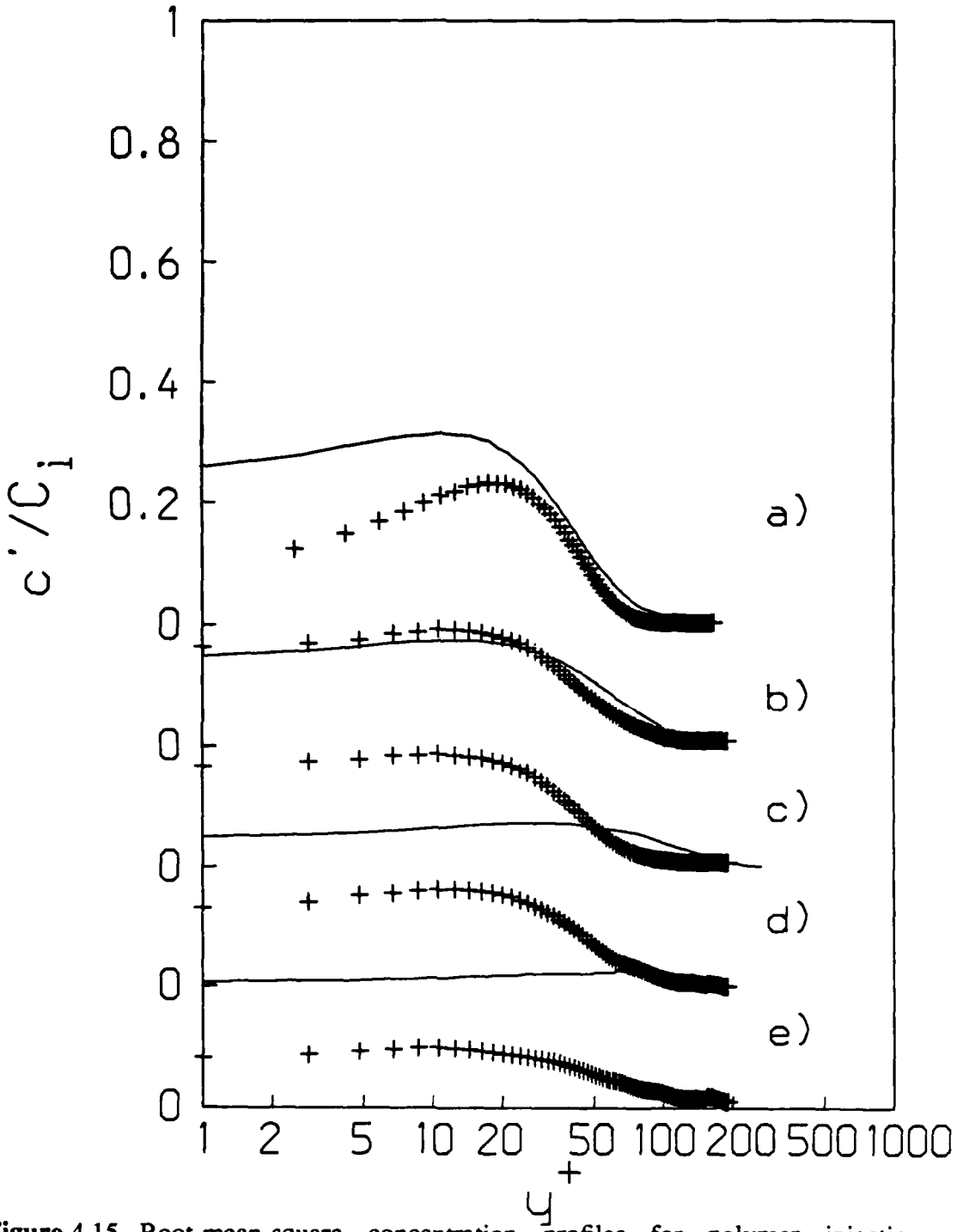

Figure 4.15 Root-mean-square concentration profiles for polymer injection: a) x = 10 mm, b) x = 25 mm, c) x = 50 mm, d) x = 100 mm, e) x = 200 mm; ———— , water injection results.

less than that for the water injection case across the entire flow. This is indicative of the decreased mixing when polymer solutions are injected. At the next streamwise location, x = 25 mm, the peak fluctuation level has decreased. The reduced fluctuation level near the wall shows that the concentration in the high-concentration layer is more uniform than at the upstream station. Here, the fluctuation level approaches zero at the edge of the high-concentration layer indicating that there is minimal mixing between the wall layer and outer region. At x = 50 mm the RMS concentration profile is essentially unchanged but at x = 100 mm and 200 mm non-zero fluctuation levels extending beyond the high-concentration wall layer are evidence of increased transport of the polymer solution from the wall region. This increased transport results in the decrease in near-wall concentration.

CHAPTER 5 - THE STRUCTURE OF TURBULENCE IN INJECTED FLOWS

To examine the effect of the evolving polymer concentration field on the structure of turbulence, two-component velocity measurements were made during polymer injection at the locations 25, 50, 100 and 200 mm downstream of the injector. To determine the effect of injection alone, two-component velocity measurements were made at $x = 25$ mm in the flow with water injection. Unless otherwise indicated, the results are normalized with the shear velocity of the water flow with no injection. The distance from the wall is normalized with this shear velocity and the kinematic viscosity of the channel water. These normalizations are for reference only and are not meant to imply any scaling arguments. Included, also for reference are lines representing the appropriate results from the water flow presented in Chapter 3.

5.1 Mean velocities

The mean velocity profile for the flow with water injection is shown in Figure 5.1. There is a slight acceleration near the wall, and a slight deceleration for y^+ from 30 to about 100. Outside of y^+ of 200 the injection has negligible effect. The region where the flow is modified corresponds roughly to the portion of the flow where the mean concentration is non-zero. Figure 5.2 shows the mean velocity profiles for x-locations between 25 and 200 mm downstream of the injectors during polymer injection. In contrast to the results for water injection, the outer flow ($y^+ \geq 50$) has

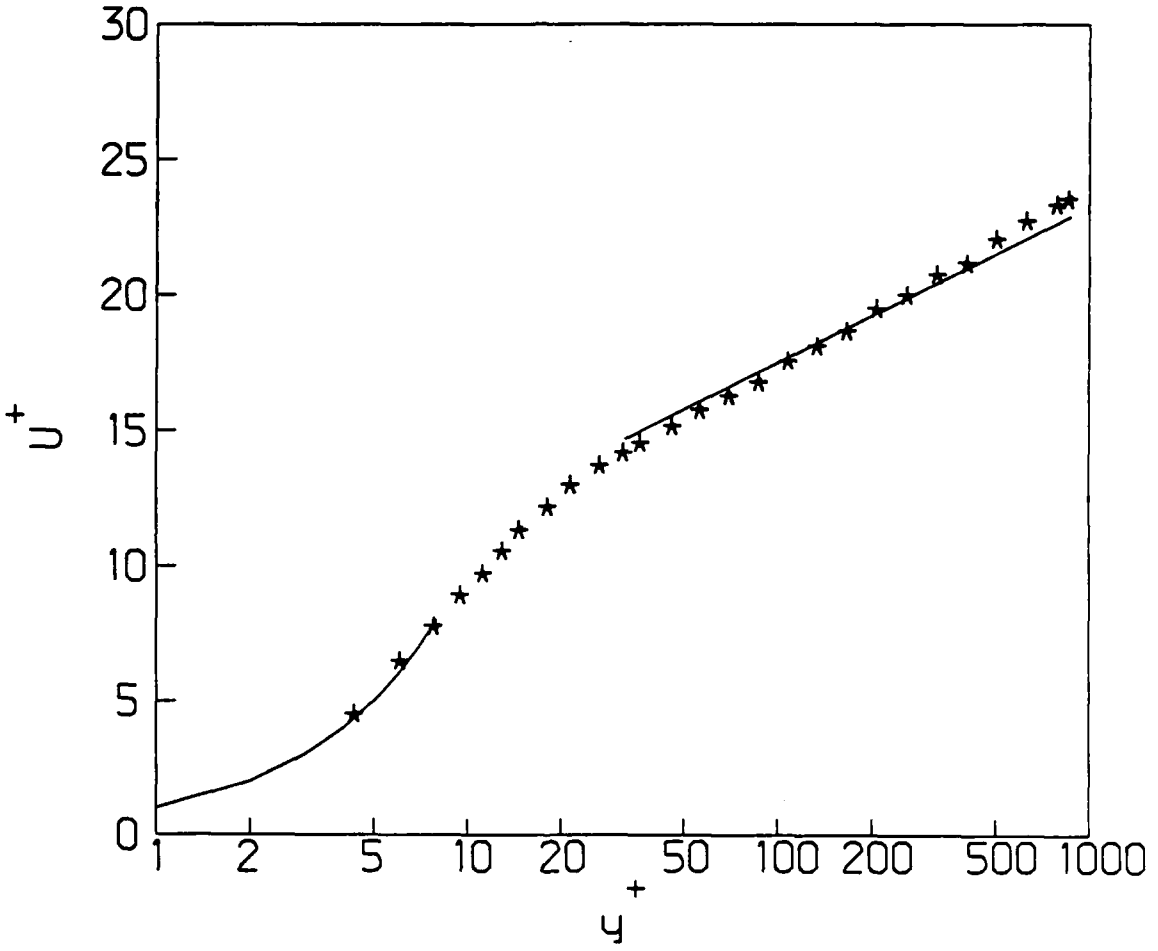

Figure 5.1 Mean velocity profile for flow with water injection; ———— , no-injection results.

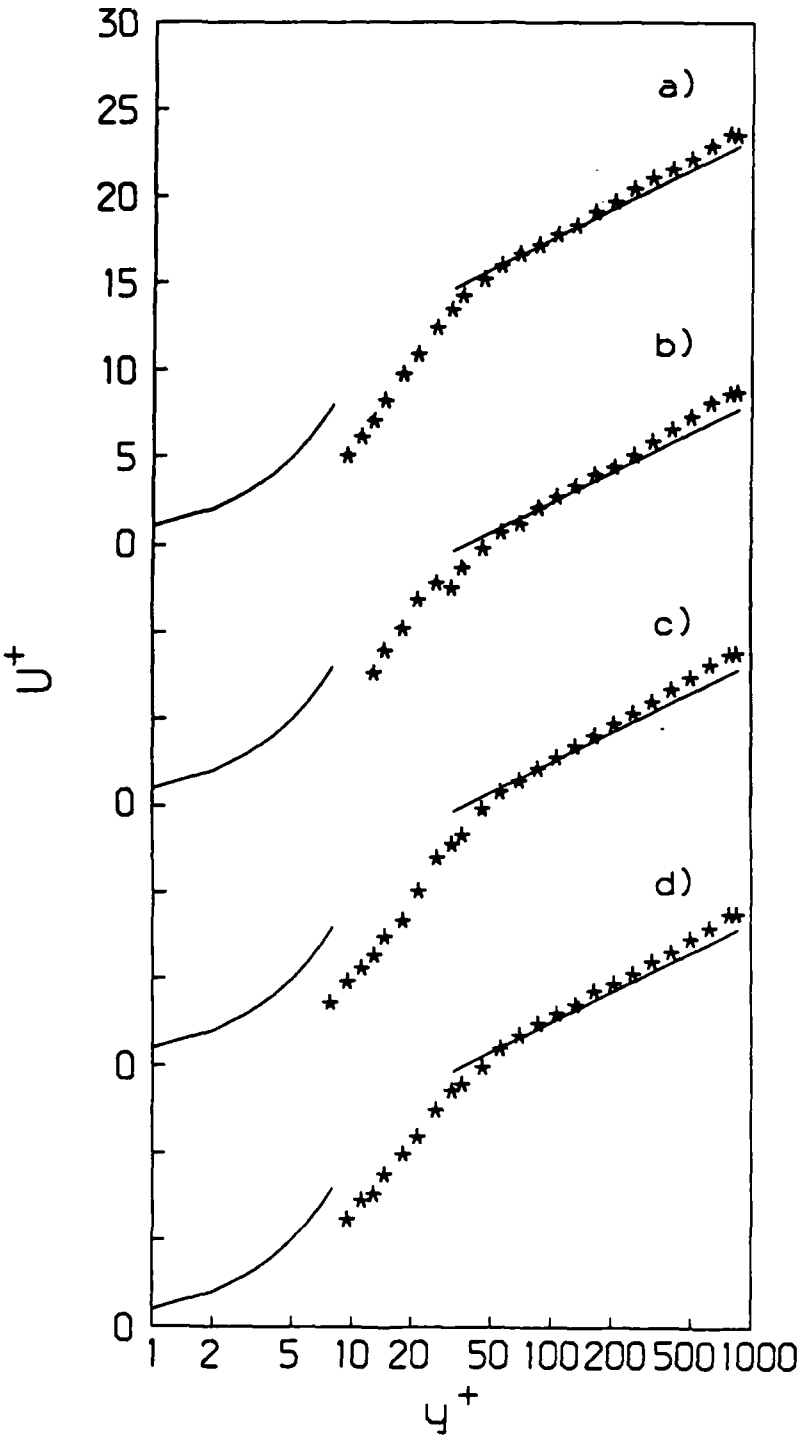

Figure 5.2 Mean velocity profiles for flow with polymer injection: a) x = 25 mm, b) x = 50 mm, c) x = 100 mm, d) x = 200 mm; ———— , no-injection results.

accelerated slightly for all streamwise locations while near the wall the flow has decelerated. This is the opposite of what occurred for water injection. The region of deceleration corresponds to the high-concentration wall layer indicating that the deceleration is related to the presence of the polymer solution (due to both an increase in viscosity and the onset of drag reduction). The reduction in velocity near the wall, which is responsible for the acceleration of the outer flow, is relatively constant for the first three locations and is slightly smaller at the 200 mm station.

5.2 Second moments

Root-mean-square velocity fluctuations normalized with the shear velocity for the flow with no injection are shown in Figure 5.3. It is clear from this figure that while u' is virtually unchanged, the RMS of the normal velocity is increased across the high-injectant-concentration portion of the flow compared to the flow with no injection. The turbulent shear stress for the water injection flow is shown in Figure 5.4. Compared to the water flow, there is a general increase in $-\overline{uv}$ in the near-wall, high concentration region. These results show that the major effects of the injection process on the structure of turbulence are to increase the turbulent shear stress and the RMS of the normal velocity in the near-wall, high-injectant-concentration region.

For polymer injection, the RMS fluctuation levels for the streamwise velocity are shown in Figure 5.5. There is a 15 percent increase in peak fluctuation level at all x-locations and the peak has moved outward from $y^+ = 15$ to about 30. Near the wall, the RMS level has decreased while in the region where the polymer concentration is small

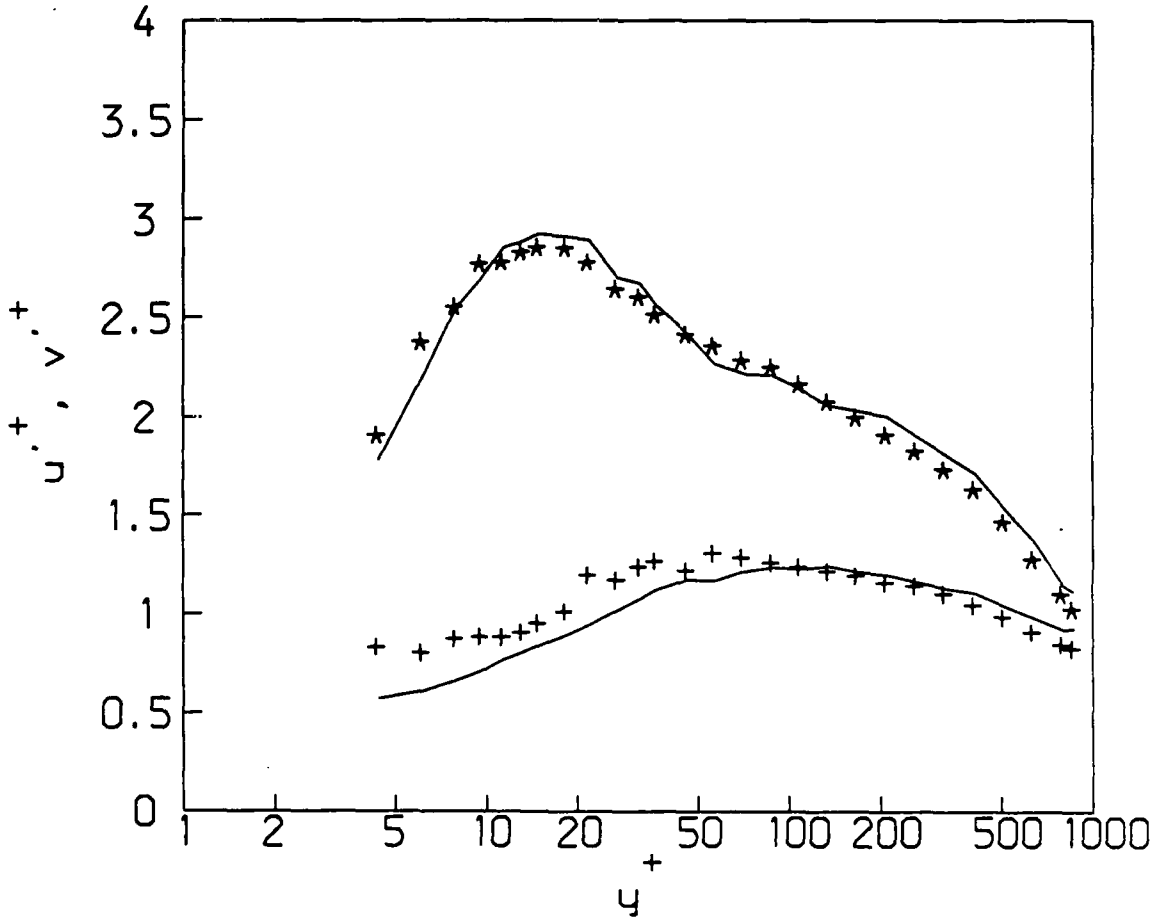

Figure 5.3 Root-mean-square velocity fluctuation profiles for flow with water injection: * , u'/u_τ; + , v'/u_τ; ———— , no-injection results.

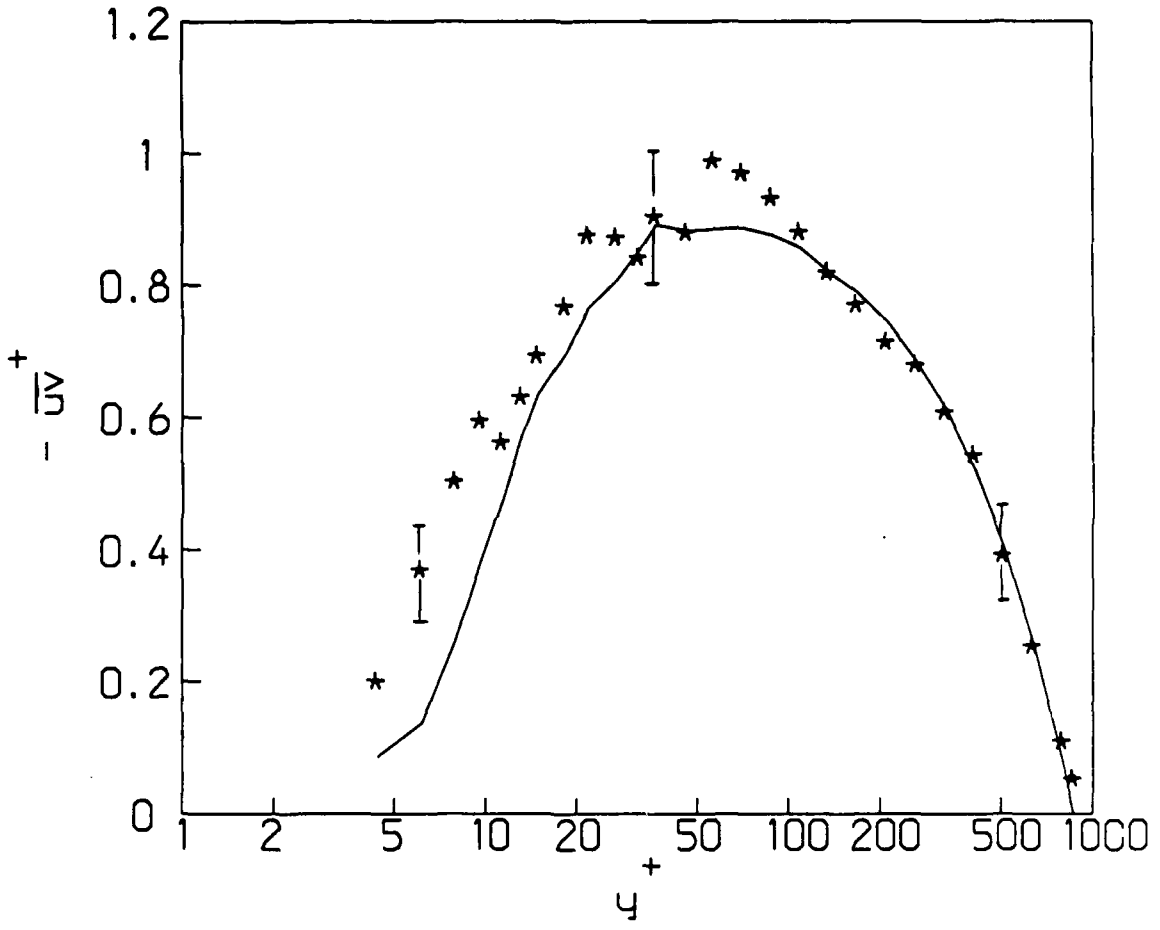

Figure 5.4 Turbulent shear stress profile for flow with water injection; ———, no-injection results; I , 95 % confidence interval.

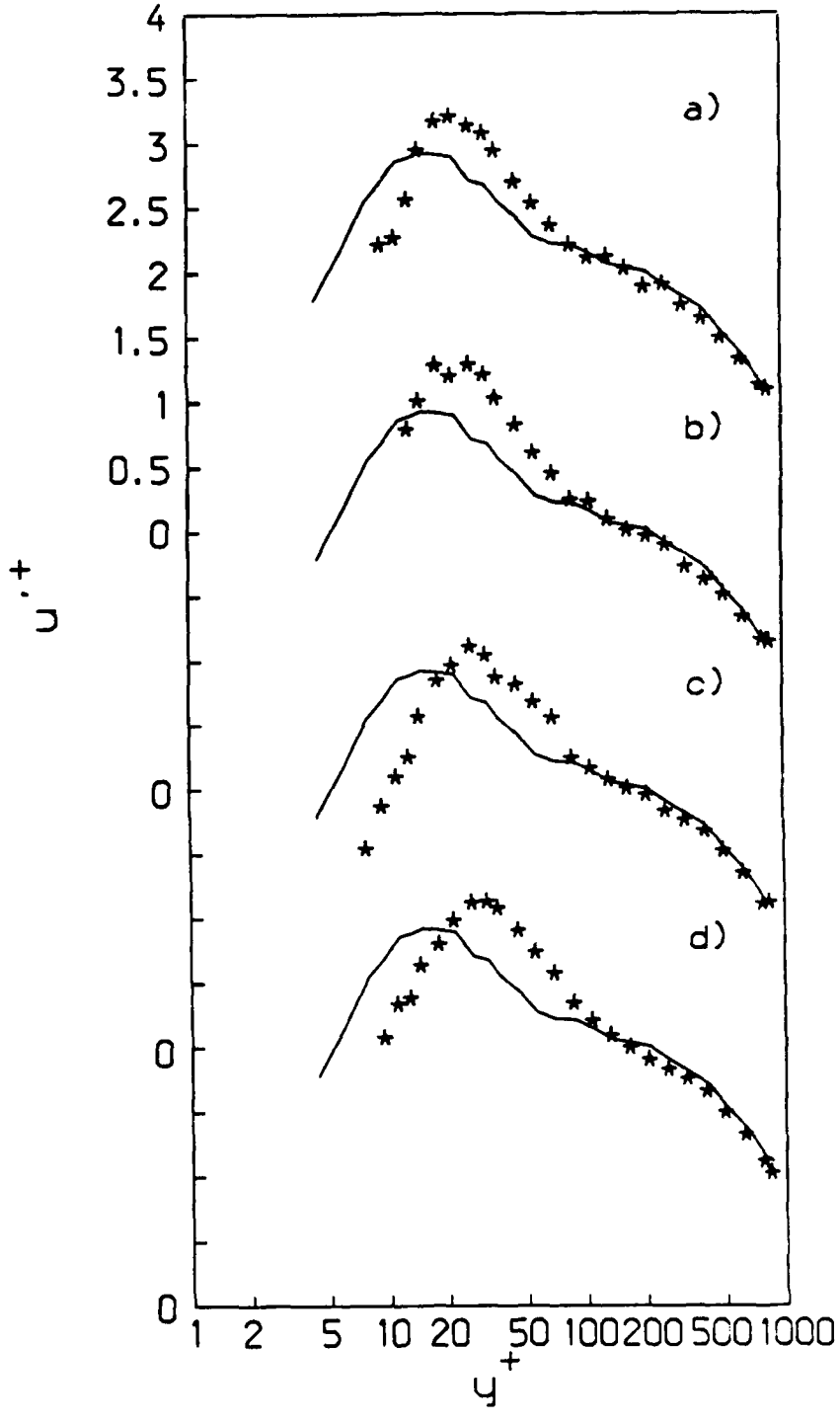

Figure 5.5 Root-mean-square velocity fluctuation (u'/u_τ) profiles for flow with polymer injection: a) x = 25 mm, b) x = 50 mm, c) x = 100 mm, d) x = 200 mm; ————, no-injection results.

($y^+ \geq 50$) there is no change relative to the water flow. Figure 5.6 shows the RMS fluctuation level of the normal velocity. At x = 25 mm the RMS level is increased near the wall, similar to the behavior in the flow with water injection. Near the wall, v′ decreases with streamwise distance except for $y^+ < 10$ where there is no change. (Due to the apparent inaccuracy of the measurement of v′ in the region $y^+ < 10$ it is likely that this does not accurately reflect the turbulence structure for $y^+ < 10$.) The damping of v′ extends significantly beyond the high-concentration wall layer (based on the mean concentration profile) for x = 100 mm and 200 mm. Similar behavior was seen by Walker and Tiederman (1987). This previous study, which examined only mean concentration profiles, did not show, however,that the polymer solution instantaneously extends beyond $y^+ = 150$ yielding non-zero RMS concentration levels in this region.

Reynolds shear stress profiles for polymer injection are shown in Figure 5.7. At x = 25 mm the maximum in $-\overline{uv}$ is about 15 percent higher than the water flow. This level is significantly higher than for the flow with water injection. Elevated $-\overline{uv}$ levels persist to the next streamwise station x = 50 mm. In a manner similar to that for v′, $\overline{uv}$ is reduced in the near-wall region and this effect extends beyond the high-concentration layer at the two downstream locations.

The correlation coefficient R_{uv} is shown in Figure 5.8 for the flow with polymer injection. At x = 100 mm and 200 mm, R_{uv} is significantly decreased in the near-wall region. This means that the decreased $-\overline{uv}$ levels which occur at these streamwise locations are not a result of a general decrease in the fluctuation level, but result from a smaller contribution from the fluctuations to net momentum transport.

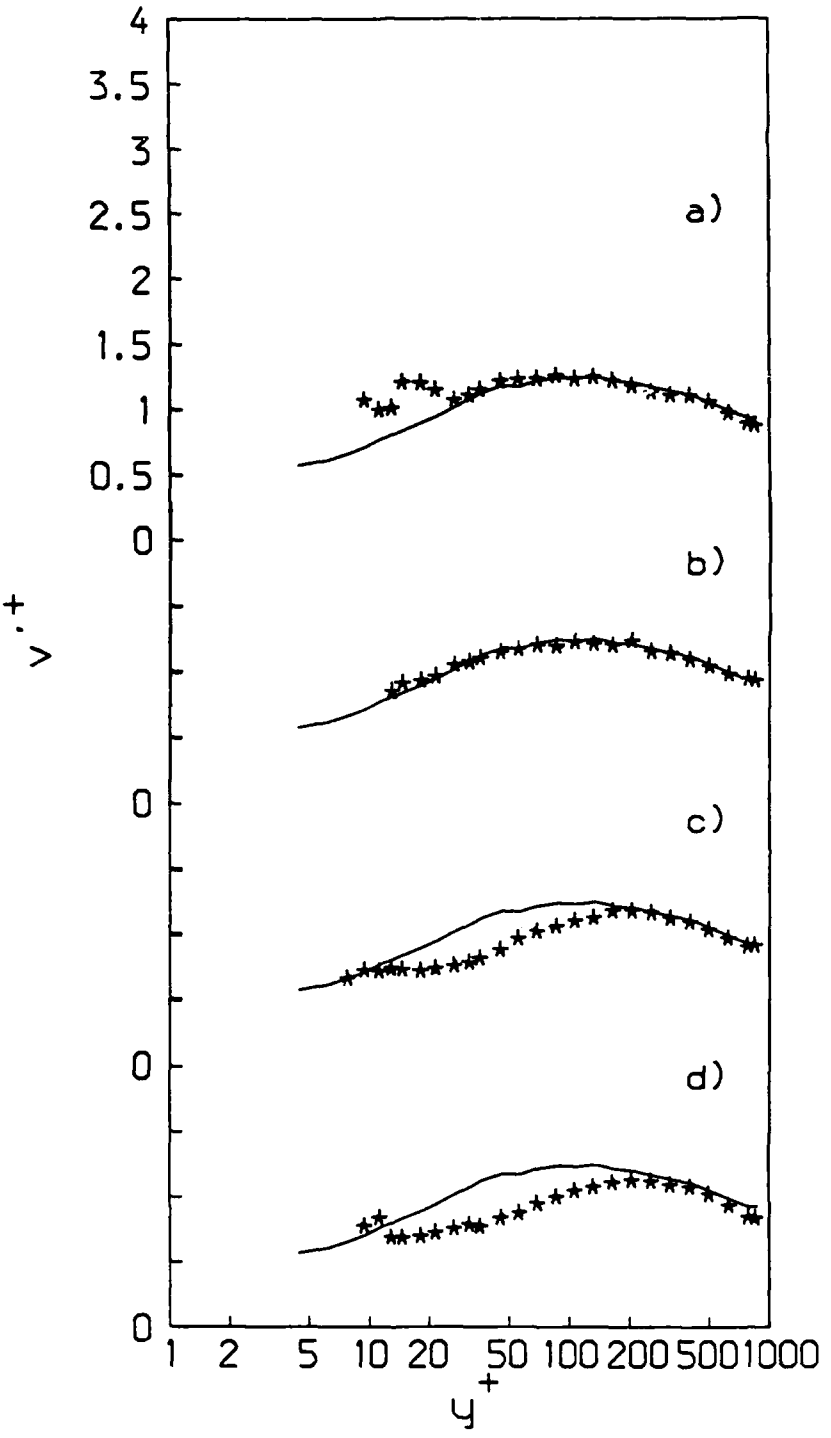

Figure 5.6 Root-mean-square velocity fluctuation (v'/u_τ) profiles for flow with polymer injection: a) x = 25 mm, b) x = 50 mm, c) x = 100 mm, d) x = 200 mm; ————, no-injection results.

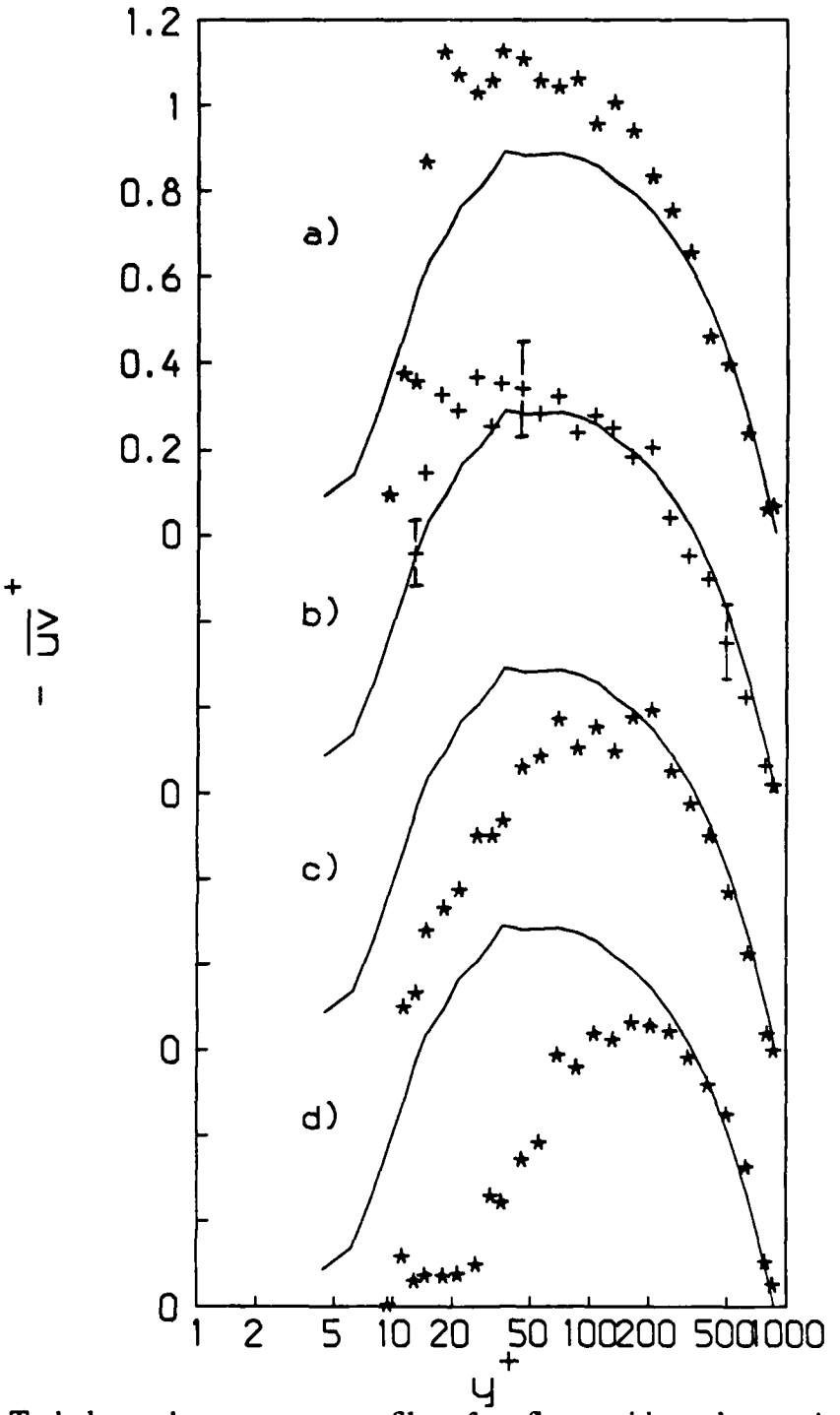

Figure 5.7 Turbulent shear stress profiles for flow with polymer injection: a) x = 25 mm, b) x = 50 mm, c) x = 100 mm, d) x = 200 mm; ———— , no-injection results; I , 95 % confidence interval.

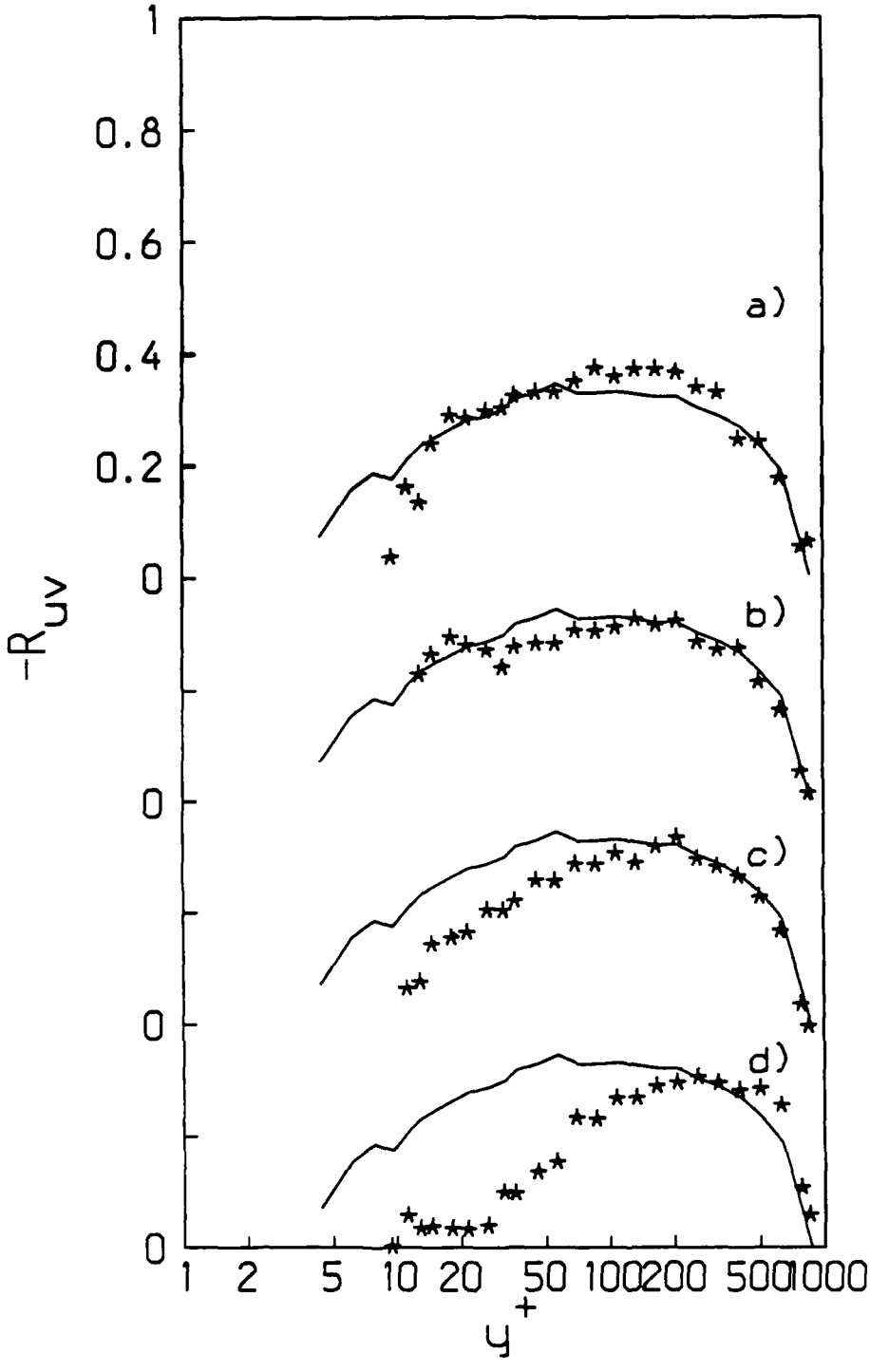

Figure 5.8 Correlation coefficient for flow with polymer injection: a) x = 25 mm, b) x = 50 mm, c) x = 100 mm, d) x = 200 mm; ———— , no-injection results.

5.3 Reynolds stress production

Figures 5.9 and 5.10 show the production terms which appear in the Reynolds stress transport equations. For the normal stress $\overline{u^2}$, shown in Figure 5.9, production (term I in Equation 3.6) is increased at x = 25 mm and 50 mm due to the increase in $\overline{uv}$ as a result of the injection process. At x = 100 mm the production has significantly decreased in the high-mean-concentration wall-region and at x = 200 mm, production has been virtually eliminated. Shear stress production (term I in Equation 3.8), shown in Figure 5.10, shows a marked increase at the two upstream locations due to the increase in v′ resulting from the injection process. At the two downstream locations, production is essentially the same as in the water flow.

These results are surprising in light of the behavior of the Reynolds stresses themselves. Although normal-stress production is virtually eliminated by x = 200 mm, u′ remains elevated and essentially constant with respect to distance from the injector; meanwhile, v′ decreases with streamwise distance. An increase or decrease in the rate of the destruction due to viscous stress fluctuations (term VI in Equations 3.5 through 3.8) would affect all stresses more or less equally since over the range of length scales which contribute to term VI the turbulence is nearly isotropic. As was discussed in Chapter 3 (and shown in Spalart, 1988 and Mansour et al., 1988), energy is transferred from $\overline{u^2}$ to $\overline{v^2}$ through the pressure-strain correlations (term II). An increase in $\overline{u^2}$ and decrease in $\overline{v^2}$ indicates that this transfer has been inhibited by the presence of the polymer solution. This assumes, of course, that neither the Reynolds stress transport equations nor their interpretation is altered significantly by the polymer.

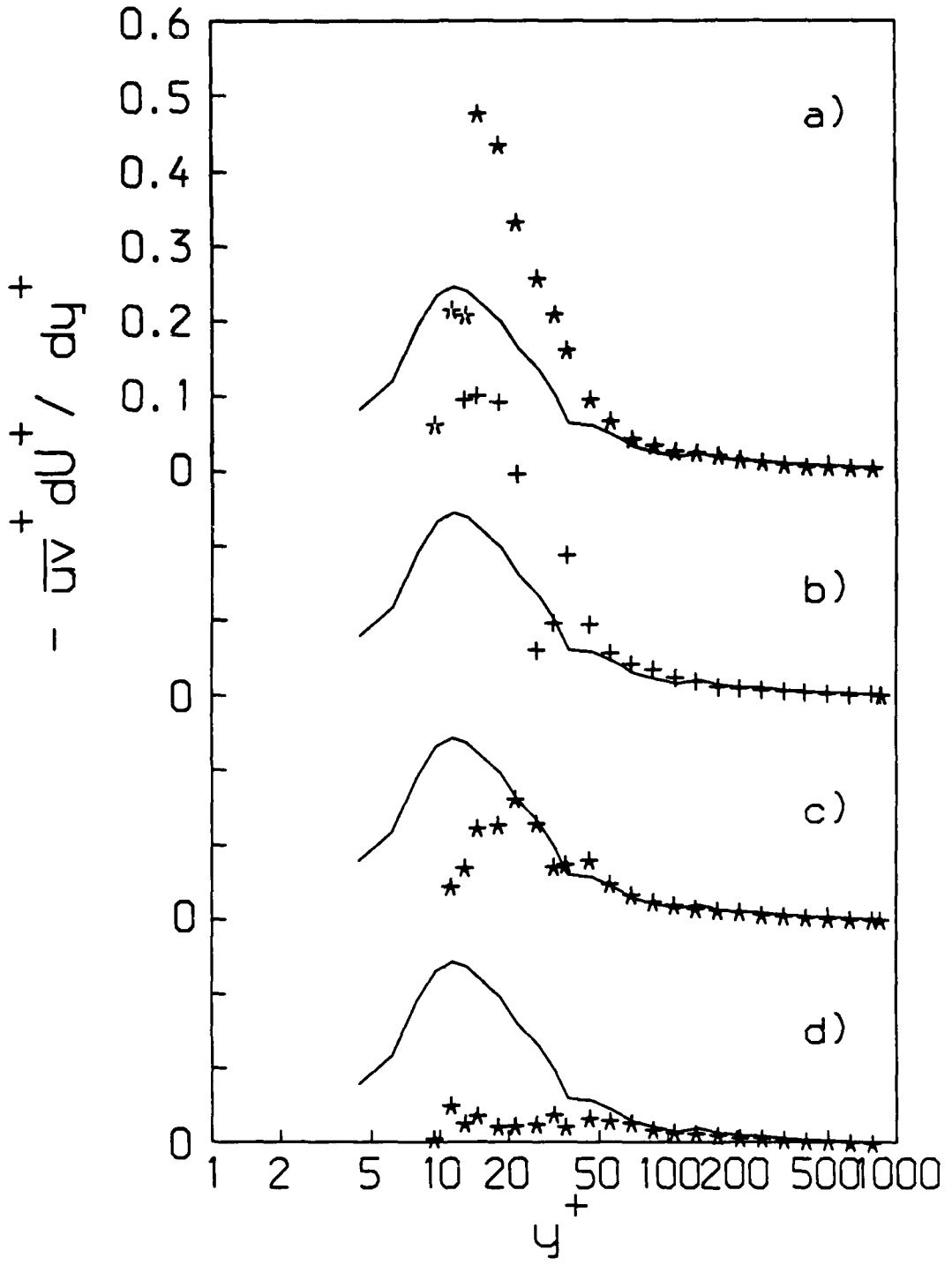

Figure 5.9 Reynolds stress production ($\overline{u^2}$ component) for flow with polymer injection: a) x = 25 mm, b) x = 50 mm, c) x = 100 mm, d) x = 200 mm; ———— , no-injection results.

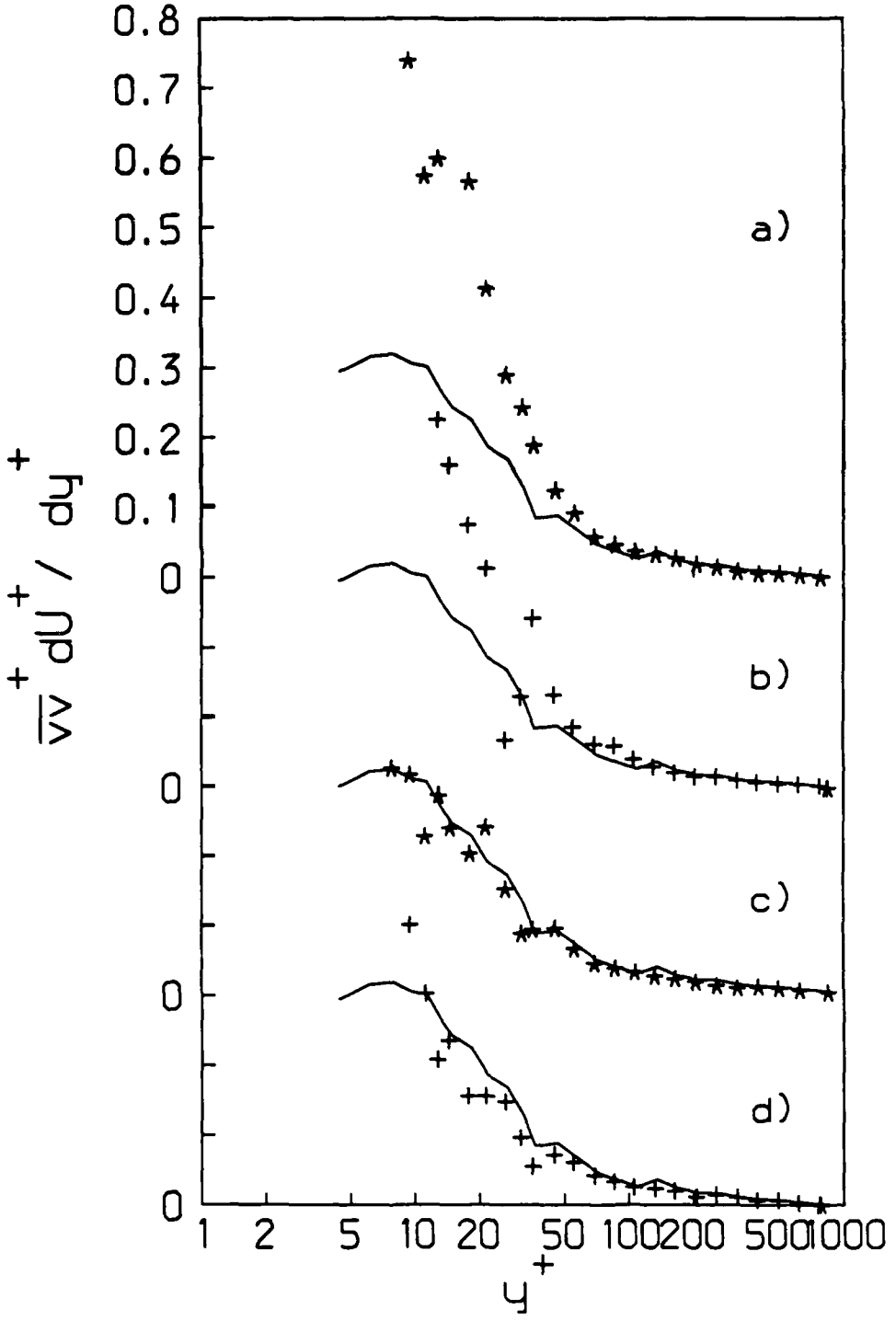

Figure 5.10 Reynolds stress production ($\overline{uv}$ component) for flow with polymer injection: a) x = 25 mm, b) x = 50 mm, c) x = 100 mm, d) x = 200 mm; ———— , no-injection results.

The turbulent shear-stress was observed to decrease significantly with streamwise position while the production rate for this stress was essentially unchanged from that of the water flow. Spalart (1988) and Mansour et al. (1988) showed that viscous stress fluctuations play only a minor role in the destruction of the turbulent shear-stress; the dominant quantity is the pressure-strain correlation (term II). This indicates that the mechanism which apparently inhibits the transfer of energy between the normal-stresses may also cause increased destruction of the Reynolds shear-stress.

CHAPTER 6 - TURBULENT MASS TRANSPORT

Turbulent mass transport ($\overline{vc}$) profiles were measured at the same four streamwise locations in the flow with polymer injection and at $x = 25$ mm in the flow with water injection. Data were acquired for y-locations extending from the edge of the high mean-concentration layer to as near the wall as possible.

The present results represent a unique physical situation when compared to scalar transport results presented in the literature. Most scalar transport investigations involve heat transfer with either constant wall heat-flux or a constant wall temperature and Prandtl numbers near unity. Due to the similarity in boundary conditions for the momentum and energy equations, the structure of the velocity and temperature fields are similar. This results in similarity between the $\overline{v\theta}$ and $\overline{uv}$ profiles (see e.g. Antonia et al., 1977 and Hishida et al., 1986). In this flow, the imposed zero-flux boundary condition at the wall ($\partial C/\partial y = 0$) and the high Schmidt number destroy this similarity.

6.1 Time-averaged turbulent mass transport

Figure 6.1 shows the $\overline{vc}$ correlation as a function of y^+ for the flow with water injection. Normalization is accomplished with the injected concentration and the shear velocity of the water flow with no injection. The $\overline{vc}$ profile does not appear to be similar to the $\overline{uv}$ profile for this flow. There is a sharp peak in the profile at about

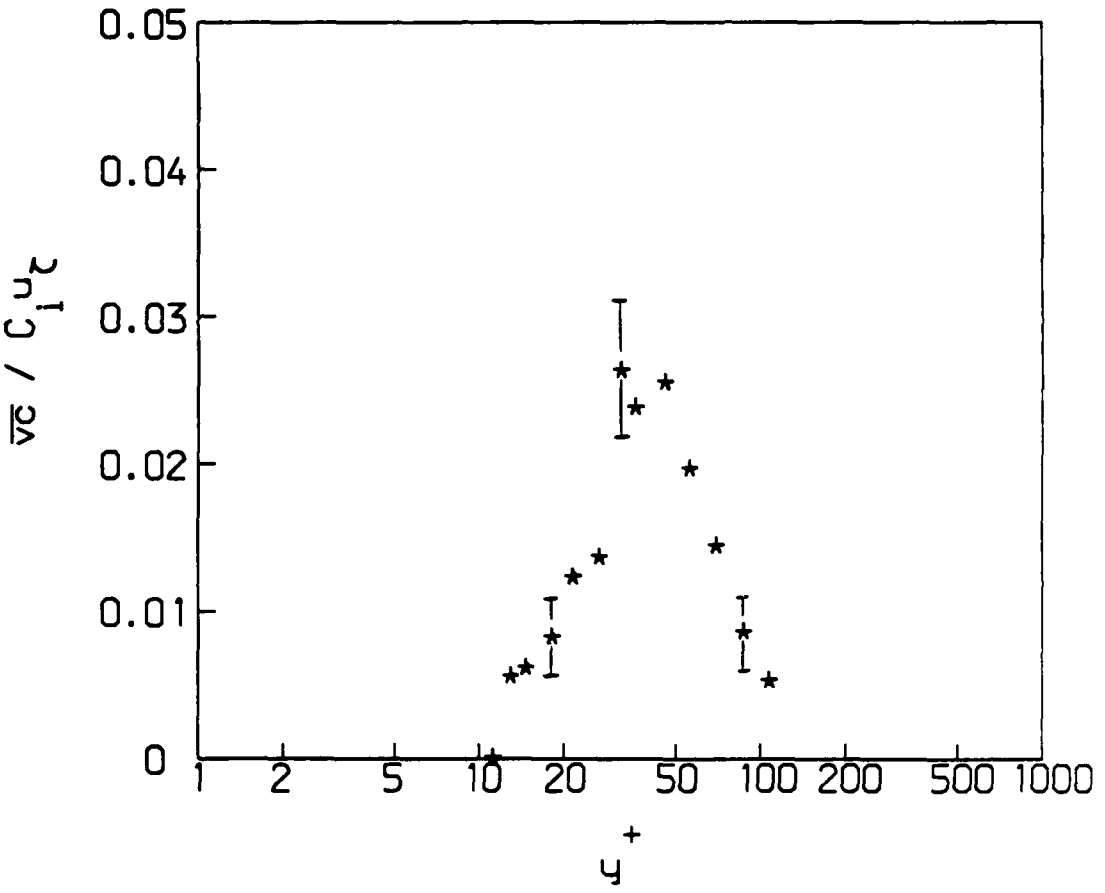

Figure 6.1 Turbulent mass transport profile at x = 25 mm for water injection; I , 95 % confidence interval.

$y^+ = 40$. This peak corresponds roughly with the inflection point in the mean concentration profile but does not correlate with any major feature of the RMS velocity or concentration profiles.

The $\overline{vc}$ product for the flow with polymer injection is shown in Figure 6.2. As expected, $\overline{vc}$ levels are near zero at x = 25 mm and 50 mm. Due to the small levels for $\overline{vc}$ the uncertainty is high (about 30 percent of the measured value); however, the sign of the $\overline{vc}$ product is believed to be correct. The interpretation of these negative values is uncertain. At the two downstream locations, the turbulent mass transport levels off with a peak at about 0.01. The behavior of $\overline{vc}$ is in good agreement with the foregoing discussion of the mean and RMS concentration profiles. The $\overline{vc}$ levels during polymer injection are significantly less than those measured during the injection of dyed water. This is not unexpected; since the polymer requires considerably more streamwise distance to mix completely with the flow, the mass transport normal to the wall must be less.

The correlation coefficient for mass transport, $R_{vc} = \overline{vc}/v'c'$, for the flow with water injection is shown in Figure 6.3. The R_{vc} profile peaks at about 0.15 in the region from y^+ of 30 to 100. This indicates that the normal-velocity and concentration fluctuations are less strongly correlated than $\overline{uv}$. R_{vc} for the flow with polymer injection is shown if Figure 6.4. (Note that the scale for Figure 6.4 is different than Figure 6.3.) At the two upstream locations, R_{vc} is less than 0.05 indicating that what fluctuations exist contribute little to the mass transport process. R_{vc} increases with streamwise distance until values comparable to those in the water flow occur at

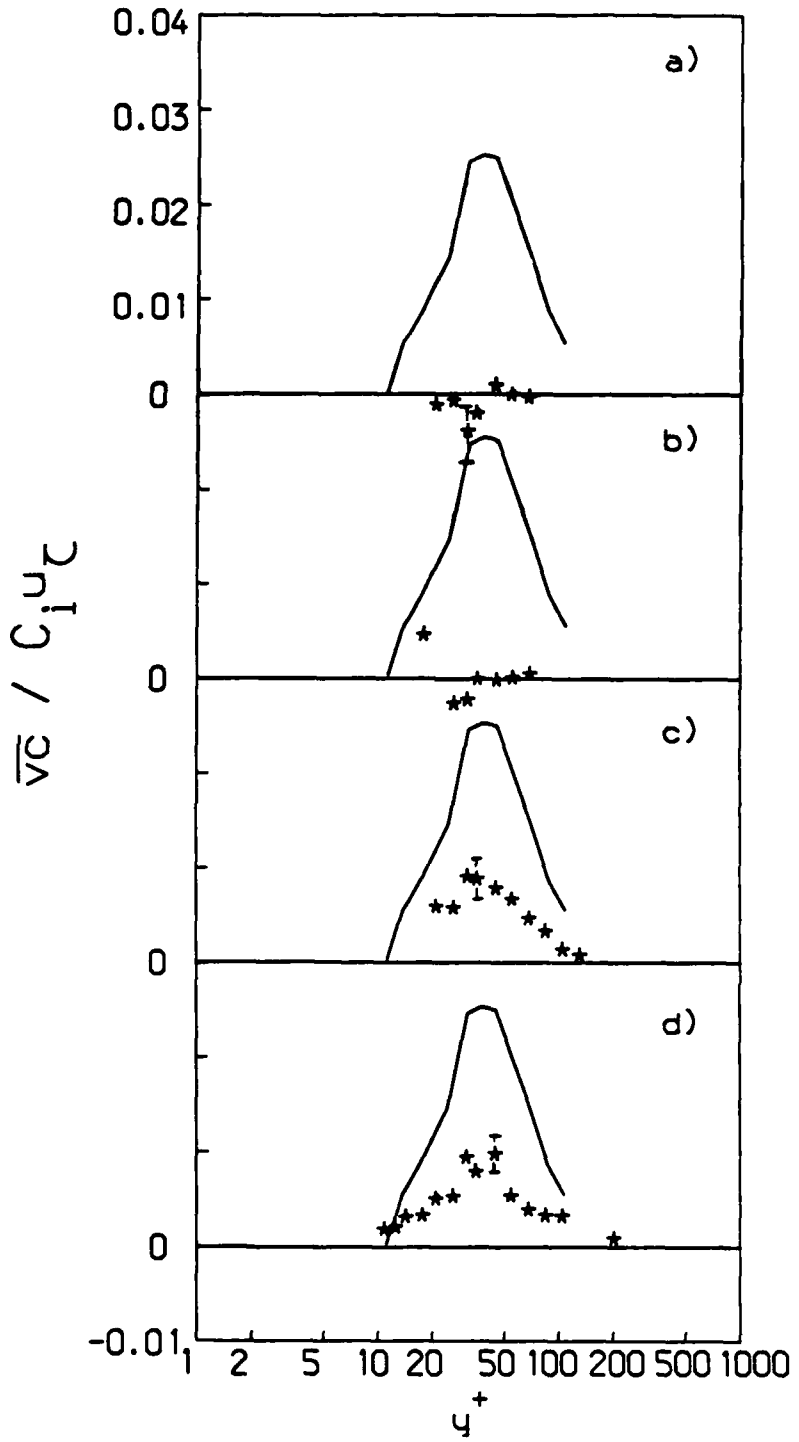

Figure 6.2 Turbulent mass transport profiles for polymer injection: a) x = 25 mm, b) x = 50 mm, c) x = 100 mm, d) x = 200 mm; ———— , x = 25 mm for water injection; I , 95 % confidence interval.

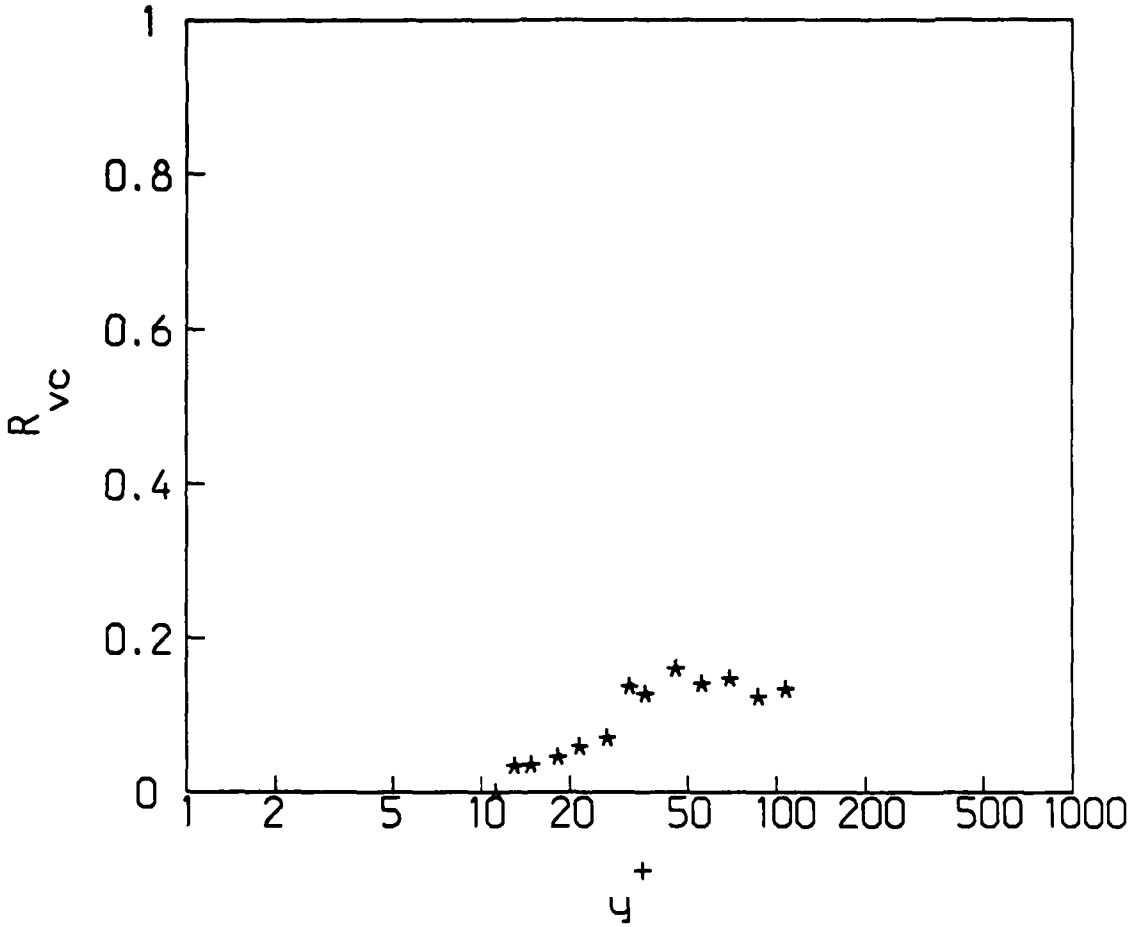

Figure 6.3 Mass-transport correlation coefficient profile at x = 25 mm for water injection.

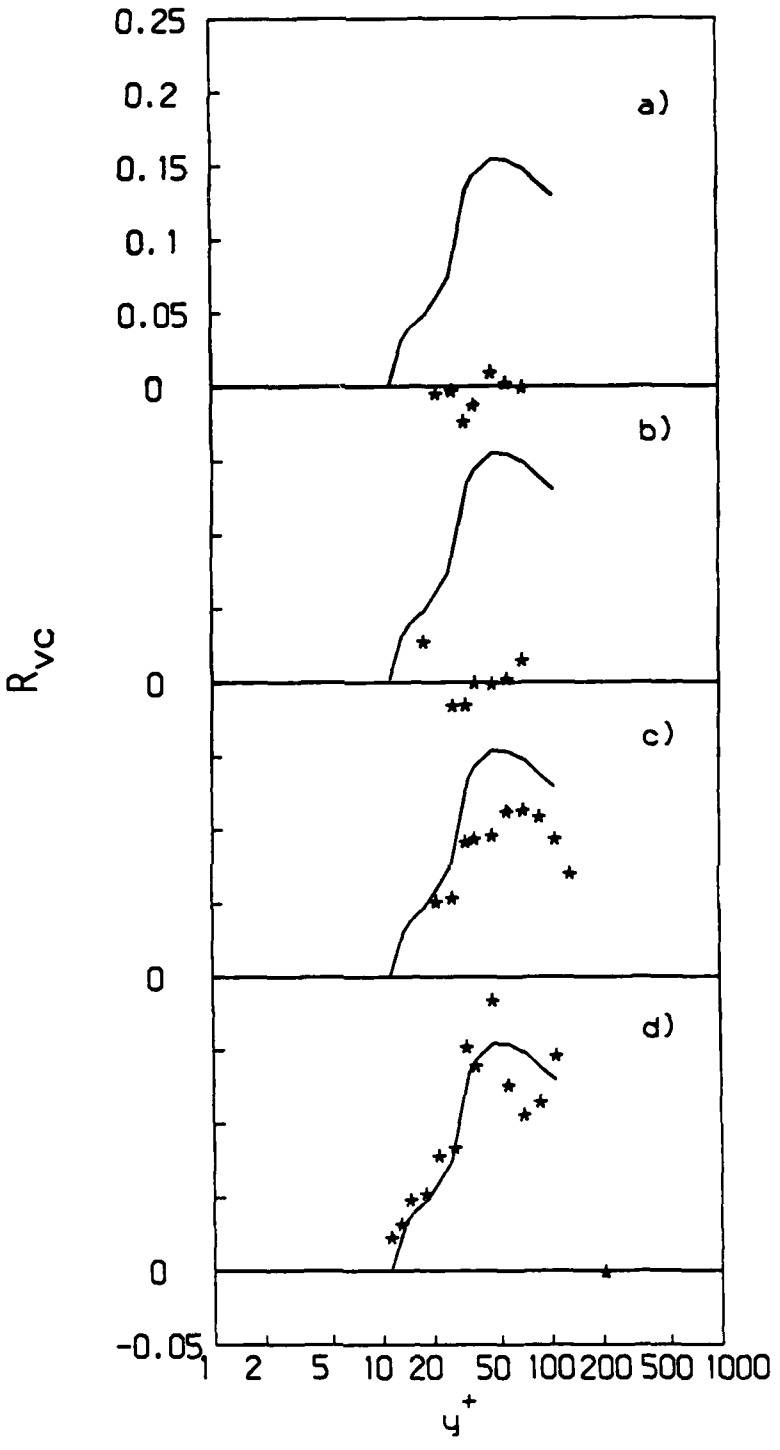

Figure 6.4 Mass-transport correlation coefficient profiles for polymer injection: a) x = 25 mm, b) x = 50 mm, c) x = 100 mm, d) x = 200 mm; ———— , x = 25 mm for water injection.

x = 200 mm, the last streamwise measurement location.

These results show that very little net transport away from the wall occurs in the polymer flow for x < 100 mm as was inferred from the mean concentration profiles, the time-resolved concentration profiles and the probability density functions for concentration. The occurence of comparable values of the correlation coefficient for x = 200 mm in the polymer flow and x = 25 mm in the water injection case means that the same amount of mass transport occurs in each flow, given the magnitude of the velocity and concentration fluctuations. This implies similarity in the mass transport processes in these two cases.

6.2 The detailed structure of turbulent mass transport

In order to better understand the relationship between the normal-velocity and concentration fluctuations and the nature of the $\overline{vc}$ product, a more detailed analysis of the structure of the normal-velocity and concentration fluctuations is necessary. Figure 6.5 shows scatter diagrams of velocity and concentration fluctuations at x = 25 mm and y^+ = 88.3, 32.4 and 18.4 for water injection. The location y^+ = 32.4 corresponds to where $\overline{vc}$ is at a maximum and the locations on either side of this maximum are where $\overline{vc}$ was equal to one-third the maximum value. At all three locations, the distinct cut-off at a fixed negative concentration fluctuation value corresponds to zero concentration and the concentration distributions are highly skewed as was previously shown in the concentration probability density functions. At low concentrations, all possible values for the velocity fluctuations are present. For y^+ = 32.4, positive concentration fluctuations are more strongly correlated with positive velocity fluctuations resulting in

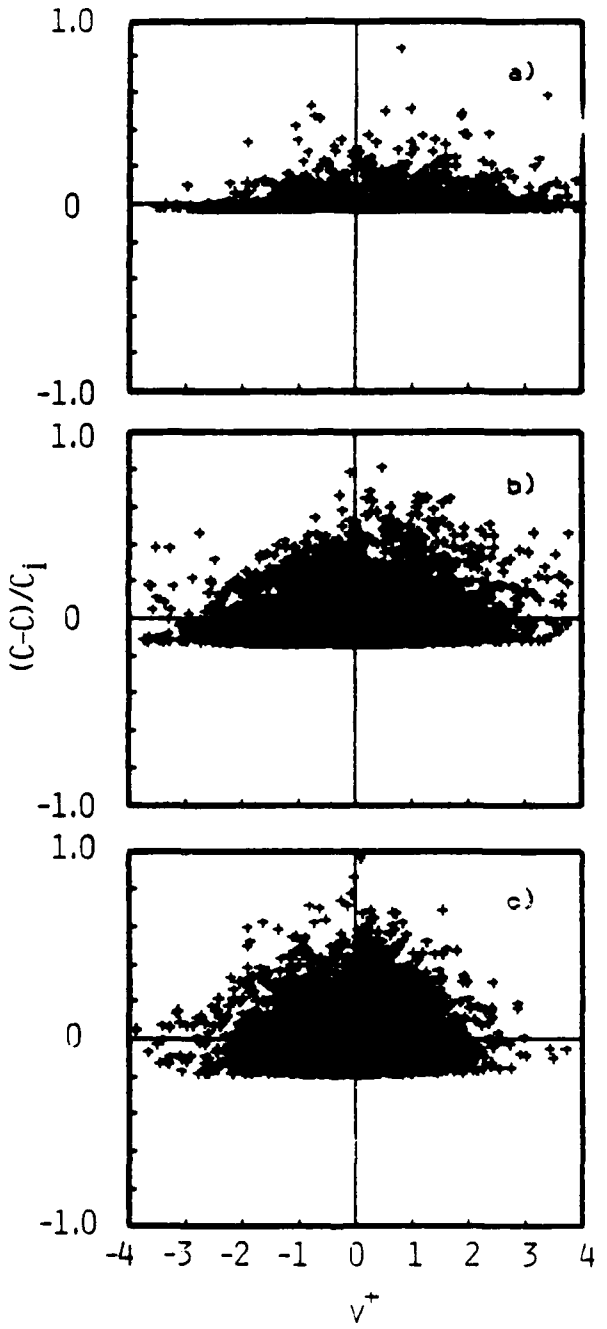

Figure 6.5 Velocity and concentration scatter diagrams for flow with water injection: x = 25 mm, a) $y^+ = 88.3$, b) $y^+ = 32.4$, c) $y^+ = 18.4$.

asymmetry of the distribution about the v axis. At $y^+ = 88.3$, the fluctuations in velocity are comparable to those at 32.4 while the concentration fluctuations are reduced considerably resulting in a decrease in $\overline{vc}$. Positive concentration fluctuations are more strongly correlated with positive velocities than negative velocities here also. The near-wall location exhibits concentration fluctuations that are comparable to those at the $\overline{vc}$ peak but reduced velocity fluctuations result in a decrease in $\overline{vc}$.

To determine how the normal-velocity fluctuations present at a point contribute to the net mass transport, the joint probability density function for velocity and concentration, f(v,c), defined such that

$$\int_{-\infty}^{\infty} \int_{-\infty}^{\infty} f(v,c)\, dc\, dv = 1 \tag{6.1}$$

was calculated. The first moment of the joint probability density function is

$$\overline{vc} = \int_{-\infty}^{\infty} \int_{-\infty}^{\infty} [v\, c\, f(v,c)]\, dc\, dv\,. \tag{6.2}$$

Integrating Equation 6.2 with respect to concentration only and normalizing with $\overline{vc}$ results in

$$1 = \int_{-\infty}^{\infty} F(v)\, dv \tag{6.3}$$

where

$$F(v) = \frac{1}{\overline{vc}} \int_{-\infty}^{\infty} [v\, c\, f(v,c)]\, dc\,. \tag{6.4}$$

The function F(v) shows the relative contribution of normal-velocity fluctuations of a given magnitude to $\overline{vc}$.

Figure 6.6 shows F(v) for the scatter diagrams in Figure 6.5. At $y^+ = 88.3$ the mass transport is primarily due to positive velocity fluctuations, i.e. high concentration fluid is being carried away from the wall. At the $\overline{vc}$ peak there is a substantial contribution to transport by negative velocity fluctuations along with a slightly larger contribution from positive velocities. This indicates that the transport consists of both movement of high concentration fluid away from the wall and movement of low concentration fluid toward the wall. This behavior is repeated at $y^+ = 18.4$ although the distribution is narrower due to the decrease in the velocity fluctuation levels.

Figure 6.7 shows scatter diagrams of velocity and concentration fluctuations at $x = 200$ mm and $y^+ = 109.2$, 27.1 and 13.1 for polymer injection. Again, the middle location corresponds to where $\overline{vc}$ is a maximum and the locations on either side are where $\overline{vc}$ was equal to one-third the maximum. At low concentrations, all possible values for the velocity fluctuations are present. For $y^+ = 27.1$, positive concentration fluctuations are correlated with positive velocity fluctuations resulting in asymmetry of the distribution about the v axis. The near-wall location again exhibits concentration fluctuations that are comparable to those at the $\overline{vc}$ peak but the velocity fluctuations are considerably reduced. This results in the reduced value for $\overline{vc}$. At $y^+ = 109.2$, the fluctuations in velocity are larger than those at the $\overline{vc}$ peak while the concentration fluctuations are reduced considerably resulting in a decrease in $\overline{vc}$. Here also, positive concentration fluctuations are more strongly correlated with positive velocities than negative velocities. At the two outer locations, there is a stronger correlation between large negative velocity fluctuations and near-zero concentrations (negative

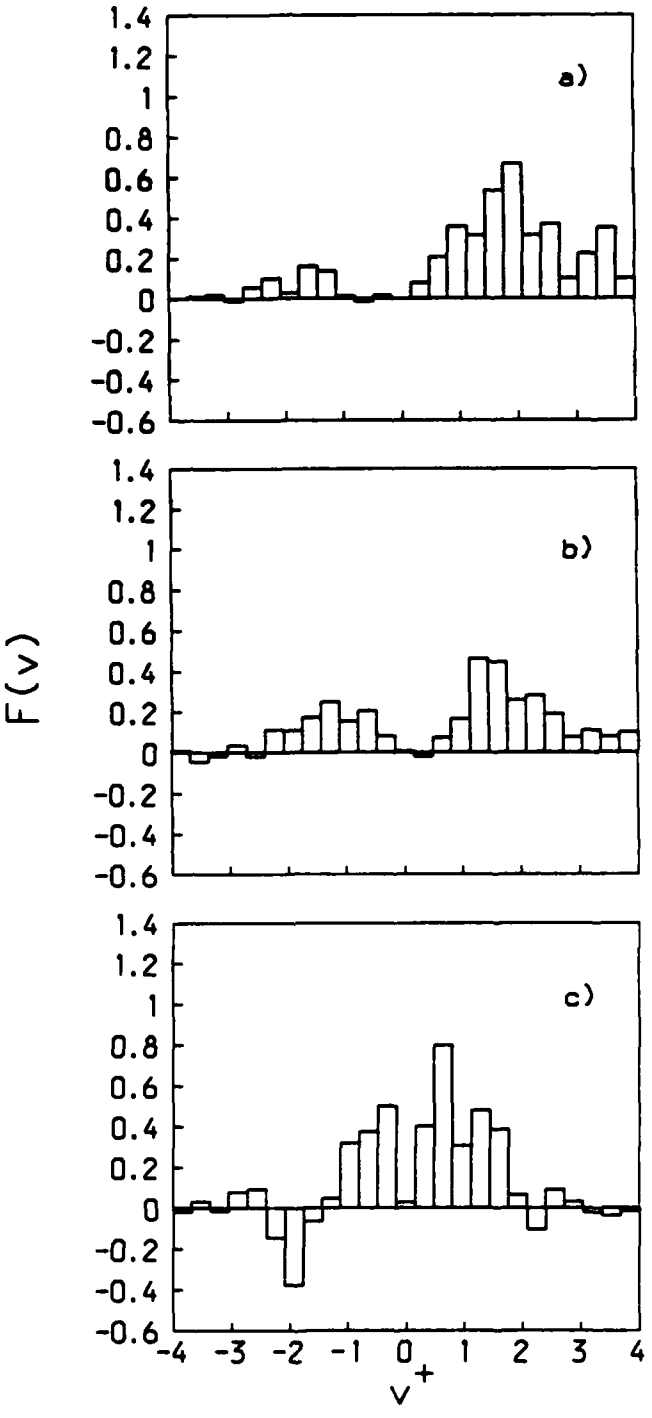

Figure 6.6 F(v) for flow with water injection: x = 25 mm, a) $y^+ = 88.3$, b) $y^+ = 32.4$, c) $y^+ = 18.4$.

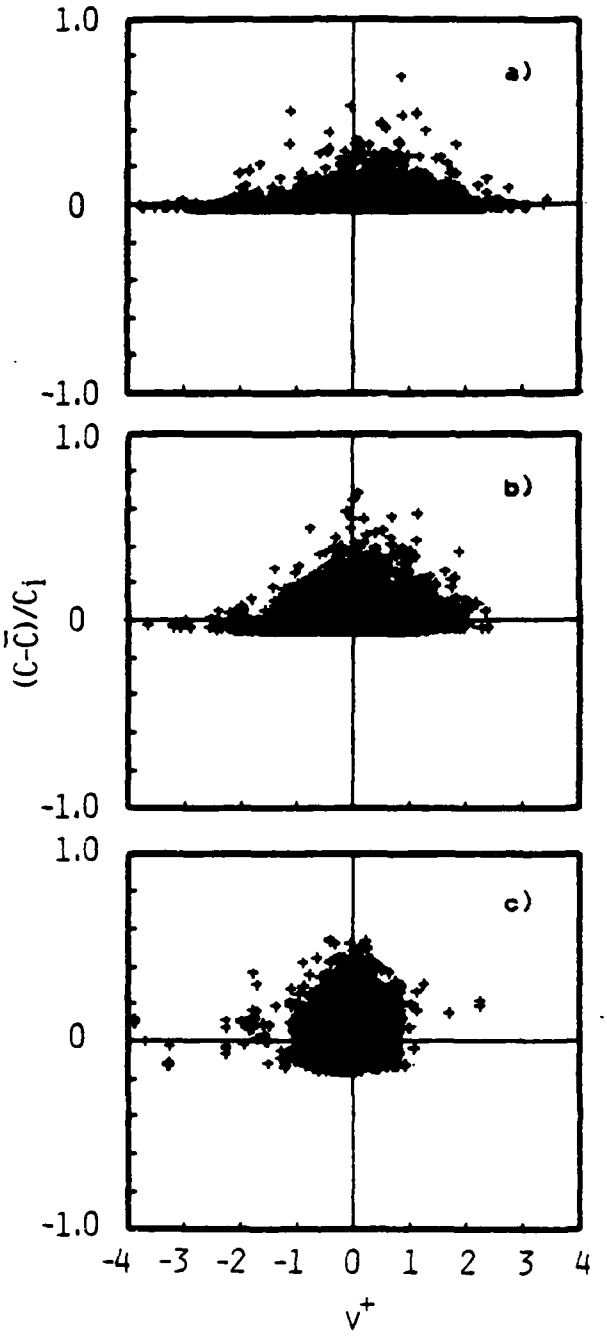

Figure 6.7 Velocity and concentration scatter diagrams for flow with polymer injection: x = 200 mm, a) $y^+ = 109.2$, b) $y^+ = 27.1$, c) $y^+ = 13.1$.

concentration fluctuations). At all locations the distributions appear more triangular in shape with large positive concentration fluctuations corresponding to small magnitude velocity fluctuations and large velocity fluctuations occurring only when the polymer concentration is near zero. This is further evidence that the polymer damps the normal velocity fluctuations and demonstrates a direct link between the presence of the polymers and a reduction in the normal velocity fluctuation.

Examination of F(v) (Figure 6.8) shows behavior very similar to that of the water injection case. One difference is apparent: the transport is concentrated at smaller velocities. This is due to the generally lower v' values present in the polymer injection case.

For comparison purposes, Figure 6.9 shows scatter diagrams for x = 25 mm with polymer injection at locations comparable to those shown in 6.5 for water injection. The values of $\overline{vc}$ at these locations are all small and less than zero. At the outer location the distribution is similar to that of the water flow, but the two inner locations exhibit the same damping of the normal velocity at high concentrations exhibited at x = 200 mm. These distributions have values of v' and c' comparable to those seen in the near-wall region of the water flow but the distributions are nearly symmetric about the v-axis resulting in the small values of $\overline{vc}$.

Plots of F(v) are shown in Figure 6.10 for these locations. At $y^+ = 32.4$, there are contributions from both positive and negative velocity fluctuations that result in net mass transport toward the wall. A contribution from positive velocity fluctuations to mass transport toward the wall is displayed at $y^+ = 27.2$ although $\overline{vc}$ is very small here

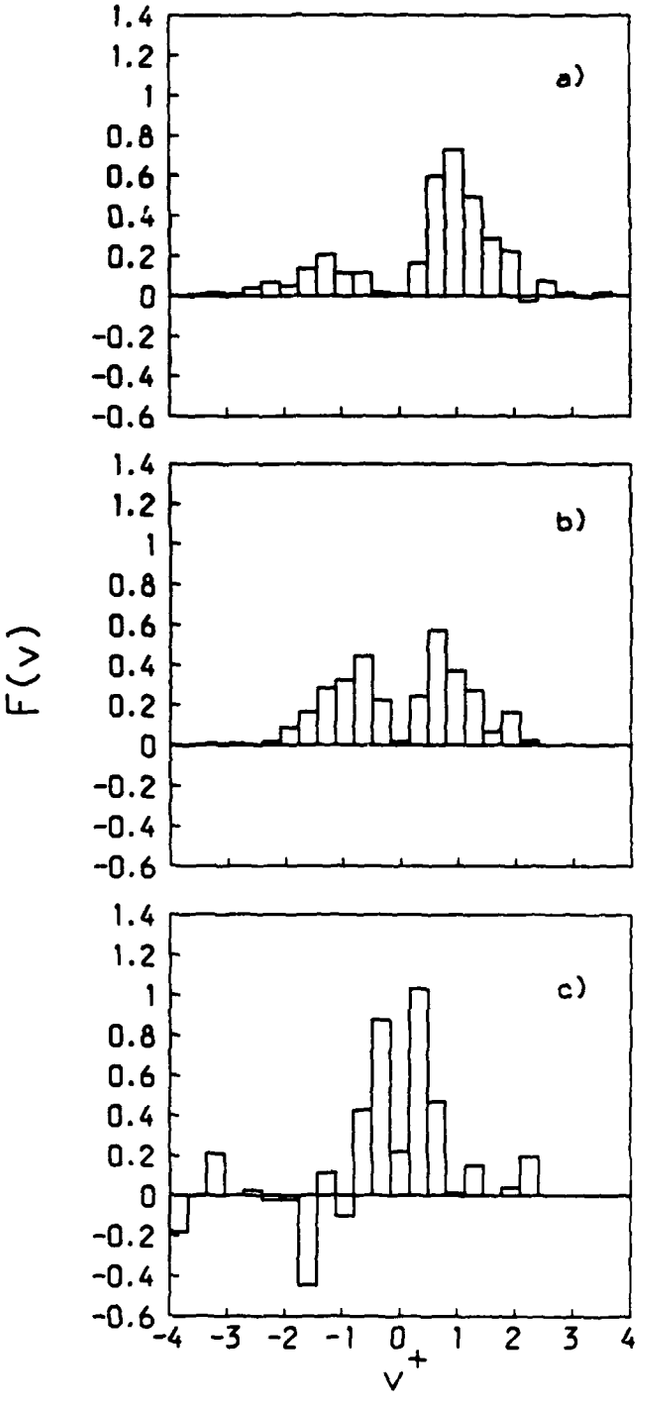

Figure 6.8 F(v) for flow with polymer injection: x = 200 mm, a) $y^+ = 109.2$, b) $y^+ = 27.1$, c) $y^+ = 13.1$.

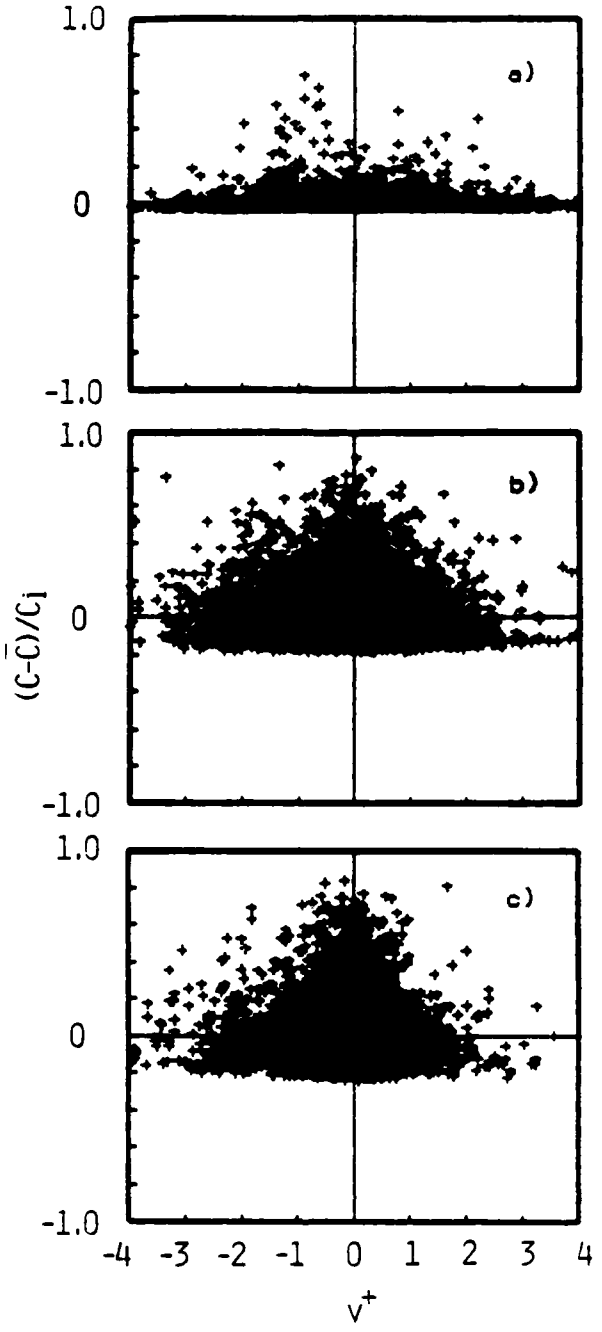

Figure 6.9 Velocity and concentration scatter diagrams for flow with polymer injection: x = 25 mm, a) $y^+ = 70.8$, b) $y^+ = 32.4$, c) $y^+ = 27.2$.

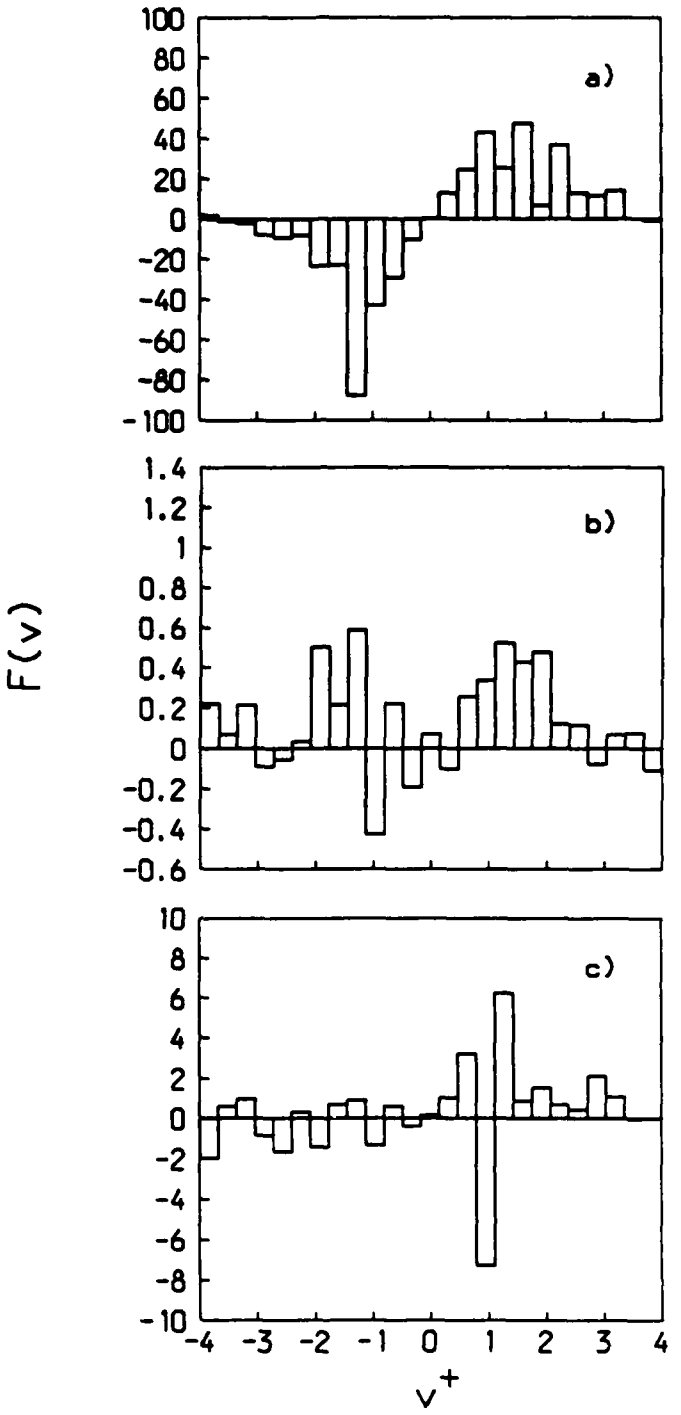

Figure 6.10 F(v) for flow with polymer injection: x = 25 mm, a) $y^+ = 70.8$, b) $y^+ = 32.4$, c) $y^+ = 27.2$.

and there is significant scatter in the results. The location at $y^+ = 70.8$ displays behavior that was not seen in the previous results: The contribution from positive velocity fluctuations is of opposite sign than that of the negative velocity fluctuations. This indicates that at this location (near the edge of the high-mean-concentration wall-region) high concentration fluid is as likely to be moving instantaneously toward the wall as away from the wall. This results in near zero net mass transport.

In the flow with water injection, for the y-location where the maximum turbulent mass transport occurs and for points nearer the wall, the positive and negative wall-normal-velocity fluctuations contribute equally to mass transport indicating that turbulent transport is about equally divided between high concentration fluid moving away from the wall and low concentration fluid approaching the wall. Further from the wall, mass transport is primarily due to positive velocity fluctuations carrying high-concentration fluid outward; negative velocities carry as much high-concentration fluid as low-concentration fluid inward toward the wall resulting in no net contribution to mass transport. This behavior is echoed at $x = 200$ mm for the polymer flow and is evidence that the transport process is similar for these two flows. At $x = 25$ mm in the flow with polymer injection, far from the wall, the contribution from positive velocities is balanced by a negative contribution from negative velocity fluctuations. Nearer the wall, positive velocity fluctuations contribute to the net transport but negative fluctuations as a group do not.

The previous paragraph concerns net transport. In the scatter diagrams shown in Figures 6.5, 6.7 and 6.9, the relative symmetry of the distributions about the c-axis

accounts for the low values of $\overline{vc}$ and R_{vc} in these flows. This is probably a high Schmidt number effect. If the Schmidt number is high (the mass diffusivity is small relative to viscosity), a fluid element with high concentration and low momentum which moves from the near wall region to the low-concentration outer flow retains its high concentration even after it has come to equilibrium with the momentum field in the outer flow. When this fluid element is carried back into the near-wall region (as it inevitably will be) it returns with the higher momentum of the outer flow but still retains the high concentration it had when it left the near-wall region. This scenario results in significantly less mass transport than momentum transport ocurring for the same turbulent motion and explains the degree of symmetry in the scatter diagrams. It also explains the negative contribution to mass transport from large negative velocities at locations near the wall.

6.3 Implications for modeling

The following paragraphs briefly examine the nature of the $\overline{vc}$ product and its relationship to momentum transport for the purpose of modeling this type of flow. Comparisons will be made between $x = 200$ mm for the flow with polymer injection and $x = 25$ mm for the flow with water injection. These two cases exhibited similar mean conctration profiles.

Figure 6.11 shows the ratio of turbulent mass and momentum transport ($\overline{vc}/\overline{uv}$) normalized with the injected concentration and the shear velocity of the water flow with no injection. The peak in this ratio for the polymer injection case is about twice that for water injection. The peak for water injection corresponds to the peak in $\overline{vc}$, while in the

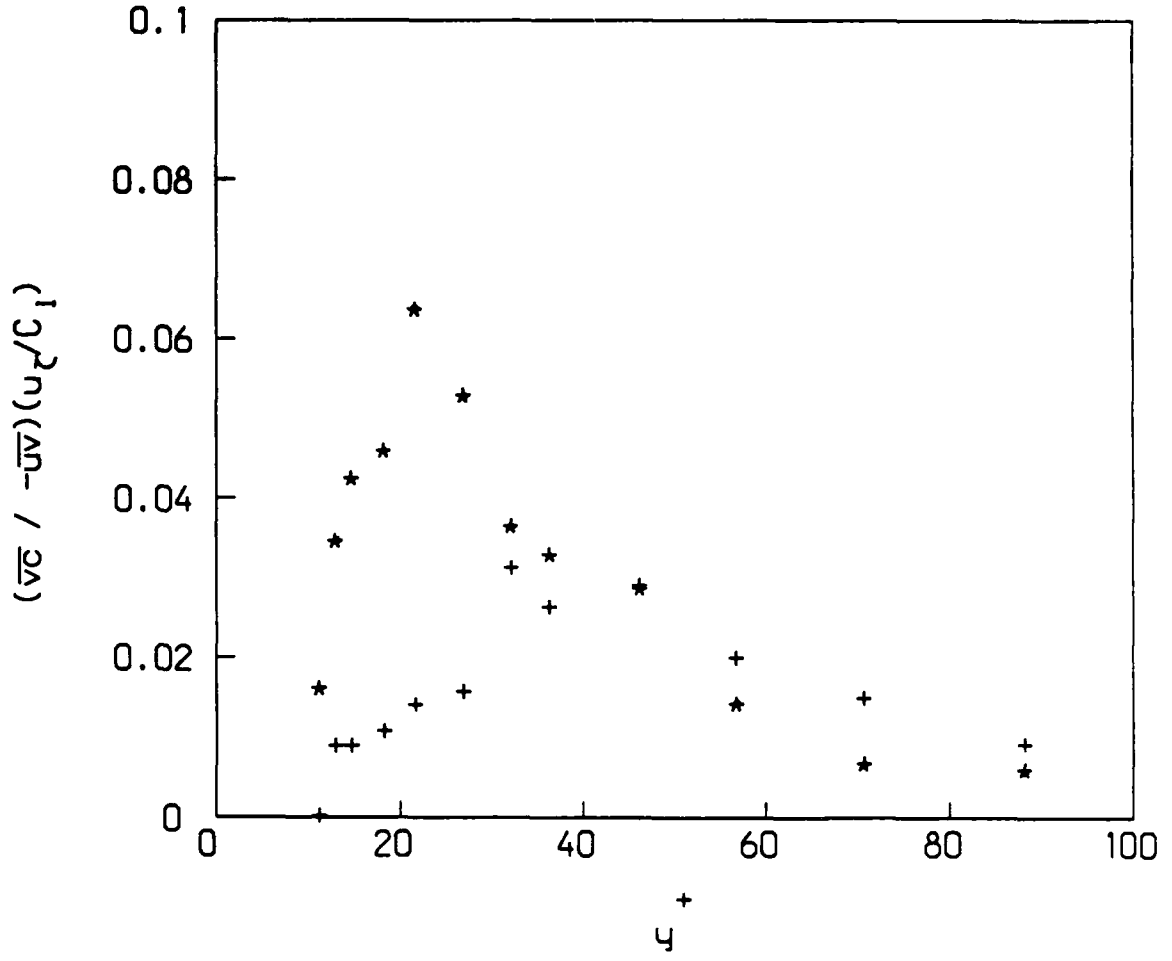

Figure 6.11 Ratio of turbulent mass transport to momentum transport: + , x = 25 mm with water injection; * , x = 200 mm with polymer injection.

polymer injection case the peak is nearer the wall than the peak in $\overline{vc}$. These results indicate that when the flow is modified the relationship between turbulent mass and momentum transport is altered, and that while the mass and momentum transport both decrease, the momentum transport is reduced more.

Turbulent diffusivities are defined as

$$\frac{\overline{vc}}{\partial \overline{C}/\partial y}$$

for mass transport, and

$$\frac{\overline{uv}}{\partial \overline{U}/\partial y}$$

for momentum transport. Profiles of turbulent mass and momentum diffusivities are shown in Figure 6.12 normalized with the kinematic viscosity of the water flow. The results presented are for x = 25 mm with water injection, and 200 mm for the flow with polymer injection. These data show that the mass-transport diffusivities are very similar for the two flows. The momentum-transport diffusivities, however, exhibit marked differences. The values for the polymer flow are significantly less than those for the water flow. This is further evidence of the difference in the effect of the presence of the polymer solution on the mass and momentum transport processes.

Turbulent Schmidt numbers are shown in Figure 6.13 for both flows. This quantity is defined as:

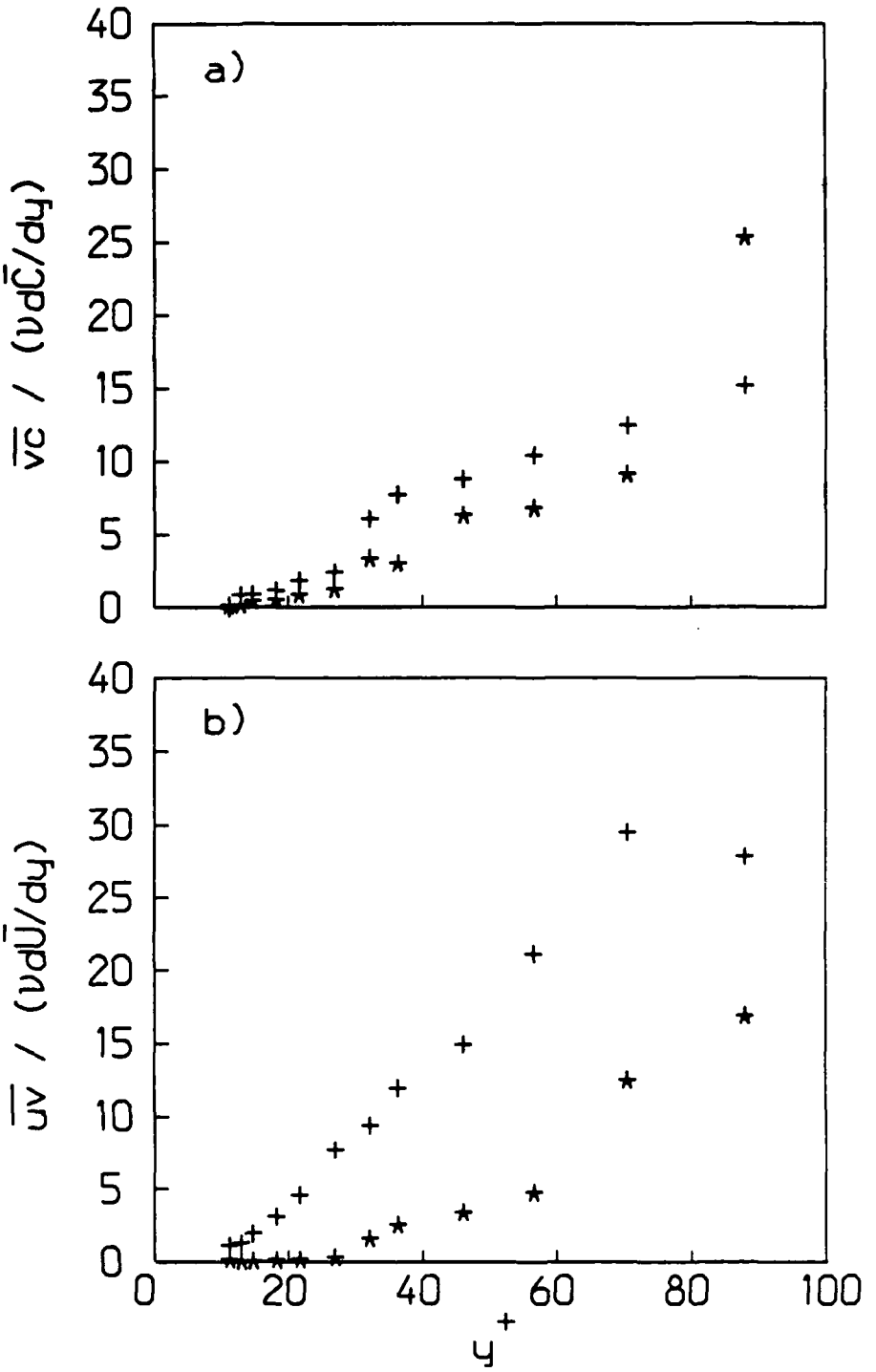

Figure 6.12 Turbulent diffusivities for a) mass transport, b) momentum transport: + , x = 25 mm with water injection; * , x = 200 mm with polymer injection.

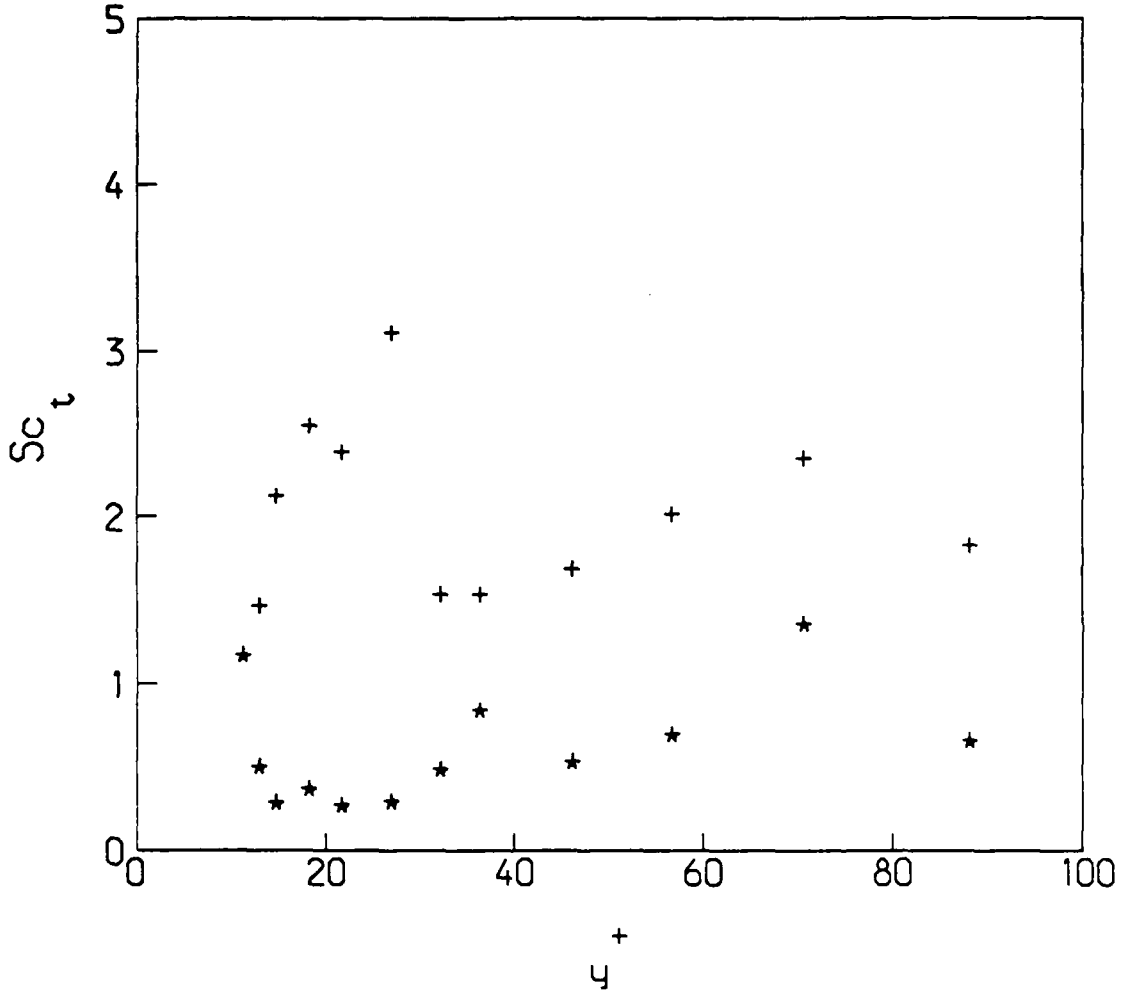

Figure 6.13 Turbulent Schmidt number profiles: + , x = 25 mm with water injection; ★ , x = 200 mm with polymer injection.

$$Sc_t = \frac{\overline{uv}/\left[\partial\overline{U}/\partial y\right]}{\overline{vc}/\left[\partial\overline{C}/\partial y\right]}.$$

Surprisingly, the flow with water injection has a higher value of Sc_t than the flow with polymer injection. The high values of Sc_t exhibited by the water injection case ($Sc_t \geq 1.5$) imply that the accepted values of $0.7 - 1.0$ are inapproporiate for the high molecular Schmidt number regime. The low values exhibited by the polymer injection case are further evidence of the complex relationship between mass and momentum transport in this flow.

CHAPTER 7 - SUMMARY AND CONCLUSIONS

This study examined a fully developed turbulent channel flow with polymer injection at the wall and had two complimentary objectives. The first objective was to gain more understanding of the way in which long-chain, high molecular weight, water soluble polymers cause viscous drag reduction in turbulent wall flows. The second was to acquire information useful in the modeling of the transport processes in flows with polymer injection at the wall, particularly the high Schmidt number mixing process which occurs. A fluorescence technique was developed for time-resolved measurements of species concentration profiles. This technique was combined with laser velocimetry to obtain measurements of turbulent mass transport $\overline{vc}$ in a flow with polymer injection and, for comparison purposes, a flow with water injection. Two-component laser velocimeter measurements were made in both flows to examine the effect of both the injection process and the evolving polymer concentration field on the structure of turbulence.

Two-component velocity measurements were used to examine the turbulence structure in the basic water flow. This yielded results which were consistent with those in the literature for fully developed, two-dimensional turbulent channel flow. A method was presented which used these velocity measurements to determine the wall shear velocity to high accuracy (±3 percent).

Time-resolved concentration profiles measured during polymer injection showed that there is very little movement of high concentration fluid away from the wall for $x < 100$ mm. This was indicative of the absence of mass transport at these locations and was confirmed by the behavior of the mean concentration profiles and direct measurements of turbulent mass tansport. For $x > 100$ mm, there were periods of activity interspersed with somewhat longer quiescent periods. During these active periods, long (in the streamwise direction) filaments of high-concentration fluid moved away from the wall; this is the dominant transport mechanism in the near-wall region. Compared to the water flow, these periods of activity had a significantly reduced frequency in the polymer flow.

Examination of the probability density functions for concentration showed that the concentration distributions are highly skewed toward low concentrations, except very near the wall. They also revealed that, during the mixing of the polymer solution with the flow, at no time does pure water penetrate to the wall. This indicates that very near the wall, the transport process for mass (and presumably other quantities) is dominated by molecular diffusion and, at most, small-scale turbulent mixing.

A detailed examination of the turbulence structure showed that in the flow with polymer injection, the RMS streamwise velocity levels are increased by about 15 percent at all streamwise locations. Initially, the injection process causes elevated levels of the RMS of the wall-normal velocity and the turbulent shear stress. However, damping action by the polymer solution subsequently reduced these quantities significantly below the levels present in the water flow for $x > 25$ mm. Scatter diagrams for wall-

normal velocity and concentration showed that, instantaneously, the presence of high polymer concentrations resulted in small velocity fluctuations, establishing a direct link between the presence of the polymer solution and reduced v' values. The decreased $-\overline{uv}$ levels result from both the decrease in v' and a decrease in the degree of correlation between the u and v velocity fluctuations.

An examination of Reynolds stress production showed that the polymer solution reduced the production rate for $\overline{u^2}$ and that the production of $\overline{uv}$ was not changed. The reduced levels of v' and $\overline{uv}$ along with the increase in u' caused by the polymer indicates that the polymer may alter the pressure-strain correlations. These correlations transfer energy from $\overline{u^2}$ to $\overline{v^2}$ and are also the principal source of $\overline{uv}$ destruction. Assuming that the Reynolds stress transport equations are not significantly altered for the polymer solution, it is concluded that the polymer solution inhibits the redistribution from u' to v' and causes increased destruction of $\overline{uv}$.

In general $\overline{vc}$ levels were lower in the polymer injection flow than in the water flow. This results in the polymer requiring a longer streamwise distance to mix completely into the flow than dyed water. The correlation coefficient for mass transport was lower than that for momentum transport; this is attributed to the high Schmidt number associated with the mass transport process. The low molecular mass diffusivity (relative to viscosity) results in high concentration fluid mixing from the wall to the outer flow and back to the wall yielding low levels of net turbulent mass transport relative to the magnitude of the velocity and concentration fluctuations.

At x=200 mm in the polymer flow, $\overline{vc}$ was less than it was at 25 mm with water injection but the mean concentration profiles and the degree of correlation were similar in both cases. This indicates that the reduced transport was the result of smaller velocity and concentration fluctuations and not differences in the transport process. The contributions to mass transport from the wall-normal velocity fluctuations were similar in these two situations. A brief examination of modeling issues confirmed these results: Profiles of the turbulent diffusivities for mass agreed for these two locations. However, the momentum transport was significantly reduced in the polymer flow causing the turbulent Schmidt number profiles to be different in these flows. For these high molecular Schmidt number flows, the turbulent Schmidt numbers deviated significantly from unity.

From the results of this study, the evolution of this flow from a Newtonian state upstream of the injector to a drag-reduced flow can be described. Immediately downstream of the injector, the injected polymer layer is stretched and distorted by the water flow above it. The larger shear viscosity of the polymer solution causes the flow near the wall to be slower than in the water flow with no injection. This blockage of the flow causes an increase in the velocity gradient at the edge of the high concentration layer. This along with the disturbance to the flow from the injection process causes increased Reynolds stress production resulting in elevated levels of v' and $\overline{uv}$. Since movement of high-concentration fluid from near the wall to the outer flow requires acceleration in the direction of fluid movement (i.e. an elongational strain) the high extensional viscosity of the polymer solution prevents it from being carried into the outer flow. (This is confirmed by the strong correlation between high polymer

concentrations and small wall-normal velocities.)

As the flow proceeds downstream, the concentrations near the wall are reduced and become more homogeneous as a result of small scale mixing within the near-wall layer. There is still no transport of high concentration fluid from the wall but the effects of the injection process begin to diminish as v' and $\overline{uv}$ levels return to those of the water flow with no injection. This shows that above the high-concentration layer the flow is still Newtonian in nature.

As the concentration in the near-wall region is reduced, the extensional viscosity is reduced and high-concentration fluid begins to move away from the wall in the form of long filaments. Due to the low molecular mass diffusivity of the polymer solution, this high concentration fluid is mixed back into the near-wall region resulting in small net mass transport relative to the size of the velocity and concentration fluctuations. The high extensional viscosity of the polymer solution causes these polymer filaments to resist acceleration and inhibits the transfer of energy from u' to v'. This resistance to acceleration increases the local instantaneous shear-strains which causes increased destruction of $\overline{uv}$ through the pressure-shear-strain correlation. It also allows this fluid to return to the near-wall region with a smaller than expected increase in momentum resulting in decreased net momentum transport. This decrease in turbulent transport results in reduced viscous drag.

REFERENCES

Antonia, R.A., H.Q. Danh and A. Prabhu 1977 Response of a turbulent boundary layer to a step change in heat flux. *J. Fluid Mech.* **80**, 153.

Argumedo, A., T.T. Tung and K.I. Chang 1978 Rheological property measurements of drag-reducing polyacrylamide solutions. *J. Rheology* **22**, 449.

Berner, C. and O. Scrivener 1980 Drag reduction and turbulence in dilute polymer solutions. In: *Viscous Flow Drag Reduction*, G.R. Hough, ed., AIAA, 290.

Bewersdorff, H.W. 1984 Effect of a centrally injected polymer thread on turbulent properties in pipe flows. In: *Drag Reduction*, R.J.H. Sellin and R.T. Moses, eds., Univ. of Bristol, B4.

Bradshaw, P. 1978 *Topics in Applied Physics Volume 12: Turbulence*. Springer-Verlag, 25.

Cho, Y.I., J.P. Hartnett and Y.S. Park 1983 Solvent effects on the rheology of aqueous polyacrylamide solutions. *Chem. Eng. Commun.* **21**, 369.

Collins, D.J. and C.W. Gorton 1976 An experimental study of diffusion from a line source in a turbulent boundary layer. *AIChE J.* **22**, 610.

Edwards, R.V. 1987 Report of the special panel on statistical bias problems in laser anemometry. *J. Fluids Engng* **109**, 89.

Fabula, A.G. and T.J. Burns 1970 Dilution in a turbulent boundary layer with polymeric friction reduction. *NUC Technical Publication No. 171.*

Finnicum, D.S. and T.J. Hanratty 1985 Turbulent normal-velocity fluctuations close to a wall. *Phys. Fluids* **28**, 1654.

Frings, B. 1984 Annular injection of concentrated polymer solutions into the wall region of turbulent pipe flow. In:*The Influence of Polymer Additives on Velocity and Temperature Fields*, B. Gampert, ed., Springer-Verlag, 349.

Gould, R.D., W.H. Stevenson and H.D. Thompson 1988 A parametric study of statistical bias in laser Doppler velocimetry. *AIAA J.*, in press.

Hanratty, T.J., L.G. Chorn and D.T. Hatziavramidis 1977 Turbulent fluctuations in the viscous wall region for Newtonian and drag reducing fluids. *Phys. Fluids* **20**, S112.

Hartnett, J.P. 1985 Mass transfer cooling. In: *Handbook of Heat Transfer Applications*, W.M. Rohsenow, J.P. Hartnett and E.N. Ganic, eds., McGraw-Hill, 1-51.

Hishida, M., Y. Nagano and M. Tagawa 1986 Transport processes of heat and momentum in the wall region of turbulent pipe flow. In: *Procedings of the Eighth International Heat Transfer Conference Vol. 3*, Hemisphere, 925.

Hoyt, J.W. 1984 Some highlights in the field of polymer drag reduction. In: *Drag Reduction*, R.J.H. Sellin and R.T. Moses, eds., Univ. of Bristol, I.1-1.

Hussain, A.K.M.F. and W.C. Reynolds 1975 Measurements in fully developed turbulent channel flow. *J. Fluids Engng* **97**, 568.

Karpuk, M.E. and W.G. Tiederman 1976 Effect of finite-size probe volume upon laser-Doppler anemometry measurements. *AIAA J.* **14**, 1099.

Kim J., P. Moin and R. Moser 1987 Turbulence statistics in fully developed channel flow at low Reynolds number. *J. Fluid Mech.* **177**, 133.

Koochesfahani, M.M. and P.E. Dimotakis 1986 Mixing and chemical reactions in a turbulent mixing layer. *J. Fluid Mech.* **170**, 83.

Kreplin, H. and H. Eckelmann 1979 Behavior of the three fluctuating velocity components in the wall region of a turbulent channel flow. *Phys. Fluids* **22**, 1233.

Latto, B. and O.K.F. El Reidy 1976 Diffusion of polymer additives in a developing turbulent boundary layer. *J. Hydronautics* **10**, 135.

Latto, B. and O.K.F. El Reidy and J. Vlachopoulos 1981 Effect of sampling rate on concentration measurements in nonhomogeneous dilute polymer solution flow. *J. Rheology* **25**, 583.

Latto, B. and O.K.F. El Reidy 1984 Dispersion of polymer additives in a developing turbulent boundary layer. In: *Drag Reduction*, R.J.H. Sellin and R.T. Moses, eds., Univ. of Bristol, B6.

Logan, S.E. 1972 Laser velocimeter measurements of Reynolds stress and turbulence in dilute polymer solutions. *AIAA J.* **7**, 962.

Luchik, T.S. 1985 *The effect of drag reducing additives on turbulent structure in channel flow*. Ph.D. Thesis, Purdue University.

Luchik, T.S. and W.G. Tiederman 1986 Effect of spanwise probe volume length on laser velocimeter measurements in wall bounded turbulent flows. *Exp. in Fluids* **3**, 339.

Luchik, T.S. and W.G. Tiederman 1987 Timescale and structure of ejections and bursts in turbulent channel flows. *J. Fluid Mech.* **174**, 529.

Luchik, T.S. and W.G. Tiederman 1988 Turbulent structure in low concentration drag-reducing channel flows. *J. Fluid Mech.* **190**, 241.

Mansour, N.N., J. Kim and P. Moin 1988 Reynolds-stress and dissipation-rate budgets in a turbulent channel flow. *J. Fluid Mech.* **194**, 15.

McComb, W.D. and L.H. Rabie 1982 Local drag reduction due to injection of polymer solutions into turbulent flow in a pipe. Part I: Dependence on local polymer concentration; Part II: Laser-Doppler measurements of turbulent structure. *AICHE J.* **28**, 547.

McLaughlin, D.K. and W.G. Tiederman 1973 Biasing correction for individual realization of laser velocimeter measurements in turbulent flows. *Phys. Fluids* **16**, 2082.

Moin, P. and J. Kim 1982 Numerical investigation of turbulent channel flow. *J. Fluid Mech.* **118**, 341.

Moser, R.D. and P. Moin 1987 The effects of curvature in wall bounded turbulent flows. *J. Fluid Mech.* **175**, 479.

Nagano, Y. and M. Hishida 1985 Production and dissipation of turbulent velocity and temperature fluctuations in fully developed pipe flow. In: *Procedings of the Fifth International Symposium on Turbulent Shear Flows*, Cornell University, 14.19.

Reischman, M.M. and W.G. Tiederman 1975 Laser Doppler anemometer measurements in drag-reducing channel flows. *J. Fluid Mech.* **70**, 369.

Rudd, M.J. 1972 Velocity measurements made with the laser Dopplermeter in turbulent pipe flow of a dilute polymer solution. *J. Fluid Mech.* **51**, 673.

Ryskin, G. 1987 Calculation of the effects of a polymer additive on converging flow. *J. Fluid Mech.* **178**, 423.

Spalart, P. 1988 Direct simulation of a turbulent boundary layer up to $R_\theta = 1410$. *J. Fluid Mech.* **187**, 61.

Tiederman, W.G., T.S. Luchik and D.G. Bogard 1985 Wall layer structure and drag reduction. *J. Fluid Mech.* **156**, 419.

Tsai, C.F. and R. Darby 1978 Nonlinear viscoelastic properties of very dilute drag-reducing polymer solutions. *J. Rheology* **22**, 219.

Walker, D.A. 1986 A fluorescence technique for measurement of concentration in mixing liquids. *J. Phys. E. Sci. Instrum.* **20**, 217.

Walker, D.T. and W.G. Tiederman 1987 Near-field effects of polymer wall injection on turbulent channel flow. In: *Procedings of the Twentieth Midwest Mechanics Conference Vol. 14a*, W. Sodel and J.F. Hamilton, eds., Purdue University, 76.

Walker, D.T., W.G. Tiederman and T.S. Luchik 1986 Optimization of the injection process for drag reducing additives. *Exp. in Fluids* **4**, 114.

Wei, T. 1987 *Reynolds number effects on the small scale structure of a turbulent channel flow*. Ph.D. Dissertation, University of Michigan.

Wells, C.S. and J. G. Spangler 1967 Injection of drag-reducing fluid into a turbulent pipe flow of a Newtonian fluid. *Phys. Fluids* **10**, 1890.

Willmarth, W.W., T. Wei, and C.O. Lee 1987 Laser anemometer measurements of Reynolds stress in a turbulent channel flow with drag reducing polymer additives. *Phys. Fluids* **30**, 933.

Yanta, W.J. and R.J. Smith 1973 Measurements of turbulence transport properties with a laser Doppler velocimeter. *AIAA Paper No. 73-169*.

Appendix A: Calculation of Rotated Statistics

The ability to calculate second statistical moments in a coordinate system which is rotated relative to the coordinate system in which the measurements were obtained simplifies processing of two-component velocity measurements. Statistics can be calculated on the measured velocity components and then these results can be used to calculate the desired statistics. This eliminates the computational expense of resolving the individual velocity measurements into the desired components prior to calculating the statistics. It also allows one to change the coordinate system and determine the appropriate statistics without re-analyzing the original velocity data.

We desire to calculate statistics in the x-y coordinate system (U and V velocity components) using statistics for U_1 and U_2 which were measured in the x_1-x_2 coordinate system which is rotated a some angle θ. (See Figure A.1.) The relationship between U and V and U_1 and U_2 is expressed as

$$U = U_2\cos\theta + U_1\sin\theta \tag{A.1}$$

$$V = U_2\sin\theta - U_1\cos\theta. \tag{A.2}$$

Time-averaging Equations A.1 and A.2 yields

$$\overline{U} = \overline{U}_2\cos\theta + \overline{U}_1\sin\theta \tag{A.3}$$

$$\overline{V} = \overline{U}_2\sin\theta - \overline{U}_1\cos\theta. \tag{A.4}$$

Subtracting the equations for the mean velocities from those for the instantaneous velocities results in equations for the fluctuating velocities u and v in terms of u_1 and u_2. These equations are

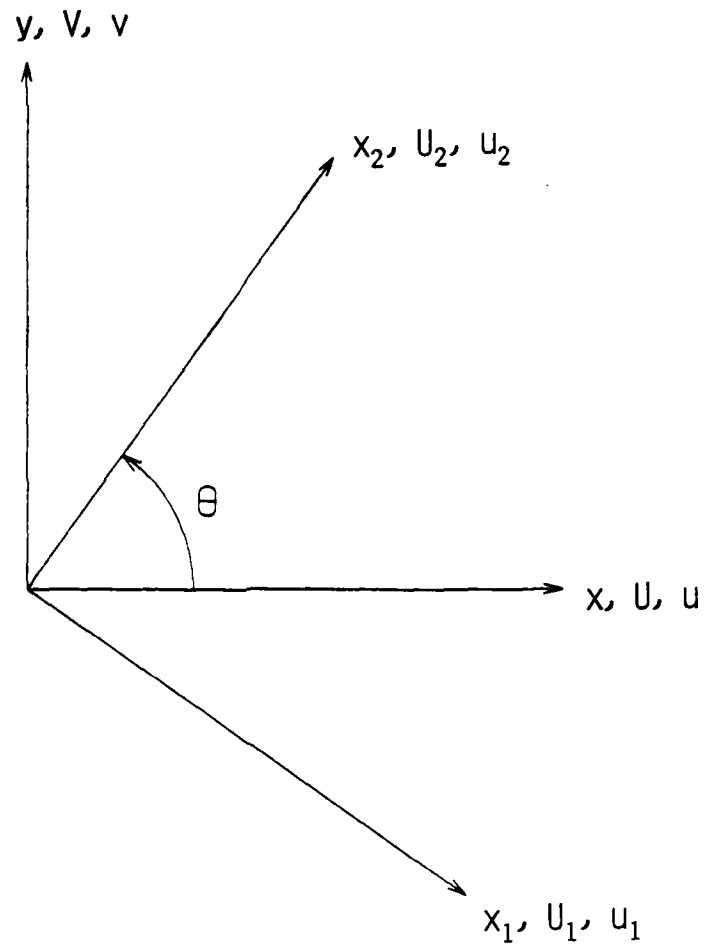

Figure A.1 Coordinate system for rotation of velocity statistics

$$u = u_2\cos\theta + u_1\sin\theta \tag{A.5}$$

$$v = u_2\sin\theta - u_1\cos\theta. \tag{A.6}$$

Squaring Equation A.5 and time-averaging results in an equation for $\overline{u^2}$:

$$\overline{u^2} = \overline{u_1^2}\sin^2\theta + \overline{u_2^2}\cos^2\theta + 2\overline{u_1 u_2}\cos\theta\sin\theta \tag{A.7}$$

Performing similar operations on Equation A.6 yields an equation for $\overline{v^2}$:

$$\overline{v^2} = \overline{u_1^2}\cos^2\theta + \overline{u_2^2}\sin^2\theta - 2\overline{u_1 u_2}\cos\theta\sin\theta \tag{A.8}$$

Multiplying Equations A.5 and A.6 and time-averaging yields the following equation for $\overline{uv}$.

$$\overline{uv} = \left[\overline{u_2^2} - \overline{u_1^2}\right]\sin\theta\cos\theta + \overline{u_1 u_2}\left[\sin^2\theta - \cos^2\theta\right] \tag{A.7}$$

These equations were used to calculate statistical moments in the desired coordinate system for the results presented.

Appendix B: Uncertainty Analysis

When examining profiles of turbulence statistics and the evolution of such profiles in the direction of flow, there are several distinct sources of uncertainty to be considered. Absolute errors in location, as well as errors in the position of one point relative to another are important. In the estimation of turbulence statistics one must consider both fixed and random errors in the individual realizations used to calculate a statistic and the inherent uncertainty in estimating a statistic with a finite-size ensemble. This section is an attempt to evaluate the impact of these uncertainties on the results to be presented.

Two separate traversing mechanisms were used to move the laser velocimeter measurement volume in space. The vertical (y-direction) motion was controlled by a micrometer having a least count of 0.013 mm the streamwise (x-direction) location was determined using a scale with a least count of 0.5 mm. This results in probable errors in the relative locations of two points in space of 0.38 wall units in the y-direction and 14 wall units in the streamwise direction. The absolute location of the wall was determined using the laser velocimeter measurement volume resulting in a estimated uncertainty of 0.9 wall units (one-half the y-extent of the measurement volume)

Uncertainty in statistical quantities can be separated into two distinct quantities: the probable error in the individual realizations used to calculate the statistics, and the uncertainties associated with estimating a statistic using a finite-size ensemble. After considering each of these in turn, this section closes with the discussion of the combined effect of both types of uncertainty.

The results of this study are derived primarily from two-component laser velocimeter data, one-component laser velocimeter data and concentration data acquired using the laser-induced-fluorescence technique. For the laser velocimeter data, the primary source of error is the uncertainty in the determination of the beam-crossing angle which affects the calculation of the fringe spacing This results in an uncertainty of 0.4 percent for the measured velocity component. (Since the statistics are calculated for a rotated coordinate system where $\overline{V} = 0$, the uncertainty for U and for V is about 0.004U.) The dominant uncertainty in the concentration measurements results from the pH dependence of the fluorescence of the dye used and the uncertainty in matching the pH of the channel water to that of the injected polymer solution (0.5 percent of the measured concentration).

These errors can be propagated to the statistics calculated from the acquired data. Experimental uncertainties (ε's) for the mean velocities (in the x-y coordinate system) are

$$\varepsilon_{\overline{U}}, \varepsilon_{\overline{V}} \approx 0.004\, \overline{U}; \tag{B.1}$$

experimental uncertainty for the mean concentration is

$$\varepsilon_{\overline{C}} \approx 0.005\, \overline{C}. \tag{B.2}$$

For the RMS quantities, the experimental uncertainties are

$$\varepsilon_{u'} \approx 0.004\, u' \tag{B.3}$$

$$\varepsilon_{v'} \approx 0.004\, \frac{\overline{uv}}{v'} \tag{B.4}$$

$$\varepsilon_{c'} \approx 0.005\, c' \tag{B.5}$$

For the remaining second moments, $\overline{uv}$ and $\overline{vc}$:

$$\varepsilon_{\overline{uv}} \approx 0.004 \left[\overline{u^2} + \overline{uv} \right] \tag{B.6}$$

$$\varepsilon_{\overline{vc}} \approx 0.006\, \overline{vc}\,. \tag{B.7}$$

The relatively complex form of the uncertainties for $\overline{uv}$ and v' results from measuring the velocities at ±45° to the desired components.

Appropriate normalization of these uncertainties yields :

$$\frac{\varepsilon_{\overline{U}}}{\overline{U}}, \frac{\varepsilon_{\overline{V}}}{\overline{U}} \approx 0.004\,, \tag{B.8}$$

$$\frac{\varepsilon_{\overline{C}}}{\overline{C}} \approx 0.005\,, \tag{B.9}$$

$$\frac{\varepsilon_{u'}}{u'} \approx 0.004\,, \tag{B.10}$$

$$\frac{\varepsilon_{v'}}{v'} \approx 0.004\, \frac{\overline{uv}}{v'^2}\,, \tag{B.11}$$

$$\frac{\varepsilon_{c'}}{c'} \approx 0.005\,, \tag{B.12}$$

$$\frac{\varepsilon_{\overline{uv}}}{\overline{uv}} \approx 0.004 \left[1 + \frac{u'^2}{\overline{uv}} \right], \tag{B.13}$$

and

$$\frac{\varepsilon_{\overline{vc}}}{\overline{vc}} \approx 0.006 . \tag{B.14}$$

The estimation of any statistic from a finite-size ensemble of individual realizations has an inherent uncertainty which is defined by the type of statistic and the size of the ensemble used in its calculation. The standard deviation of the estimated mean is

$$\sigma_{\overline{U}} = \frac{1}{\sqrt{N}} \sigma_U . \tag{B.15}$$

If one assumes that the distribution for a given quantity is Gaussian or nearly so, the uncertainty at the 95 percent confidence level resulting from the estimation of the statistic from a finite size ensemble (δ) is

$$\frac{\delta_{\overline{U}}}{\overline{U}} = \frac{2}{\sqrt{N}} \frac{u'}{\overline{U}} . \tag{B.16}$$

This indicates, as was shown by Yanta and Smith (1973), that the uncertainty in the estimated mean depends on both the ensemble size and the RMS level.

Similar uncertainties can be calculated for the second moments. For large sample sizes, the standard deviation of the standard deviation is given by

$$\sigma_{u'} = \frac{1}{\sqrt{2N}} \sigma_U . \tag{B.17}$$

When estimating the uncertainty for products such as $\overline{uv}$, if we assume the two quantities are independent then

$$\sigma_{\overline{uv}} = \sqrt{\frac{2}{N}}\,\sigma_U \sigma_V \,. \tag{B.18}$$

The uncertainties for u´ and $\overline{uv}$ are therefore given by

$$\frac{\delta_{u'}}{u'} = \frac{2}{\sqrt{2N}}\,, \tag{B.19}$$

and

$$\frac{\delta_{\overline{uv}}}{\overline{uv}} = 2\sqrt{\frac{2}{N}}\,\frac{u'v'}{\overline{uv}} = \frac{2}{R}\sqrt{\frac{2}{N}} \tag{B.20}$$

where R is the correlation coefficient for u and v. This shows that the uncertainty in the estimate of an RMS quantity depends solely on the ensemble size (Yanta and Smith, 1973), but the uncertainty in quantities like $\overline{uv}$ depend upon both the ensemble size and the degree of correlation.

Figure B.1 shows the variation of this type of uncertainty with ensemble size and the relevant parameters for mean, RMS and $\overline{uv}$-type statistics.

The total uncertainty in a given statistic is then the root-sum-square of the uncertainties arising from both sources

$$\upsilon = \sqrt{\delta^2+\varepsilon^2}\,. \tag{B.21}$$

For the mean quantities:

$$\frac{\upsilon_{\overline{U}}}{\overline{U}} \approx \left[(0.004)^2 + \frac{1}{N}\left[\frac{u'}{\overline{U}}\right]^2\right]^{1/2}, \tag{B.22}$$

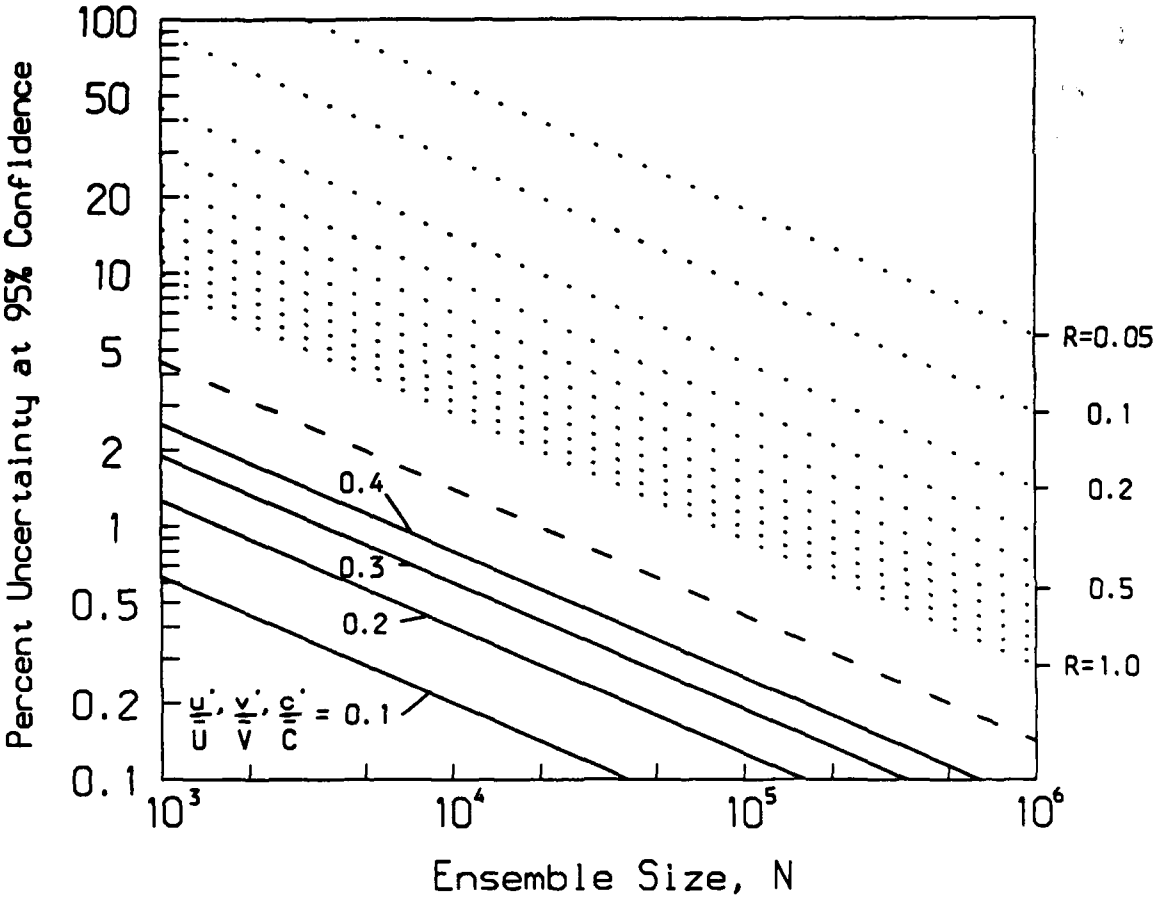

Figure B.1 Uncertainty in estimated statistics due to finite ensemble size. ——— : $\overline{U}$, $\overline{V}$, $\overline{C}$; – – – – : u′, v′, c′; - - - - - : $\overline{uv}$, $\overline{vc}$.

$$\frac{\upsilon_{\overline{V}}}{\overline{U}} \approx \left[(0.004)^2 + \frac{1}{N} \left[\frac{v'}{\overline{U}} \right]^2 \right]^{½}, \tag{B.23}$$

and

$$\frac{\upsilon_{\overline{C}}}{\overline{C}} \approx \left[(0.005)^2 + \frac{1}{N} \left[\frac{c'}{\overline{C}} \right]^2 \right]^{½}. \tag{B.24}$$

For the second moments:

$$\frac{\upsilon_{u'}}{u'} \approx \left[(0.004)^2 + \frac{1}{2N} \right]^{½}, \tag{B.25}$$

$$\frac{\upsilon_{v'}}{v'} \approx \left[(0.004)^2 \left[\frac{\overline{uv}}{v'^2} \right]^2 + \frac{1}{2N} \right]^{½}, \tag{B.26}$$

$$\frac{\upsilon_{c'}}{c'} \approx \left[(0.005)^2 + \frac{1}{2N} \right]^{½}, \tag{B.27}$$

$$\frac{\upsilon_{\overline{uv}}}{\overline{uv}} \approx \left[(0.004)^2 \left[1 + \frac{u'^2}{\overline{uv}} \right]^2 + \frac{2}{N} \left[\frac{2}{R} \right]^2 \right]^{½}, \tag{B.28}$$

and

$$\frac{\varepsilon_{\overline{vc}}}{\overline{vc}} \approx \left[(0.006)^2 + \frac{2}{N} \left[\frac{2}{R} \right]^2 \right]^{½}. \tag{B.29}$$

These equations were used to estimate uncertainty at the 95 percent confidence level for the experimental data. For mean and root-mean-square statistics, the uncertainty estimate is generally comparable to the size of the plotting symbol used.

For $\overline{uv}$ and $\overline{vc}$, the uncertainty estimates are indicated by error bands on a few representative points.

DISTRIBUTION LIST

Dr. Michael M. Reischman, Code 1132F
Office of Naval Research
800 North Quincy Street
Arlington, VA 22217

Office of Naval Research
Resident Representative
536 S. Clark Street, Rm. 286
Chicago, IL 60605-1588

Director
Naval Research Laboratory
Attn: Code 2627
Washington, DC 20375
(6 copies)

Professor D.G. Bogard
Department of Mechanical Engineering
The University of Texas
Austin, TX 78712

Dr. Steve Deutsche
ARL
Pennsylvania State University
P.O. Box 30
State College, PA 16801

James H. Green, Code 634
Naval Ocean System Center
San Diego, CA 92152

Professor T.J. Hanratty
Department of Chemical Engineering
1209 West California Street
Box C-3
Urbana, IL 61801

Dr. R.J. Hansen, Code 1215
Office of Naval Research
800 North Quincy Street
Arlington, VA 22217

Defense Technical Information Center
Building 5, Cameron Station
Alexandria, VA 22314
(12 copies)

Mechanical Engineering Business Office
Purdue University
West Lafayette, IN 47907

Dr. O. Kim, Code 6124
Naval Research Laboratory
Washington, DC 20375

Professor S.J. Kline
Thermosciences Division
Department of Mechanical Engineering
Stanford University
Stanford, CA 94305

G. Leal
Department of Chemistry and
Chemical Engineering
California Institute of Technology
Pasadena, CA 91125

Justin H. McCarthy
Code 1540
David Taylor Naval Ship R&D Center
Bethesda, MD 20084

Professor E.W. Merrill
Department of Chemical Engineering
Massachusetts Institute of Technology
Cambridge, MA 02139

E.W. Hendricks, Code 4420
Naval Research Laboratory
Washington, DC 20375

Dr. J.H. Haritonidis
Room 37-461
Massachusetts Institute of Technology
Cambridge, MA 02139

Dr. D.L. Hunston
Polymer Sciences & Standards Division
National Bureau of Standards
Washington, DC 20234

Mr. G.W. Jones
Code 55W3
Naval Sea Systems Command
Washington, DC 20362

Dr. John Kim
M.S. 202A-1
NASA - Ames Research Center
Moffett Field, CA 94035

Dr. C.L. Merkle
Department of Mechanical Engineering
Pennsylvania State University
State College, PA 16801

Dr. T.E. Pierce
Code 63R31
Naval Sea Systems Command
Washington, DC 20362

Steve Robinson
M.S. 229-1
NASA - Ames Research Center
Moffett Field, CA 94035

Professor W.W. Willmarth
Department of Aerospace Engineering
University of Michigan
Ann Arbor, MI 48109